LIPID-DEPENDENT MODULATION OF DESENSITIZATION IN PENTAMERIC LIGAND-GATED ION CHANNELS

TOKA HUSSEIN

Thesis submitted to the University of Ottawa
in partial Fulfillment of the requirements for the
Doctorate in Philosophy in Biochemistry

Department of Biochemistry, Microbiology, and Immunology
Faculty of Medicine
University of Ottawa

Abstract

Pentameric ligand-gated ion channels (pLGICs) are central to fast synaptic communication in the nervous system. Upon agonist binding, these receptors open an ion-conducting pore across the postsynaptic membrane, allowing selective ions to flow down their electrochemical gradient into the cell, and prolonged exposure to agonist drives the channels into a non-conducting desensitized state. While agonist binding initiates channel opening, the agonist-induced response can be influenced by various exogenous and endogenous compounds, including the lipids in the cell membrane. Although the lipid sensitivity of the prototypic pLGIC, the nicotinic acetylcholine receptor (nAChR) from *Torpedo*, is well characterized, the lipid sensitivities of other pLGICs, including the prokaryotic ELIC, have only recently gained considerable interest. Structural studies have identified a putative inner-leaflet lipid pocket in ELIC, shaped by a Trp-Arg-Pro (W-R-P) motif. Compelling evidence suggests that binding of phosphatidylethanolamine (PE) or phosphatidylglycerol (PG) to this site leads to slower rates of ELIC desensitization, likely by influencing the dynamics or position of the outermost transmembrane helix, M4. This motif is conserved in anion-selective pLGICs and in GLIC, raising the question of whether it plays a conserved functional role.

Using site-directed mutagenesis and two-electrode voltage clamp (TEVC) electrophysiology, I probed the role of the W-R-P motif in ELIC and tested whether this lipid site plays a conserved functional role across pLGICs. I show that the W-R-P pocket plays different roles in modulating desensitization across pLGICs. Mutations to W-R-P pocket residues and to regions of M4 affect desensitization rates in both ELIC and the α1 glycine receptor (GlyR) but have no measurable effect in GLIC. ELIC also tolerates a broader range of M4 mutations than GlyR or GLIC. The phenotypes observed correlates with the density of

aromatic interactions at the M4-M1/M3 interface, which is sparse in ELIC but extensive in α1 GlyR and GLIC.

Focusing on ELIC, I then show that the strength of interactions at the M4-M1/M3 interface modulates the rate of desensitization. Eliminating the Trp224-Arg301 cation-π interaction accelerates desensitization, while reversing or substituting this interaction with a potential salt bridge restores slow desensitization. Strengthening M4-M1/M3 interactions through three aromatic substitutions partially restores slow-desensitizing phenotypes. My data identify three distinct interactions and/or features of the M4-M1/M3 interface that contribute to slow desensitization in ELIC including the Trp224-Arg301 cation-π interaction, an interaction between W220 on M1 and S271 on M3, and the Pro305 kink on M4.

Collectively, my data shows that the W-R-P pocket plays different roles in shaping desensitization across pLGICs, and that the strength of interactions at the M4-M1/M3 interface modulate the rate of ELIC desensitization. These findings support a model in which lipid binding at the W-R-P pocket modulates ELIC desensitization through its effects on M4 structure or dynamics, while the broader architecture of the M4-M1/M3 interface determines whether this mechanism applies in other pLGICs.

Acknowledgements

I would like to thank my supervisor, Dr. Baenziger, for his guidance and support through every up and down of this journey. Your mentorship helped me a lot, in the lab and outside of it. From you, I learned how to navigate life with a clearer head, and how to "rise above feelings":)

I would like to thank my TAC committee members, Dr. Corrie daCosta, Dr. Jean-François Couture, and Dr. Natalie Goto, for their guidance and constructive comments that helped bring this work to completion.

A special immense gratitude goes to Dr. Camille Hénault. You were patient with me as I learned to pull my first glass pipette and record my first 'real' TEVC trace. This work wouldn't have been where it is today without your consistent feedback, long debates of what the data meant and where to take it next. Shoutout to our walks and unleashing our artistic sides in the Mud Oven!

I would like to thank all current and past members of the Baenziger lab Anna, Camille (I know, again), Christian, Deepansh, Fareed, Mack, Rui Yan, and Serena. From the daCosta lab Mariam and Louise. Thank you all for the insightful discussions during the Ion Channel Journal Club or just enjoying food at Father's and Sons.

To the colleagues I met as fresh graduate students and now lifelong friends Redaet Daniel, Sara El-Sahli, Aisha Saleh, Rashida Rajgara, Houda Tantawi, Nourelhouda Bouhlel, and Nasteho Abdoulkader, thank you from the bottom of my heart.

To all my Ottawa friends, you all made my experience here very enjoyable and memorable. My journey would've never been the same without our celebrations of small wins, birthdays, spontaneous karaoke and paint nights. Navigating the challenges of being an international graduate student wouldn't have been possible without all of you.

They say long-distance friendships are hard to keep, but I think when all 'true' friends scatter across the world chasing better lives, staying close is one of the most generous things you can do for each other. Eman ElGazzar, Zainab Hassan, Hoda Akl, Noha Harag, Mayar Shahin, and Sara Khalid, thank you for being my true friends. To Omar Eldaghar and Hebatallah Mohamed, my dearest friends now in heaven, you may have left this world, but the values you both instilled in me and all our friends, hard work, helping others, and enjoying life to the max, live on in all of us.

To my parents, Osama and Magda, thank you for all the love and everything that you have done raising me the way I am. I would not be standing where I am without you, and I hope I keep making you proud.

To my brothers Mohamed and Ahmed, thank you for the long calls and unwavering support. I am so proud of the people you are becoming.

To Hassan, what a nice turn of life events eh? :) thank you and your family for all the steady love and continuous support.

Table of Contents

List of Figures

List of Tables

List of Abbreviation

%Des	extent of desensitization at the end of agonist application
τ	time constant of current decay
ACh	acetylcholine
AChBP	acetylcholine binding protein
AMPA	α-amino-3-hydroxy-5-methyl-4-isoxazolepropionic acid
ANOVA	analysis of variance
ATP	adenosine triphosphate
BTX	bungarotoxin
cDNA	complementary deoxyribonucleic acid
CHS	cholesteryl hemisuccinate
CNS	central nervous system
cRNA	complementary ribonucleic acid
cryo-EM	cryogenic electron microscopy
DHA	docosahexaenoic acid
DNA	deoxyribonucleic acid
DTT	dithiothreitol
EC_{50}	agonist concentration eliciting half-maximal response
ECD	extracellular domain
ELIC	*Erwinia chrysanthemi* ligand-gated ion channel
EPR	electron paramagnetic resonance
EPSP	excitatory postsynaptic potential
GABA	γ-aminobutyric acid
$GABA_AR$	γ-aminobutyric acid type A receptor

GLIC	*Gloeobacter* ligand-gated ion channel
GlyR	glycine receptor
GPCR	G protein-coupled receptor
HEK	human embryonic kidney
HEPES	4-(2-hydroxyethyl)-1-piperazineethanesulfonic acid
ICD	intracellular domain
IPSP	inhibitory postsynaptic potential
LGIC	ligand-gated ion channel
MES	2-(N-morpholino)ethanesulfonic acid
MS	mass spectrometry
nAChR	nicotinic acetylcholine receptor
NMDA	N-methyl-D-aspartate
NTD	N-terminal domain
PAM	positive allosteric modulator
PC	phosphatidylcholine
PCR	polymerase chain reaction
PDB	Protein Data Bank
PE	phosphatidylethanolamine
PG	phosphatidylglycerol
pH_{50}	pH eliciting half-maximal response
PI	phosphatidylinositol
pLGIC	pentameric ligand-gated ion channel
PNS	peripheral nervous system
POPC	1-palmitoyl-2-oleoyl-sn-glycero-3-phosphocholine
POPE	1-palmitoyl-2-oleoyl-sn-glycero-3-phosphoethanolamine

POPG	1-palmitoyl-2-oleoyl-sn-glycero-3-phosphoglycerol
PS	phosphatidylserine
SMA	styrene maleic acid
sTeLIC	*Symbiobacterium thermophilum* ligand-gated ion channel
TEVC	two-electrode voltage clamp
THC	Δ9-tetrahydrocannabinol
THDOC	tetrahydrodeoxycorticosterone
TMD	transmembrane domain

1 Chapter 1 – Introduction

In the 17th century, René Descartes wrote what is now considered as the first principle of modern philosophy: *"dubito, ergo sum, vel, quod idem est, cogito, ergo sum"-"I doubt, therefore I am, or what is the same, I think, therefore I am."*. With this, he placed conscious thought at the center of human existence. This set the stage for a lasting, complex question: what does it mean to think and to be, and how does the mind relate to the physical body, or to consciousness itself.

Today, this question is approached through biology. Modern neuroscience places the nervous system, and especially the brain, at the center of efforts to understand consciousness. Conscious experience depends on nervous system activity, emerging from the coordinated interaction of many interconnected neural circuits rather than from a single structure. The complexity and organization of the nervous system therefore provide the physical basis for perception, cognition, and identity. In this way, a philosophical question of being leads to a biological investigation, as understanding nervous system function is not only a biological problem but also a step towards understanding the self.

The ability to sense the environment, interpret information, and respond is what gives rise to perception, behavior, and, ultimately, consciousness. At the most basic level, this ability allows us to see, hear, smell, taste, and feel. These functions are supported by the nervous system through tightly regulated signaling that enables rapid and accurate communication but also leaves the system vulnerable. Even small changes at the cellular or molecular scale can disrupt signaling and, over time, lead to neurological dysfunction or disease. Such perturbations may arise from genetic mutations or from the action of endogenous or exogenous compounds. Consequently, many neuronal signaling components have emerged as effective sites for therapeutic intervention. For this reason, understanding the nervous system requires moving

beyond organism-level descriptions to investigate the cellular and molecular mechanisms that underlie neural communication. Although research has advanced our knowledge of brain structure, synaptic transmission, and neurological disorders, many of the fundamental processes that govern neuronal function remain poorly understood.

This thesis focuses on a key class of membrane proteins involved in neuronal signaling, the superfamily of pentameric ligand-gated ion channels (pLGICs). These neurotransmitter-gated receptors are located at neuronal and neuromuscular synapses where they play a central role in fast synaptic transmission. While neurotransmitter, or agonist, binding activates pLGIC function, the lipid environment in the cell membranes surrounding these channels modulate their activity, although the detailed mechanisms are still emerging.

The goal of my research has been to gain a deeper understanding of how membrane lipids influence pLGIC activity. Specifically, I focus on the W-R-P motif, a conserved amino acid triad that shapes a lipid-binding site at the inner-leaflet of pLGICs, to test whether this motif plays a conserved role in desensitization across the pLGIC family. I also examine how interactions in the transmembrane domain (TMD) of *Erwinia chrysanthemi* ligand-gated ion channel (ELIC), a prokaryotic pLGIC, shape channel desensitization. The central questions addressed in this work are: first, whether the conserved W-R-P motif supports a conserved mechanism across pLGIC family members, and second, how interactions at the W-R-P pocket and the M4-M1/M3 interface in ELIC influence channel desensitization through their effects on M4 structure or dynamics. To address these questions, I studied both prokaryotic and eukaryotic pLGICs.

Because a deep understanding of neuronal communication is essential to this work, I begin with a review of the nervous system and signal transduction, followed by an in-depth discussion of pLGICs structure, function, and their sensitivity to lipids.

1.1 The nervous system coordinates complex organismal function

The brain is the most complex organ of the human body. It is composed of billions of interconnected nerve cells, or neurons, but constitutes only one component of the nervous system. The nervous system is divided into the central nervous system (CNS) and the peripheral nervous system (PNS), which together support information processing and communication across the body.

The CNS, which consists of the brain and spinal cord, serves as the primary site of information integration. It receives sensory input, processes this information, and generates coordinated output signals. These signals are transmitted to peripheral tissues through the PNS. The PNS is composed of nerves, which are cable-like bundles of axons from many neurons wrapped in connective tissue that extend from the CNS to muscles, organs, and sensory receptors. Through these connections, the PNS conveys sensory information to the CNS and distributes motor commands to target tissues.

1.1.1 Neurons and glial cells coordinate long-range signaling across the body

Communication across the nervous system relies on two main cell types: neurons and glial cells. Neurons are specialized cells that transmit information over long distances using electrical and chemical signals. They convert external stimuli, such as chemical or mechanical cues, into nerve impulses, which either carry this sensory information to the brain or send motor commands to muscles and glands, as discussed in more detail below. Notably, mature neurons have a very limited capacity for self-repair and do not undergo cell division. Thus, neuronal loss due to injury or disease is often irreversible and contributes to chronic neurodegenerative disorders such as Alzheimer's disease (Brophy & Shen, 2009).

Glial cells, on the other hand, do not transmit signals themselves, but support neurons by maintaining the structural, metabolic, and physiological conditions required for efficient neural communication. Glial cells, also known as neuroglia, support neuronal function by regulating the extracellular environment, providing metabolic support, and insulating axons. In the CNS, oligodendrocytes form myelin sheaths around each axon, while Schwann cells perform this role in the PNS, increasing the speed of signal transduction. Other glial cells, such as astrocytes, help regulate extracellular ion levels, clear neurotransmitters from the synaptic cleft, and support synaptic function. Unlike neurons, glial cells retain the capacity to divide in the adult nervous system. Following injury, such as stroke or trauma, neurons are not replaced, thus, glial cells often proliferate at or near the site of damage, a response known as gliosis. This proliferative capacity allows glia to participate in tissue repair and maintenance of the neural environment after injury (Brophy & Shen, 2009).

Figure 1-1 Neuronal structure and action potential propagation.

a. Schematic of a myelinated neuron showing dendrites, the soma, the axon, nodes of Ranvier, and axon terminals. **b.** Insets illustrate the stages of an action potential, including the resting state, depolarization, repolarization, and the refractory period, along with the associated movement of Na^+ and K^+ through voltage gated ion channels across the membrane. The membrane potential trace summarizes the time course of these events during an action potential. The figure was created using BioRender.

a.

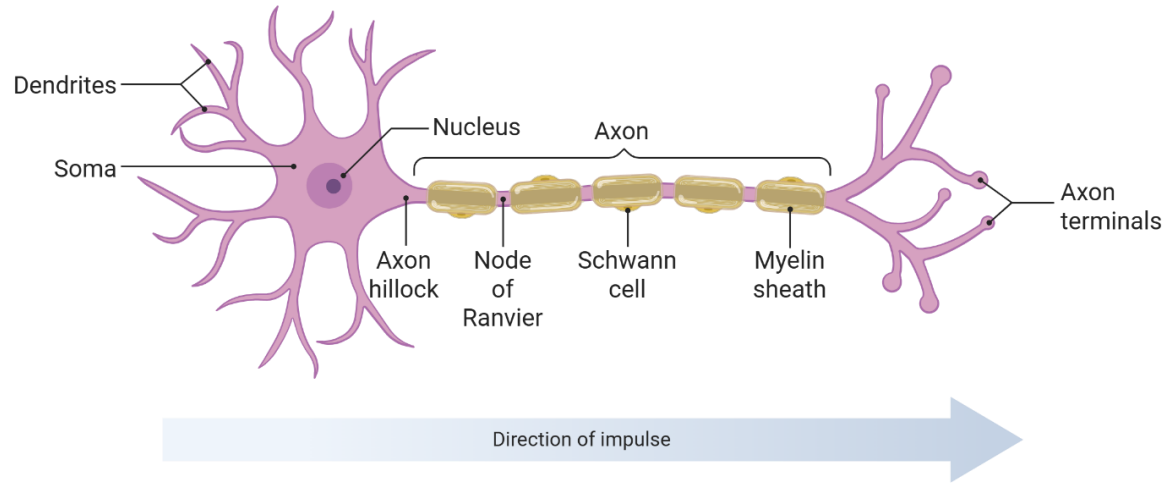
Dendrites
Soma
Nucleus
Axon
Axon terminals
Axon hillock
Node of Ranvier
Schwann cell
Myelin sheath
Direction of impulse

b.

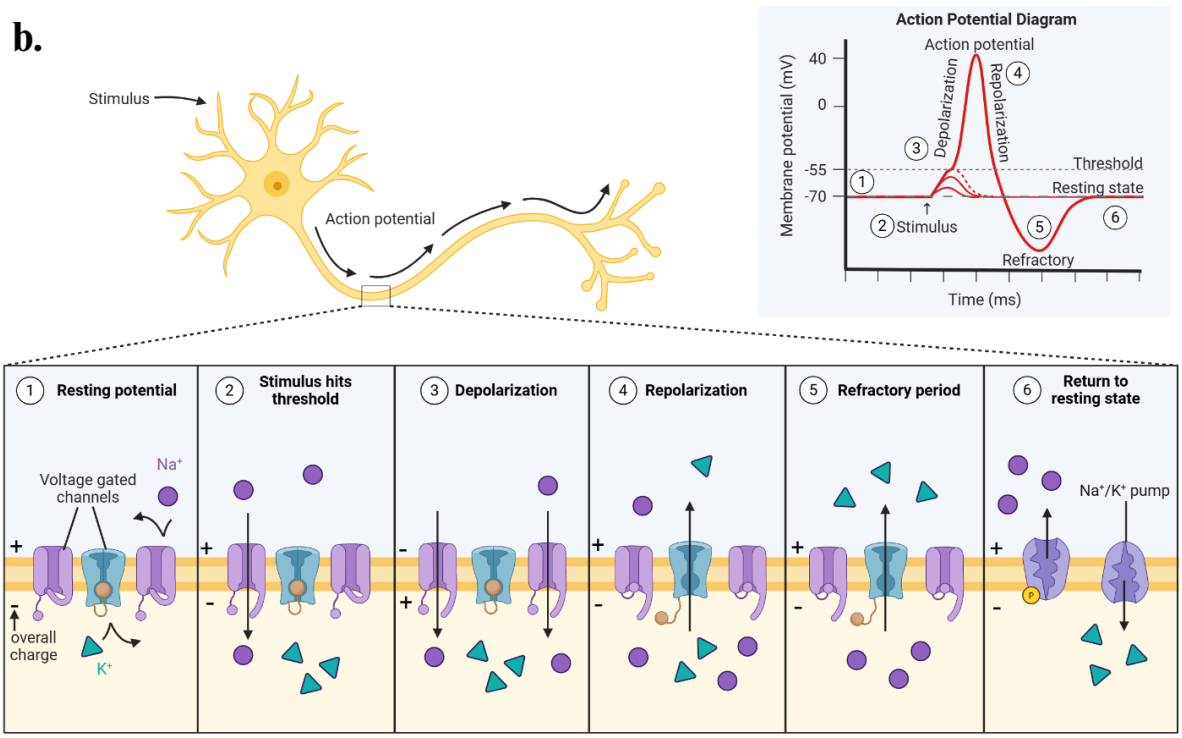
Stimulus
Action potential
Action Potential Diagram
Action potential
Depolarization
Repolarization
Threshold
Resting state
Stimulus
Refractory
Membrane potential (mV)
Time (ms)
1 Resting potential
2 Stimulus hits threshold
3 Depolarization
4 Repolarization
5 Refractory period
6 Return to resting state
Voltage gated channels
Na+
K+
overall charge
Na+/K+ pump

1.1.2 Neuronal communication: From Electrical to Chemical Signaling

The primary function of a neuron is to transmit signals from one end of the cell to the other. To accomplish this unidirectional flow of information, each neuron consists of three main structures: dendrites, the cell body or soma, and the axon. Signals from other cells or external stimuli are first detected by highly branching dendrites and transmitted to the soma. These signals are then transmitted along the axon, as an electrical impulse, to the axon terminus. The axon is a thin, elongated fiber that varies in length and can extend up to 1.5 meters in adults. In many neurons, the axon is partially wrapped in a lipid-rich layer called the myelin sheath, which insulates the fiber and increases the speed of action potential propagation. The myelin sheath does not cover the axon continuously. Instead, short unmyelinated gaps, known as nodes of Ranvier, are found at regular intervals along the axon. This architecture enables a faster mode of signal transmission, as described below.

Our current understanding of neuronal signalling is shaped by the foundational work of Hodgkin and Huxley in the 1950s. Using the squid giant axon, they demonstrated that action potential in neurons arises from the tightly regulated flow of sodium (Na^+) and potassium (K^+) ions across the plasma membrane. This discovery established the ionic basis of the nerve impulse and introduced voltage-gated ion channels as key regulators of membrane potential (Catterall, 1996; Catterall et al., 2012; Hodgkin, 1948; HODGKIN & HUXLEY, 1952; HODGKIN & KATZ, 1949; Schwiening, 2012).

Neurons maintain a resting membrane potential of about -70 mV through the coordinated activity of two key membrane proteins: the Na^+/K^+ pump and K^+ leak channels. The Na^+/K^+ pump uses ATP to actively transport three Na^+ ions out of the cell and two K^+ ions into the cell, establishing a concentration gradient where K^+ accumulates inside the cell while Na^+ accumulates outside. At the same time, K^+ leak channels allow K^+ to diffuse passively out

of the cell down its concentration gradient. As K^+ leaves the cell, the intracellular environment becomes increasingly negative, in part because large, negatively charged intracellular proteins and organic anions remain trapped inside the cell. A stable resting potential of -70 mV is reached when the outward chemical driving force promoting K^+ efflux is exactly balanced by the inward electrical force opposing it, a relationship described by the Nernst equation for K^+ (Hille et al., 1999).

Neuronal signaling begins when external stimuli cause the opening of cation channels in the dendrites, allowing Na^+ to enter the cell. These Na^+ ions then passively diffuse through the dendrites and the soma to the axon hillock, a specialized region at the junction between the soma and the axon where action potentials are initiated. When the cumulative input depolarizes the membrane at the axon hillock to a threshold of around -55 mV, voltage-gated Na^+ channels open, allowing Na^+ to rapidly enter the cell, driving the membrane potential toward +30 mV (**Figure 1-1b, stages 1 and 3**). The inward Na^+ current depolarizes the adjacent region of the axon, causing voltage-gated Na^+ channels to open, allowing Na^+ ions to enter the cell and diffuse down through the myelinated region of the neuron to the next node of Ranvier. The resulting increase in internal Na^+ ions at this node then depolarizes the membrane to open a new set of Na^+ channels, facilitating a new burst of Na^+ ion influx/diffusion, and thus the propagation of the action potential. The action potential thus jumps from one node of Ranvier to the next, a process called saltatory conduction. Saltatory conduction increases the speed of signal transmission thus allowing the electrical signal to reach the axon terminal more rapidly than it would with the continuous, wavelike propagation that occurs in unmyelinated fibers (**Figure 1-1b, stage 3)** (Catterall et al., 2012) .

Following depolarization at each node of Ranvier, Na^+ channels rapidly inactivate, preventing further Na^+ entry, and voltage-gated K^+ channels open. The resulting K^+ efflux restores the membrane potential toward resting levels, often producing a brief undershoot

known as hyperpolarization (**Figure 1-1b, stages 4 and 5**). During this brief refractory period, the membrane cannot fire another action potential, ensuring that the signal propagates in one direction only. The Na^+/K^+ pump then restores the ion gradients by transporting three Na^+ out and two K^+ in, returning the membrane to its resting potential (**Figure 1-1b, stage 6**). This cycle forms a single action potential. The action potential is initiated at the axon hillock and travels down the axon via saltatory conduction in myelinated neurons, as described above (Catterall et al., 2012) .

When the action potential reaches the axon terminal, membrane depolarization leads to the opening of voltage-gated calcium (Ca^{2+}) channels , allowing Ca^{2+} to flow into the terminal (**Figure *1-2*, step 2**). The increase in intracellular concentration facilitates Ca^{2+} binding to synaptotagmin, a calcium-sensing protein anchored on the surface of synaptic vesicles, small unilamellar vesicles filled with chemical neurotransmitters. This binding triggers a conformational change in synaptotagmin that promotes vesicle fusion to the presynaptic membrane, releasing neurotransmitters into the synaptic cleft - the narrow extracellular space between the pre and postsynaptic membranes (**Figure *1-2*, step 3**). Neurotransmitters then diffuse across the synaptic cleft and bind to receptors on the postsynaptic membrane of a neuron or muscle fiber, allowing the signal to propagate to the next cell (**Figure *1-2*, step 4**) (Südhof, 2013).

Figure 1-2 Synaptic transmission at the neuromuscular junction.

(1) An action potential arrives at the presynaptic axon terminal. (2) Membrane depolarization opens voltage-gated Ca^{2+} channels (pink, presynaptic membrane), allowing Ca^{2+} to flow into the presynaptic terminal. Ca^{2+} binds to synaptotagmin (purple crescents), a calcium-sensing protein anchored on the surface of acetylcholine (ACh)-containing synaptic vesicles. This binding triggers a conformational change that promotes vesicle fusion with the presynaptic membrane. (3) Vesicle fusion releases ACh into the synaptic cleft at the neuromuscular junction. ACh diffuses across the cleft and binds to nicotinic acetylcholine receptors (nAChRs, teal) on the postsynaptic muscle membrane. (4) ACh binding opens the nAChR ion channel pore, allowing Na^{+} to flow into the muscle cell, causing membrane depolarization and triggering muscle contraction. The figure was created using BioRender.

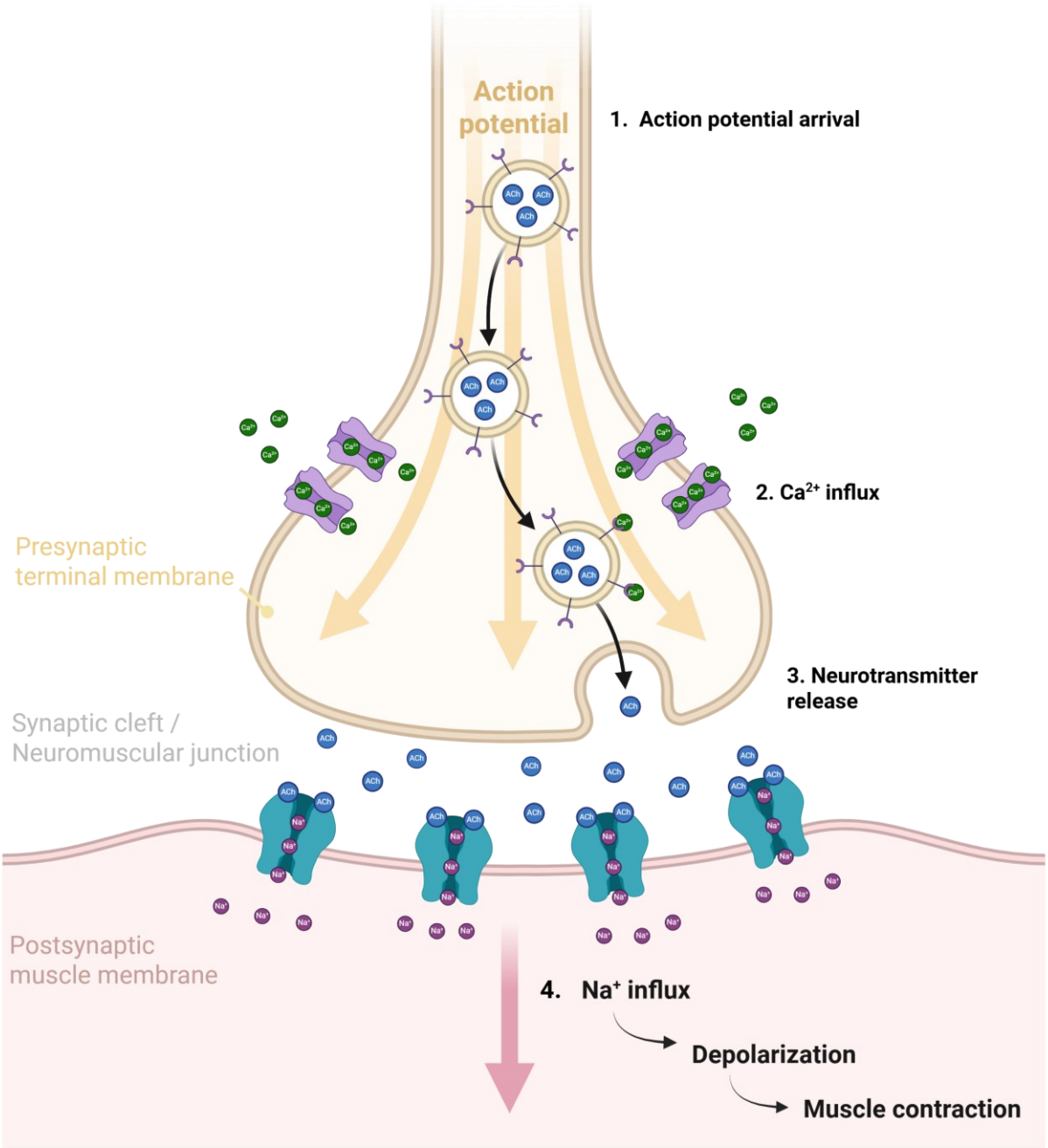
Action potential
1. Action potential arrival
2. Ca2+ influx
Presynaptic terminal membrane
3. Neurotransmitter release
Synaptic cleft / Neuromuscular junction
Postsynaptic muscle membrane
4. Na+ influx
Depolarization
Muscle contraction

1.1.3 Postsynaptic Receptor Classes and Synaptic Signalling

Postsynaptic receptors fall into two broad classes, metabotropic and ionotropic receptors. Metabotropic receptors, such as G-protein coupled receptors (GPCRs) do not directly conduct ions. Instead, they activate intracellular signaling pathways that modulate neuronal excitability over longer timescales, often by indirectly regulating ion channel activity or gene expression. As these pathways involve multiple intermediate steps, metabotropic signaling is relatively slow and produces sustained, modulatory effects.

In contrast, ionotropic receptors are ligand-gated ion channels (LGICs) that open directly in response to neurotransmitter binding, allowing specific ions to flow across the membrane within milliseconds. This rapid ion flux produces immediate changes in post-synaptic membrane potential, enabling fast and reliable communication between neurons. The effect can be either excitatory or inhibitory, depending on the ion selectivity of the channel and the direction of ion movement. Excitatory channels conduct cations and depolarize the post-synaptic membrane, promoting action potential firing and signal propagation, while inhibitory channels conduct anions and hyperpolarize the membrane, suppressing action potential firing. The balance between excitation and inhibition is essential for normal neural circuit function, and its disruption underlies many neurological and psychiatric disorders.

Because of their speed and direct gating mechanism, ionotropic receptors are critical for precise timing, rapid signal integration, and the overall fidelity of synaptic transmission, with even small changes in ion channel gating having profound effects on neural communication. Disruption of neurotransmitter receptor function, which alters the timing, strength, and/or balance of excitation and inhibition, is implicated in many neurological and neuromuscular diseases. For example, mutations in anion-conducting receptors that reduce inhibitory conductance can shift the balance toward excitation, predisposing to seizures or

disorders such as startle disease (or hyperekplexia) (Becker et al., 2002; Bode & Lynch, 2014; Breitinger et al., 2004; Chung et al., 2010; Davies et al., 2010; Moraga-Cid et al., 2015; Moroni et al., 2011). Conversely, overly persistent inhibitory currents can excessively dampen neuronal activity, contributing to conditions such as ataxia or paralysis (Benarroch, 2021; Rajakulendran et al., 2007). Similarly, dysfunction of nicotinic acetylcholine receptors (nAChRs) at the neuromuscular junction impairs reliable neuromuscular transmission, resulting in muscle weakness and/or seizures. This can occur through autoantibody-mediated receptor loss in myasthenia gravis or through gain- or loss-of-function mutations that prolong or shorten channel opening in congenital myasthenic syndromes (Lindstrom et al., 1976; Ohno et al., 1995; Sine et al., 1995). Together, these examples illustrate that maintaining a proper balance of excitatory and inhibitory channel activity, both in magnitude and timing, is essential for normal nervous system function.

1.2 Ligand-gated ion channels mediate fast synaptic signaling

LGICs are membrane proteins that open an ion channel across the membrane in response to neurotransmitter binding, a process known as gating. Upon activation, these channels allow selective ions to flow across the membrane, producing either an excitatory or inhibitory effect. Channels that conduct cations, like Na^+ or Ca^{2+}, depolarize the postsynaptic cell, generating excitatory postsynaptic potentials (EPSPs). In contrast, channels that conduct anions such as Cl^- hyperpolarize or stabilize the membrane potential, producing inhibitory postsynaptic potentials (IPSPs). The strength and duration of these responses depend on ion selectivity, the number of receptors activated, and the kinetics of channel gating.

In addition to activation, LGIC function is dynamically regulated during sustained neurotransmitter exposure. Upon prolonged agonist-binding, LGICs adopt a desensitized state. In this state, the channel pore closes, despite the bound neurotransmitter. Desensitization helps

limit response duration and prevents overstimulation during sustained neurotransmitter release. The rate and extent of desensitization vary among receptors and play an important role in shaping how neurons integrate input, generate action potentials, and maintain temporal precision within neural circuits. Through these functions, ion channels play a key role in regulating synaptic strength, plasticity, and overall neural networks behaviour (M. V Jones & Westbrook, 1995; Voglis & Tavernarakis, 2006)

1.2.1 Structural classes of ligand-gated ion channels

LGICs are grouped into three main classes based on their structural architecture, with each class linked to distinct physiological roles. Trimeric receptors include ATP-gated P2X ion channels, which play key roles in synaptic transmission, pain sensation, and inflammatory responses (M. T. Young, 2010). Tetrameric receptors include glutamate-activated cation channels. Of these, tetrameric AMPA (α-amino-3-hydroxy-5-methyl-4-isoxazolepropionic acid) receptors mediate most fast excitatory neurotransmission in the CNS and are critical for learning and memory processes (Swanson, 2009). NMDA (N-methyl-D-aspartate) receptors, which are slower-gating glutamate channels, play a key role in synaptic plasticity and memory formation. Kainate receptors primarily serve modulatory functions, fine-tuning neuronal excitation and inhibition through both pre- and postsynaptic mechanisms (Pinheiro & Mulle, 2006). Finally, pentameric ligand-gated ion channels (pLGICs) form a distinct structural class that contributes to motor control, sensory processing, and neural plasticity (Albuquerque et al., 2009; Lynch, 2004). The focus of this thesis is on the function of pLGICs, which are discussed in detail below.

1.3 Pentameric ligand-gated ion channels are structurally conserved mediators of neurotransmission

In humans, pLGICs are expressed throughout both the CNS and the PNS and are divided into four major families based on neurotransmitter specificity and ion selectivity. Two families are cation-selective and thus excitatory, responding to acetylcholine through nicotinic acetylcholine receptors (nAChRs) and to serotonin (5-HT) through serotonin type 3 receptors (5-HT_3Rs). The other two families are anion-selective and thus inhibitory, activated by γ-aminobutyric acid (GABA) via $GABA_A$ receptors ($GABA_A$Rs) and glycine (Gly) via glycine receptors (GlyRs) (Ananchenko et al., 2022; Thompson & Baenziger, 2020).

Each of these families consists of both homo- and hetero-pentameric receptors assembled from distinct subunit combinations. The nAChR family includes sixteen subunits (α1-α7, α9-α10, β1-β4, δ, γ, and ε) (Albuquerque et al., 2009), while the 5-HT_3 receptor family includes five subunits (A, B, C, D, and E) (Lummis, 2012). $GABA_A$ receptors include nineteen subunits (α1- α6, β1-β3, γ1-γ3, ε, δ, π, θ, and ρ1-ρ3) (Olsen & Sieghart, 2008), and GlyR include five subunits (α1-α4 and β) (Lynch, 2004). This subunit diversity enables fine tuning of receptor kinetics, pharmacology, and modulation, allowing pLGIC signaling to be precisely adapted to the functional requirements of specific neuronal circuits.

Different combinations of subunits give rise to receptors with distinct functional properties and expression patterns across tissues. In the PNS, muscle-type nAChRs mediate synaptic transmission at the neuromuscular junction, where their rapid activation triggers muscle contraction. In the CNS, neuronal nAChRs mediate fast excitatory neurotransmission and are implicated in processes such as arousal, attention, and reward (Curtis & Ryall, 1964; Dale, 1936; Kuffler & Yoshikami, 1975b). 5-HT_3Rs mediate fast excitatory neurotransmission

in both the CNS and PNS and play key roles in autonomic reflexes and the brain-gut axis (Bradley, 1987; Kilpatrick et al., 1987; Richardson & Engel, 1986; Tecott et al., 1993).

By contrast, inhibitory $GABA_A$Rs and GlyRs are essential for maintaining excitation-inhibition balance, $GABA_A$Rs predominate in the brain, while GlyRs are most abundant in the spinal cord and brainstem, where they mediate fast synaptic inhibition (Arregui et al., 1972; Bowery & Smart, 2006; Dudel & Kuffler, 1961c, 1961b, 1961a; Edwards & Kuffler, 1959; Kuffler & Edwards, 1958; Kuffler & Eyzaguirre, 1955; Kuffler & Yoshikami, 1975b, 1975a; A. B. Young & Snyder, 1973, 1974; Zukin et al., 1974)

In addition to these eukaryotic families, homologous pLGICs are also found in bacteria, demonstrating that the core architecture underlying fast ligand-gated ion conduction predates the evolution of the nervous system. Several prokaryotic pLGICs have been identified, including the *Erwinia chrysanthemi* ligand-gated ion channel (ELIC), the *Gloeobacter violaceus* ion channel (GLIC), the *Desulfofustis glycolicus* ligand-gated ion channel (DeCLIC), and the *Tevnia jerichonana* symbiont ligand-gated ion channel (sTeLIC). ELIC and GLIC have been widely used as model systems for studying pLGIC structure and function, as discussed in detail below, and DeCLIC and sTeLIC are emerging as additional models (Hu, Ataka, et al., 2018; Hu et al., 2020; Hu, Nemecz, et al., 2018; Lycksell et al., 2021; Nemecz et al., 2016; Tasneem et al., 2005).

1.4 pLGICs share a conserved architecture

The electric organs of the electric eel and the *Torpedo* ray are enriched in cholinergic synapses, making them a rich natural source of nAChRs. This access to large quantities of receptor enabled extensive biochemical and biophysical studies. The discovery that α-bungarotoxin (α-BTX), a snake venom peptide, binds nAChRs with high affinity and

specificity, enabled affinity-based purification of the receptor (Changeux et al., 1970; Michaelson & Raftery, 1974a; Schmidt & Raftery, 1973).

Subsequent biochemical, pharmacological, and affinity-labeling studies systematically mapped agonist and antagonist binding sites and identified key functional residues involved in ligand binding (Damle & Karlin, 1978; Karlin & Cowburn, 1973; Whiting & Lindstrom, 1988). Affinity labelling established that agonist binding sites are located at subunit interfaces and are coordinated by conserved aromatic residues contributed by loops from both the principal subunit (loops A-C) and the complementary subunit (loops D-G). The π-electron systems of these aromatic residues interact with positively charged or partially charged groups on the ligand, such as the quaternary ammonium of acetylcholine (Dennis et al., 1988; Galzi et al., 1990; Middleton & Cohen, 1991).

These biochemical advances set the stage for protein sequencing and, ultimately, the cloning of nAChR subunits (Claudio et al., 1983; Devillers Thiery et al., 1983; Nef et al., 1984). The striking sequence homology between subunits, and the subsequent identification of homologous genes encoding 5-HT_3R, $GABA_A$Rs and GlyRs, established the existence of a broader superfamily of pLGICs (Grenningloh et al., 1988; Schofield et al., 1988). Despite differences in ion selectivity and pharmacology, the sequence homology suggested a conserved architecture.

Pioneering cryo-electron microscopy (cryo-EM) studies by Nigel Unwin and colleagues provided the first structural insight into the architecture of the nAChR. Unwin showed that native membranes isolated from electroplaque tissue form 2D helical crystalline tubes densely packed with nAChRs, which were amenable to structural analysis by electron microscopy (Brisson & Unwin, 1985; Toyoshima & Unwin, 1988b, 1988a, 1990; Unwin et al., 1988). Initial negative-stain reconstructions provided the first low-resolution (~17 Å) images of the

receptor (Toyoshima & Unwin, 1988a). Their work revealed that nAChR is a pentamer with subunits arranged pseudo-symmetrically around a central ion conducting pore that spans the membrane, providing the first structural evidence linking receptor architecture to ion channel function. Continued methodological improvements throughout the 1990s improved resolution to ~9 Å (Unwin, 1993) and revealed rod-like densities corresponding to α-helices within each subunit, including the identification of the pore-lining M2 helix. This was followed by a ~4 Å resolution model of the extracellular and transmembrane domains (Miyazawa et al., 2003; Unwin, 1993), at which point it became possible to trace the polypeptide chain and identify the major structural domains: the extracellular domain (ECD), the transmembrane domain (TMD), and the intracellular domain (ICD). The moderate resolution of these cryo-EM models, however, was insufficient to provide an atomic view of how agonists are recognized at the binding site. This gap was filled by high-resolution X-ray crystal structures of the acetylcholine binding protein (AChBP).

AChBP is a water-soluble protein secreted by glial cells of molluscs, such as *Lymnaea stagnalis,* that shares significant sequence and structural homology with the nAChR ECD (Smit et al., 2001). High-resolution x-ray structures of AChBP revealed that the ECD consists of ten β-strands (β1-β10) arranged into two antiparallel β-sheets that fold into a β-sandwich (Brejc et al., 2001; Celie et al., 2004; Hansen et al., 2005). Structures of AChBP in complex with agonists and antagonists confirmed and extended the earlier affinity-labeling data, providing an atomic view of how loops A-C and D-G converge at the subunit interface to coordinate ligand binding (Celie et al., 2004; Hansen et al., 2005).

Integration of AChBP structures with cryo-EM and biochemical data led to the publication of a 4 Å model of the *Torpedo* nAChR pentamer in 2005 (Unwin, 2005). This was the first near-complete structural model of a full-length pLGIC, and it further established that each subunit is organized into three domains: the ECD consisting of ten β-strands (β1- β10);

Figure 1-3 Structure of the *Torpedo* nAChR

A side view of the receptor is shown on the left, with the extracellular domain (ECD) in red, the transmembrane domain (TMD) in blue, and the intracellular domain (ICD) in green (PDB: 7QL5). Residues contributing to the agonist binding sites (αTrp149) and the channel gate (Leu9' and Val13') are shown as cyan and tan spheres, respectively. Top-down views of the ECD and TMD are shown on the right. The ECD view highlights the agonist binding sites located at the interfaces between principal (αγ, αδ) and complementary (γ, δ) subunits. Figure is adapted from Ananchenko et. al 2022.

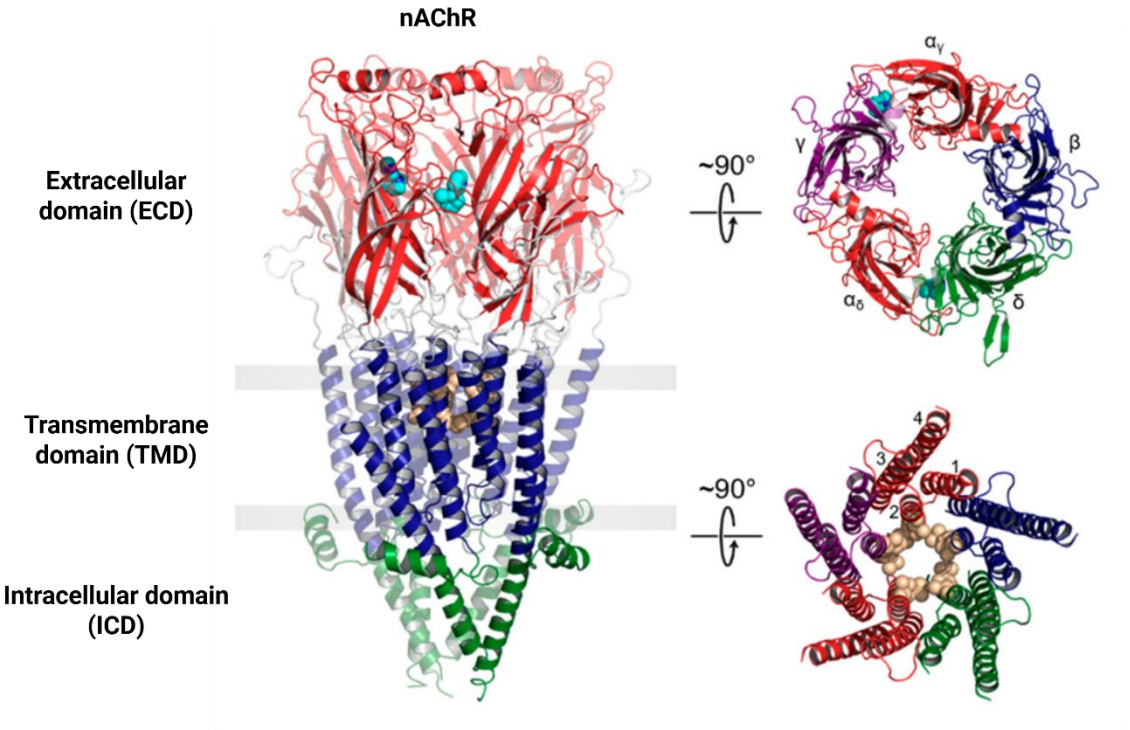
nAChR
Extracellular domain (ECD)
Transmembrane domain (TMD)
Intracellular domain (ICD)
~90°
~90°
αγ
γ
β
αδ
δ
1
2
3
4

the TMD formed by four α-helices (M1-M4); and an intracellular domain (ICD) located between M3 and M4 and consisting of a long-disordered stretch followed by an MA α-helix that connects to M4. Each domain serves a distinct function. Agonist binding occurs at the interfaces between subunits in the ECD. The TMD forms the ion-conducting pore, with M2 lining the channel and determining ion selectivity. The ICD is involved in trafficking and, in the case of the nAChR, in receptor clustering at the post-synaptic membrane. Although most pLGICs follow this three-domain organization, some prokaryotic members, such as DeCLIC, contain an additional extracellular N-terminal domain (NTD) (Hu et al., 2020; Lycksell et al., 2021). Although limited resolution introduced modeling ambiguities, the 2005 structure established the core architectural features of the pLGIC family.

Prokaryotic pLGICs offered key practical advantages over eukaryotic channels for structural studies in that 2) they can be expressed in heterologous systems at yields suitable for structural studies and 2) they lack the large ICD found in eukaryotic pLGICs making them easier to crystallize. These features enabled the first full-length pLGIC structures to be solved by x-ray crystallography. In 2008, the structure of ELIC was solved in a closed conformation (Hilf & Dutzler, 2008), followed shortly by structures of GLIC in an open-channel-like conformation (Bocquet, Nury, Baaden, Poupon, et al., 2009; Hilf et al., 2009), providing the first atomic-resolution views of the ECD-TMD assembly and the structural basis for understanding how agonist binding is transduced into pore opening. Crystal structures of sTeLIC subsequently revealed a widely open pore and a cavity for allosteric modulation (Hu, Nemecz, et al., 2018), and X-ray and cryo-EM studies of DeCLIC characterized the dynamics and Ca^{2+}-dependent regulation of its multidomain architecture (Hu et al., 2020; Lycksell et al., 2021).

Subsequent crystallographic and cryo-EM studies expanded the conformational repertoire to include closed, open, and desensitized-like states, and resolved complexes with

ions and inhibitors (Brams et al., 2020; Fourati et al., 2017, 2018; Hilf et al., 2010; Nury et al., 2011; Nys et al., 2016; Pan, Chen, Willenbring, Mowrey, et al., 2012; Pan, Chen, Willenbring, Yoshida, et al., 2012; Sauguet, Howard, et al., 2013; Sauguet, Poitevin, et al., 2013; Spurny et al., 2012, 2013, 2015), lipids (Basak et al., 2017; Bergh et al., 2024; Bharambe et al., 2024; Dalal et al., 2024, 2025; N. Dietzen et al., 2021; N. M. Dietzen et al., 2022; Hénault et al., 2019; P. Kumar et al., 2020, 2021; Sridhar et al., 2021), and pharmacological modulators (Bertozzi et al., 2016; Fourati et al., 2015; Gonzalez-Gutierrez et al., 2013; Hu, Ataka, et al., 2018; Kinde et al., 2015; Louis et al., 2022; Menny et al., 2017; Prevost et al., 2012; Rovšnik et al., 2021; Sauguet et al., 2014; Sauguet, Howard, et al., 2013). These studies established prokaryotic pLGICs as model systems for studying conserved allosteric mechanisms across the pLGIC superfamily, with ELIC the focus of this thesis.

Figure 1-4. pLGICs display a conserved core architecture with diverse auxiliary features. Side views of the prokaryote DeCLIC (PDB: 6V4S, far left), the human α1β3γ2 $GABA_AR$ (PDB: 7QNE, middle left), and the *Torpedo* nAChR (PDB: 7QL5, middle right) colored according to domains (NTD, orange; ECD, red; TMD, blue; ICD, green). Bound agonists are presented as cyan spheres at the interfaces between two subunits. In the side views, the principal subunit is on the left and the complementary subunit is on the right. Residues forming the channel gate are presented as tan spheres. Figure is adapted from Ananchenko et. al 2022.

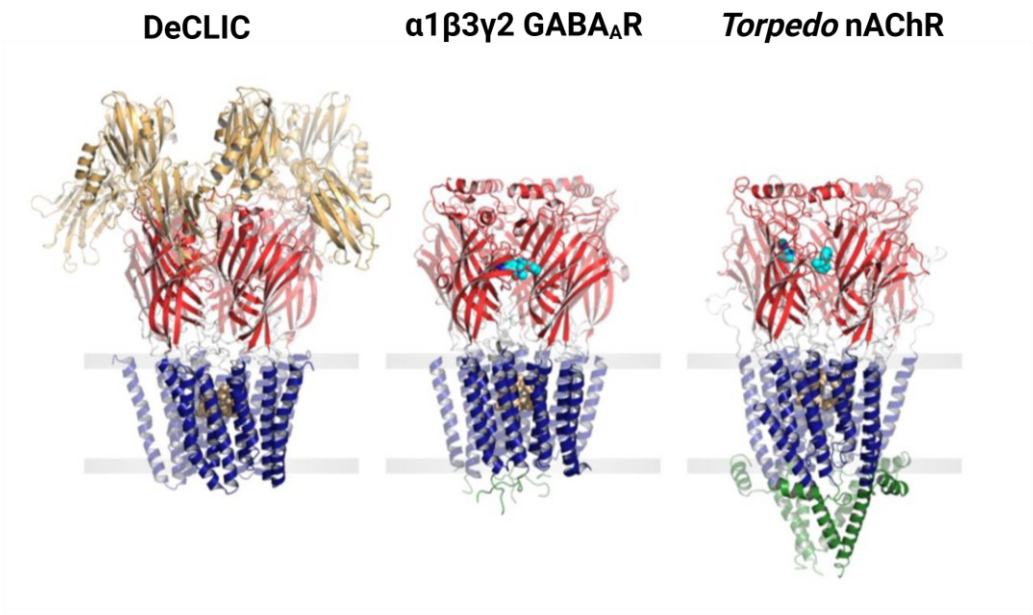
DeCLIC
α1β3γ2 GABA$_A$R
Torpedo nAChR

1.4.1 Conformational transitions underlying pLGIC function

Coupling between agonist binding in the ECD and pore opening in the TMD occurs at the interface between these two domains. Agonist binding induces compression of the binding-site loops in the ECD, driving a rocking motion of the β-sandwich. This motion is transmitted to the TMD through a network of covalent and non-covalent interactions, including the covalent linkage between β10 strand and M1 helix, as well as interactions involving the β1-β2, β6-β7, and β9-β10 loops and the M2-M3 linker. In the resting state, the ion channel pore is closed by a hydrophobic barrier formed by conserved residues in the extracellular half of the M2 helices, which excludes water molecules and thereby prevents ion permeation. Upon agonist binding, concerted rearrangements at the ECD-TMD interface propagate to the pore, resulting in coordinated tilting and twisting of the M2 helices away from the central pore axis. This structural motion widens the pore and disrupts the hydrophobic barrier, allowing hydrated ions to diffuse down their electrochemical gradient (W. Y. Lee et al., 2009; W. Y. Lee & Sine, 2005; Mukhtasimova et al., 2009; Thompson et al., 2025.).

Prolonged agonist exposure leads pLGICs to enter one or more desensitized states, which bind agonist with high affinity but are non-conductive. Desensitization rates vary widely across the pLGIC family (Auerbach & Akk, 1998; Gielen et al., 2015a; Gielen & Corringer, 2018a; Marabelli et al., 2015). This variation is functionally important. Fast desensitization shapes the duration and amplitude of post-synaptic responses, contributes to short-term synaptic plasticity, and limits drug efficacy at receptors targeted therapeutically (M. V. Jones & Westbrook, 1996; Quick & Lester, 2002). Despite this functional relevance, the structural basis of desensitization is less well understood than that of activation, and the mechanisms that modulate desensitization remain to be elucidated.

Figure 1-5 Conformational states underlying pLGICs function.

Agonist binding drives the transition of pLGICs from a resting closed state to an activated open state. With continued agonist presence, the receptor enters a desensitized non-conductive state. Shown below the schematic are the pore-lining M2 helices from two opposing subunits of the *zebrafish* α1 GlyR in putative closed (PDB 6PXD), open (PDB 6PM6), and desensitized (PDB 6PM5) conformations. Distances indicate the narrowest region of the pore in each state. In the closed conformation, the pore is constricted at the 9' leucine (L277), whereas in the desensitized conformation, constriction occurs near the -2' proline (P266). Figure is adapted from (Cheng & Arcario, 2026)

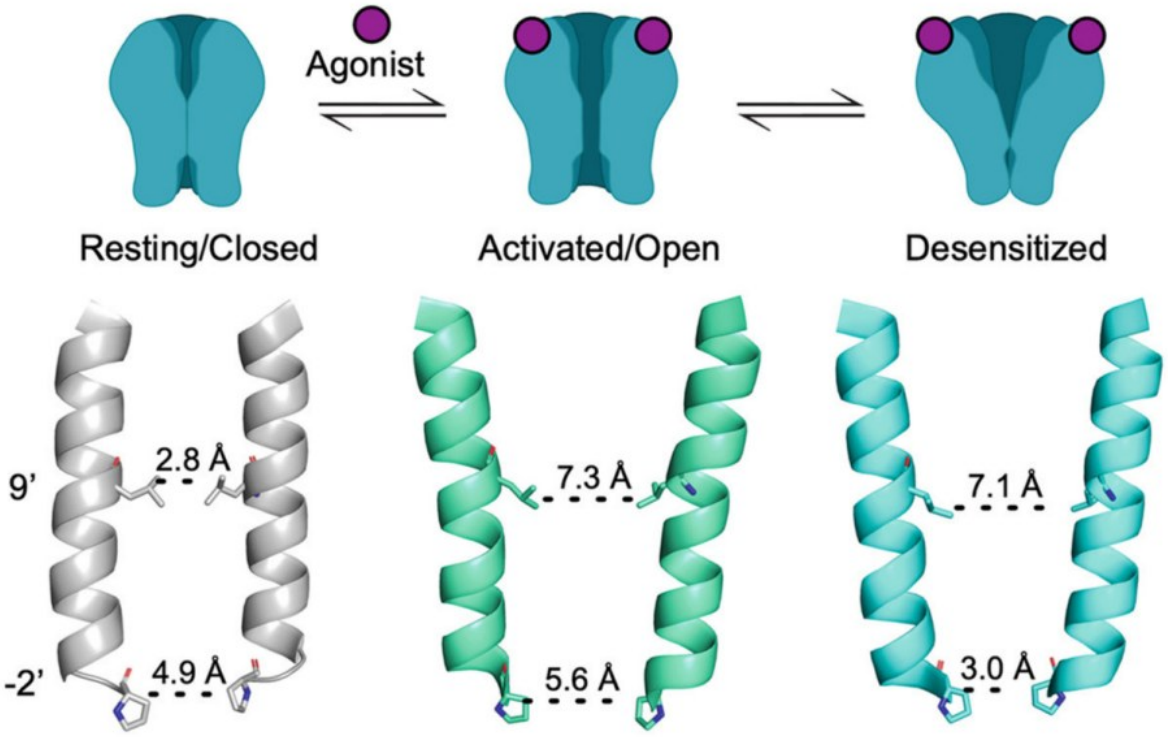
Agonist
Resting/Closed
Activated/Open
Desensitized
9'
-2'
2.8 Å
4.9 Å
7.3 Å
5.6 Å
7.1 Å
3.0 Å

In efforts of understanding desensitization, Gielen and Corringer proposed that activation and desensitization are governed by separate structural gates at different positions along the ion pore, a model they termed the dual-gate model (Gielen et al., 2015a, 2020; Gielen & Corringer, 2018a). In this model, agonist binding promotes channel opening through the activation gate in the upper half of the pore, while desensitization involved closure of a distinct gate near the intracellular end. In anion-selective pLGICs, this intracellular gate is associated with a conserved Pro residue at the -2' position of M2 (Gielen et al., 2015a). Studies using concatemeric α1β2γ2 $GABA_AR$ further showed that closure of the desensitization gate occurs through sequential, asymmetric subunit rearrangements, rather than concerted motion across all five subunits, with the γ2 subunit contributing most prominently (Gielen et al., 2020). Kinetic modeling suggested that pore closure requires desensitization of at least two subunits, with faster components reflecting partially engaged intermediate states and slower components reflecting progressive engagement of additional subunits (Gielen et al., 2020). Whether this model applies to cation-selective pLGICs remains to be tested. In the human α7 nAChR, structural and functional studies suggest that the region surrounding the activation gate (L9') also contributes to tuning desensitization kinetics (Zhuang et al., 2022), indicating that the structural determinants of desensitization are not fully conserved across the superfamily.

Although agonist binding is the primary driver of conformational change, lipids in the surrounding membrane modulate pLGICs function. Notably, interactions at a conserved lipid-binding site at the M4-M1/M3 interface have been shown to influence desensitization in ELIC (Hénault et al., 2019), suggesting that lipids are not passive components of the membrane but instead contribute directly to shaping the conformational landscape of pLGICs. The following section reviews how lipids influence pLGIC function.

1.5 The function of the pLGICs is sensitive to lipids

1.5.1 The lipid sensitivity of the *Torpedo* nAChR

The functional sensitivity of nAChRs to lipids was first recognized during early attempts to isolate and reconstitute the receptor's function in artificial liposomes. These studies showed that agonist-induced cation flux could only be maintained when the receptor was solubilized and purified in the presence of lipids and then reconstituted into membranes of defined composition that supported function (Briley & Changeux, 1977; Criado et al., 1982, 1984; Epstein & Racker, 1978; Fong & McNamee, 1986; Heidmann et al., 1980; O. T. Jones et al., 1988; O. T. Jones & Mcnamee, 1988; Michaelson et al., 1976; Michaelson & Raftery, 1974b; Sunshine & McNamee, 1992). Ion flux assays showed that robust agonist-induced activity was observed when the *Torpedo* nAChR was reconstituted into vesicles containing phosphatidylcholine (PC), anionic lipids, and cholesterol at a 3:1:1 molar ratio. In contrast, membranes lacking cholesterol, anionic lipids, or both failed to support agonist-induced responses (Criado et al., 1982, 1984; Fong & McNamee, 1986). These results initially led to the proposal that cholesterol and phosphatidic acid (PA), or other anionic lipids, bind to distinct sites on the receptor and stabilize its structure in complementary ways, with occupancy of both sites required for channel function. Subsequent work, however, pointed instead to the involvement of non-specific lipid interactions and modulation by bulk membrane physical properties (Baenziger et al., 2017; daCosta et al., 2013; daCosta & Baenziger, 2009; Thompson & Baenziger, 2020).

It was later shown that increasing levels of *either* anionic lipids or cholesterol in a PC membrane lead to an increasing proportion of agonist-responsive *Torpedo* nAChRs (Baenziger et al., 2000; Hamouda et al., 2006). Importantly, not all anionic lipids are equally effective. PA uniquely supported receptor activation in the absence of cholesterol, whereas other anionic

lipids, including phosphatidylserine (PS) and phosphatidylinositol (PI), preferentially stabilized non-activatable conformations in PC membranes lacking cholesterol (daCosta et al., 2002, 2009; daCosta & Baenziger, 2009; Hamouda et al., 2006). In parallel, cholesterol was shown to be functionally replaceable by a range of neutral lipids/cholesterol analogs, indicating that the nAChR exhibits relatively low lipid specificity with respect to either lipid class (Rankin et al., 1997; Sunshine & McNamee, 1992).

These findings were initially interpreted in the framework of a two-state equilibrium between an agonist-activatable resting state (R) and a non-activatable desensitized state (D), with the receptor in PC-only membranes assumed to be desensitized (Baenziger et al., 2000; Hamouda et al., 2006; McCarthy & Moore, 1992). This R-to-D model was later shown to be incorrect. The nAChR reconstituted in pure PC membranes adopts a conformation with resting-state-like binding affinity for ligands that bind to both the ECD and TMD, yet fails to undergo ligand-induced conformational transitions, indicating that this lipid-dependent state is neither resting nor desensitized (daCosta & Baenziger, 2009). This led to the proposal of a distinct "uncoupled" conformation (U), in which agonist binding is dissociated (or uncoupled) from channel gating. When reconstituted into membranes containing PC and PA, the receptor instead adopts a resting conformation that can transition to open (O) and desensitized states upon ligand binding (daCosta & Baenziger, 2009).

The uncoupled state model was further supported by studies of bulk membrane properties. In thick PC bilayers composed of long, unsaturated acyl chains, the receptor favours an uncoupled-like conformation that does not undergo rapid agonist-induced transitions, although transitions to high-affinity states still occur over slow timescales (daCosta et al., 2013). This indicates that bulk membrane properties, in addition to specific lipid interactions, influence the energy landscape of nAChR conformations.

Figure 1-6 Lipid modulation of the nAChR

a. The lipid-dependent uncoupled *Torpedo* nAChR. Lipid composition controls the proportion of uncoupled (U) versus resting (R) conformations (Scheme 1, boxed). Coupled conformations transition from R to O (open) and D (desensitized) states (Scheme 2) Potential role of M4 as a lipid-sensor modulating allosteric communication in the nAChR. **b.** Side view of the α subunit of the 4 Å resolution *Torpedo* structure published in 2005 (PDB ID: 2BG9) highlighting the coupling interface between the ECD and TMD. **c.** Schematic depicting possible lipid-dependent structural re-arrangements leading to loss of interactions between post-M4 and the Cys-loop (daCosta & Baenziger 2009)

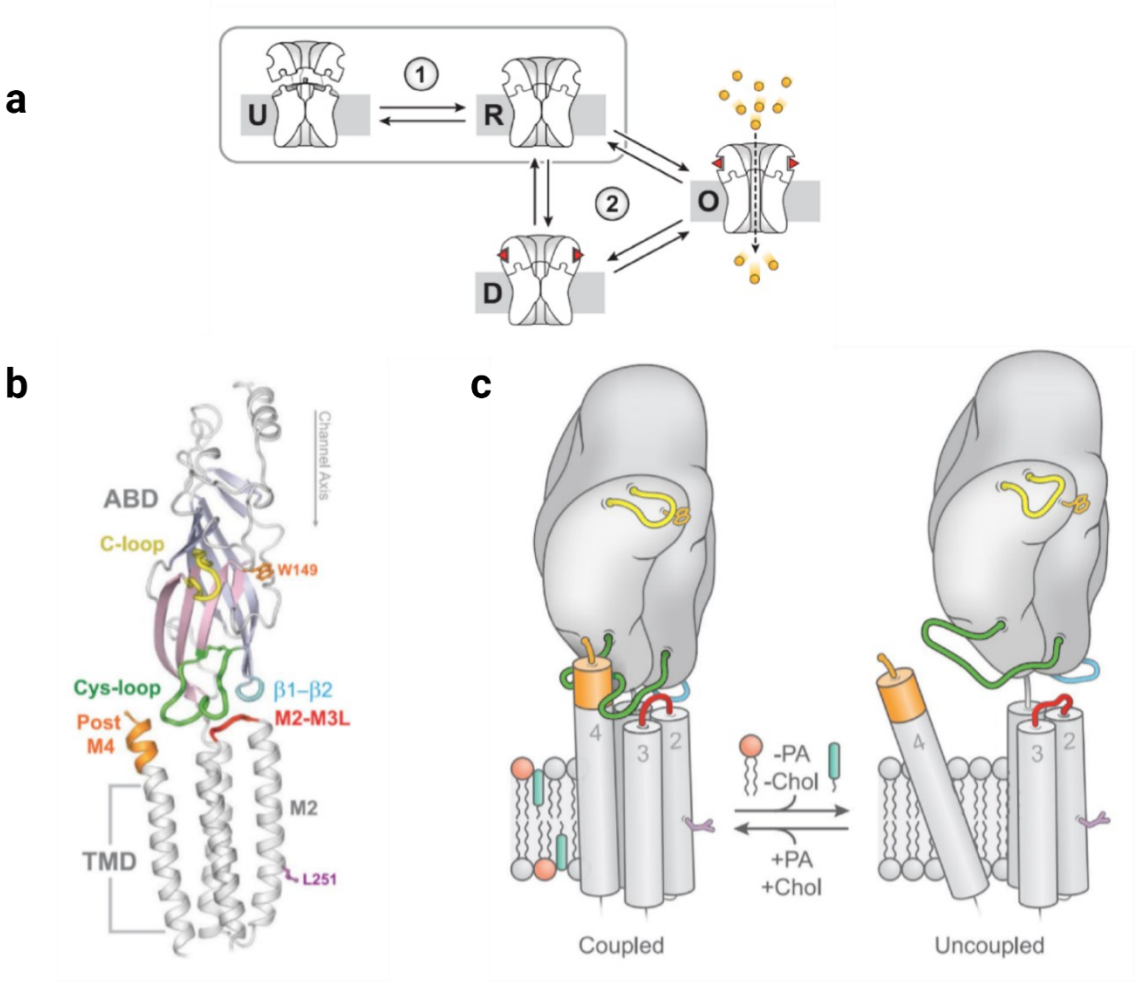
a
U
1
R
2
O
D
b
Channel Axis
ABD
C-loop
W149
Cys-loop
β1–β2
Post
M4
M2-M3L
M2
TMD
L251
c
4
3
2
-PA
-Chol
+PA
+Chol
Coupled
Uncoupled

After the uncoupled state was proposed, lipid modulation was initially interpreted in terms of an equilibrium between uncoupled (U) and coupled (R) conformations. This model was extended when the nAChR reconstituted in PC and PS membranes and was shown to be desensitized rather than resting, indicating that lipids shift the equilibrium not between two states but among the full set of functional conformations (daCosta & Baenziger, 2009). These findings collectively led to this broader conformational selection model in which lipids shift the equilibrium between functional receptor states (R, O, D, and U), with the U state predominating when activating lipids are absent (**Figure *1-6***). This model now provides the dominant interpretation of how lipids modulate nAChR function.

1.5.2 The lipid sensitivity of anion-selective pLGICs

Like the nAChRs, the activity of $GABA_A$Rs also depend on the surrounding membrane environment. Detergent-solubilized $GABA_A$Rs retain binding to GABA and benzodiazepine but lose pore-blocking binding (Schofield et al., 1988). Channel activity is only restored when brain lipid extract and cholesterol hemisuccinate (CHS) are included during solubilization or reconstitution (Bristow & Martin, 1987; Hayoundjian et al., 1986). Cholesterol depletion using methyl-β-cyclodextrin suppresses agonist-induced responses in hippocampal neurons. This effect is not rescued by the stereoisomer epicholesterol, indicating that the interaction is stereospecific (Bennett & Simmonds, 1996; Sooksawate & Simmonds, 2001a, 2001b). As observed with the nAChR, both increases and decreases in cholesterol levels impaired function, suggesting an optimal cholesterol range is required.

The most studied lipid modulators of $GABA_A$Rs are the neurosteroids, which are cholesterol-derived molecules that act through discrete sites within the TMD. Positive allosteric modulators (PAMs) such as allopregnanolone enhance $GABA_A$Rs inhibitory neurotransmission by increasing the open probability (p_{open}) and dwell time and, at higher

concentrations, directly gating the channel (Akk, Bracamontes, & Steinbach, 2004; Akk, Bracamontes, Covey, et al., 2004; Akk, Covey, et al., 2009; Akk et al., 2005, 2008; Akk, Li, et al., 2009; Belelli & Lambert, 2005; Bičiková, 2001; Majewska et al., 1986). In contrast, C3-sulfated and 3β-hydroxylated neurosteroids act as negative allosteric modulators that enhance desensitization. These bind at sites distinct from both positive neurosteroid sites and channel blockers (Akk et al., 2001; Eisenman et al., 2003; Majewska et al., 1986, 1988; Shen et al., 2000a, 2000b). Cryo-EM structures of $GABA_A$Rs in bound to allopregnanolone resolved two classes of neurosteroid binding sites within the TMD: an intrasubunit site at the M1-M4 interface and an intersubunit site between neighboring subunits (Laverty et al., 2017a; Miller, Scott, Masiulis, Colibus, et al., 2017). These structures confirmed that lipid-derived molecules can access specific, geometrically defined pockets within the TMD to directly influence gating.

The molecular basis of bulk lipid modulation of $GABA_A$Rs is less well understood. Molecular dynamics simulations suggest that lipids and lipophilic modulators stabilize TMD conformations that promote effective ECD-TMD coupling, similar to the mechanism proposed for the nAChR (daCosta & Baenziger, 2009; Kim et al., 2020; A. G. Lee, 2021a). Structural studies have identified a phosphatidylinositol 4,5-bisphosphate (PIP_2) binding site in the α1β3γ2 $GABA_A$R at the ECD-TMD interface, although functional data suggest a primary role for this interaction in receptor trafficking rather than direct modulation of channel gating (Laverty et al., 2019). At a cellular level, $GABA_A$Rs function has been linked to dynamic partitioning between cholesterol-rich and PIP_2-enriched membrane domains. Agonist binding drives a rapid and reversible receptor translocation between these domains that coincides with activation and desensitization (Yuan et al., 2025). This suggests that lateral lipid heterogeneity in the plasma membrane actively shapes $GABA_A$Rs behavior during synaptic signaling.

The lipid sensitivity of GlyRs has been less systematically studied. GlyRs purified from rat spinal cord and reconstituted into soybean azolectin membranes retain agonist-induced

anion flux (Riquelme et al., 1990). Single-channel conductance of both homomeric α_2 and heteromeric $\alpha_2\beta$ GlyRs appears similar in planar bilayers composed of brain-derived polar lipids or defined PE/PG mixtures (Yu et al., 2021a). Cholesterol depletion using methyl-β-cyclodextrin did not affect glycine-induced maximal current but suppressed potentiation by tetrahydrocannabinol, suggesting a modulatory role for cholesterol in GlyR gating (Yao, Liu, et al., 2020; Yao, Wells, et al., 2020). The M4 helix, the outermost TMD helix in direct contact with the surrounding lipids, has emerged as a critical determinant of GlyR function. M4-swapped chimeras between α1 and α3 subunits showed that subunit-specific agonist efficacy is largely defined by residues at the M4-lipid interface (Chen et al., 2009). M4 is also required for proper surface trafficking and participates in interactions with the neighbouring M1 and M3 helices that influence receptor folding and function (Haeger et al., 2009). These findings suggest that M4 may serve as a conserved lipid-sensing element across pLGICs, although the molecular details remain less well defined for the anion-selective family. Recent cryo-EM structures of full-length GlyRs in lipid nanodiscs have revealed distinct conformational states, with protein-lipid contacts varying across functional states, further supporting a role for lipids in shaping GlyR conformational dynamics (Dämgen & Biggin, 2021; A. Kumar et al., 2020a).

Across both $GABA_A$Rs and GlyRs, cholesterol and neurosteroids act through discrete TMD sites, and bulk lipid properties influence receptor distribution and conformational dynamics. The role of specific lipid-binding sites in modulating function, however, remains unknown.

1.5.3 The lipid sensitivity of prokaryotic pLGICs

ELIC and GLIC display distinct lipid sensitivities despite sharing the same conserved pLGIC architecture. Like the nAChR, ELIC does not respond to agonist in PC-only bilayers and is proposed to adopt an uncoupled or uncoupled-like conformation in this lipid

environment (Carswell, Hénault, et al., 2015; Carswell, Sun, et al., 2015; Hénault et al., 2019; Labriola et al., 2013). In contrast, GLIC retains agonist-induced conformational transitions in PC-only membranes. This difference has been attributed to the strength of M4-M1/M3 interactions within the TMD, which in GLIC are reinforced by an extensive network of aromatic residues absent in ELIC (Carswell, Sun, et al., 2015; Hénault et al., 2015; Therien & Baenziger, 2017). Introducing analogous aromatic residues into the ELIC M4-M1/M3 interface restores function in PC-only membranes, suggesting that the strength of M4-M1/M3 interactions determine lipid sensitivity (Carswell, Sun, et al., 2015; Labriola et al., 2013; Therien & Baenziger, 2017)

In ELIC, the lipid requirements for agonist response have been examined across several studies. Reconstitution of WT ELIC into PC-only membranes containing the anionic PG, or the zwitterionic PE, or both, restores a robust agonist-induced response and markedly slows desensitization on the tens-of-seconds timescale compared to reconstitution in asolectin that lacks PG and PE (Hénault et al., 2019; P. Kumar et al., 2021; Petroff et al., 2022; Tong et al., 2019). The effect of PG on desensitization was shown to be concentration-dependent. Increasing POPG content in liposomes from 0 to 25 mol% progressively decreases macroscopic desensitization (Tong et al., 2019). Consistent with a direct interaction, native mass spectrometry showed that POPG preferentially binds to ELIC over the zwitterionic lipids POPE and POPC, with up to eight lipid molecules resolved per pentamer. Lipid extraction from purified ELIC showed selective enrichment of PG relative to PE compared to the source *E. coli* membrane, indicating that ELIC actively selects for anionic lipids from a mixed membrane environment (Tong et al., 2019). The minimum lipid composition required for full ELIC agonist response, however, has not been systematically defined.

Cholesterol and docosahexaenoic acid (DHA) also modulate ELIC function, although with distinct phenotypes. Cholesterol slows ELIC desensitization (Hénault et al., 2019), while

DHA reduces peak agonist-induced current without altering agonist potency and competes with PG for binding, suggesting an inhibitory rather than activating role (N. M. Dietzen et al., 2022). The effects of these same lipids on GLIC are strikingly different: cholesterol accelerates rather than slows GLIC desensitization, and DHA either increases apparent desensitization rates or stabilizes a pre-active state with slower apparent desensitization (Basak et al., 2017; Gielen & Corringer, 2018a; Velisetty & Chakrapani, 2012). Together, these findings illustrate that even closely related prokaryotic pLGICs can respond to the same lipids in opposing ways, reflecting differences in their TMD architecture.

1.6 Mechanisms by which lipids influence ELIC function

The most detailed mechanistic understanding of how lipids influence pLGIC function has come from studies on ELIC. As described in the previous section, ELIC does not exhibit agonist-induced function in PC-only membranes. Cryo-EM structures of ELIC in this environment suggest that agonist binding leads to conformational changes in the ECD that propagate to the M2-M3 linker but fail to penetrate the remainder of the TMD (P. Kumar et al., 2020). This is consistent with the hypothesis that physical coupling between the ECD and TMD is lost in membranes lacking PE and PG, as described for the *Torpedo* nAChR (daCosta & Baenziger, 2009). Adding PG or PE to PC membranes restores robust agonist-induced responses and markedly slows desensitization, establishing that specific lipid interactions at the TMD are required for normal ELIC function (Hénault et al., 2019; P. Kumar et al., 2021; Tong et al., 2019).

The first direct structural evidence for lipid binding to ELIC came from a 2.5 Å crystal structure solved in 2019 by the Baenziger and Ulens groups (Hénault et al., 2019). Electron density for a bound lipid was resolved at the inner-leaflet at one M4-M1/M3 interface. This density was assigned to be PE, consistent with the fact that ELIC was crystallized in the

presence of an *E. coli* lipid extract that had 58 mol% PE during crystallization. This inner-leaflet lipid-binding site is shaped by three residues, Trp224 on M1, Arg301 on M4, and Pro305 on M4, forming the W-R-P motif. Arg301 forms a cation-π interaction with Trp224, while Pro305 introduces a kink in M4 that opens a pocket for inner-leaflet lipids (Cordes et al., 2002; Hénault et al., 2019; P. Kumar et al., 2021; Tong et al., 2019). In parallel, native mass spectrometry and molecular modelling from the Cheng group showed that the inner-leaflet site and an outer-leaflet site accommodate PG with a higher apparent affinity than for PE (Tong et al., 2019).

Four findings support a model whereby the binding of either PE (Hénault et al., 2019) or PG (P. Kumar et al., 2021) to the W-R-P pocket slows ELIC desensitization by altering the dynamics or position of M4 relative to M1 and M3. First, reconstituting wild-type ELIC into membranes lacking PE and PG leads to a fast-desensitizing phenotype, indicating that PE and/or PG modulate the rates of desensitization. Second, mutations, such as P305A, that should favour a non-kinked conformation of M4 that obstructs lipid binding, accelerate ELIC desensitization. In fact, shifting the P305-induced kink either up or down by one helical turn (on the P305A background) also accelerates desensitization, although to a lesser extent. Third, deleting the last eight or more C-terminal residues results in a similar fast-desensitizing phenotype. Of note, the Δ8M4 ELIC crystal structure lacks density for the entire M4 α-helix, thus implicating increased M4 dynamics with the fast-desensitizing phenotype. Finally, several structures of ELIC in the Protein Data Bank (PDB) exhibit density corresponding to M4 in both kinked and unkinked conformations, suggesting that M4 naturally oscillates between the two conformations (Gonzalez-Gutierrez et al., 2012; Zimmermann & Dutzler, 2011). Taken together, these observations support a model whereby lipid binding to the W-R-P pocket stabilizes a kinked conformation of M4 and constrains its motion relative to M1 and M3, slowing the rates of desensitization. Whether the relevant change is in M4 dynamics, in the

Figure 1-7 Lipid-binding to the W-R-P motif influence ELIC desensitization.

a. (Left) structure of ELIC with a bound lipid (PDB: 6HJX). ELIC is shown as a white surface with two subunits highlighted in cartoon representation and colored by transmembrane helices: M1 yellow, M2 green, M3 pink, and M4 blue. The inset highlights the intracellular lipid-binding pocket formed by the W224, R301, and P305 residues. (Top right) electrophysiological recordings of purified ELIC reconstituted into vesicles of defined lipid composition. Each condition represents 4 to 26 independent experiments, with desensitization time constants (τ) reported as mean ± S.E.M. (Bottom right) representative TEVC traces recorded from *Xenopus laevis* oocytes expressing wild-type ELIC and the fast-desensitizing ΔM4 mutant in response to 6 mM cysteamine. **b.** Whole-cell TEVC recordings from oocytes expressing M4 proline-shifted ELIC mutants, illustrating the effect of altered M4-kink position on desensitization kinetics. **c.** Cartoon putty representations of the ELIC 7′C structure and the ELIC Δ8 C-terminal deletion mutant, both in complex with Nb72 (not shown). Residues are colored according to average B-factor values, ranging from 25 $Å^2$ in blue to 250 $Å^2$ in red. Increased flexibility of the M4 helix and M3-M4 linker in the Δ8 mutant is indicated by the gray dashed line.

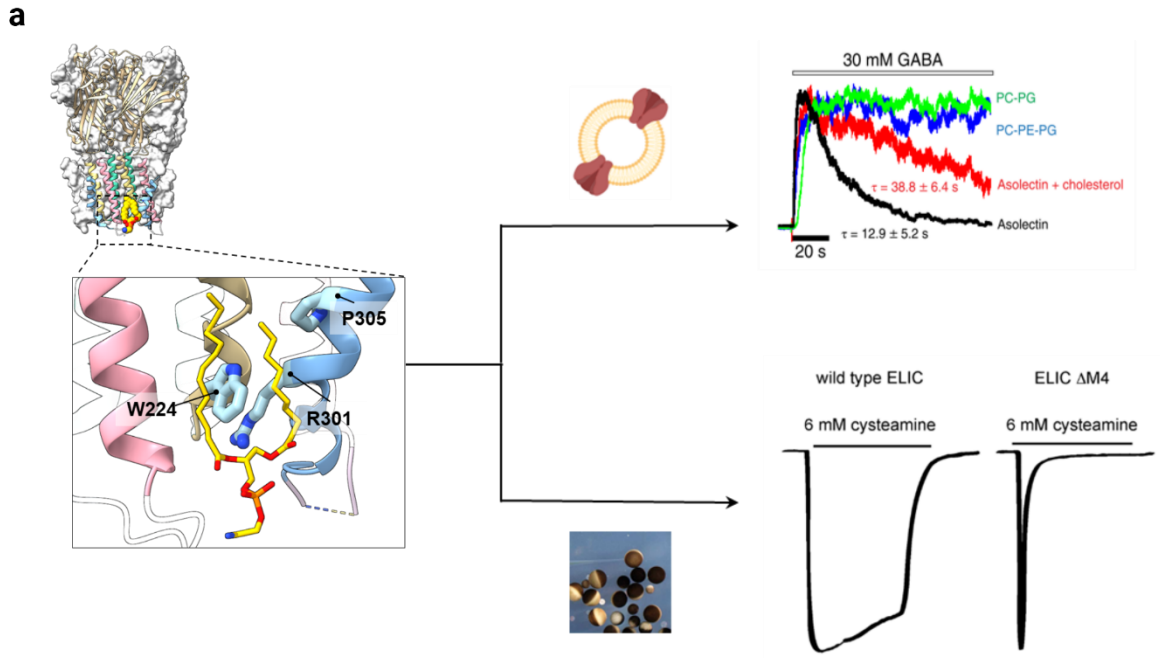
a
P305
W224
R301
30 mM GABA
PC-PG
PC-PE-PG
τ = 38.8 ± 6.4 s
Asolectin + cholesterol
Asolectin
τ = 12.9 ± 5.2 s
20 s
wild type ELIC
ELIC ΔM4
6 mM cysteamine
6 mM cysteamine

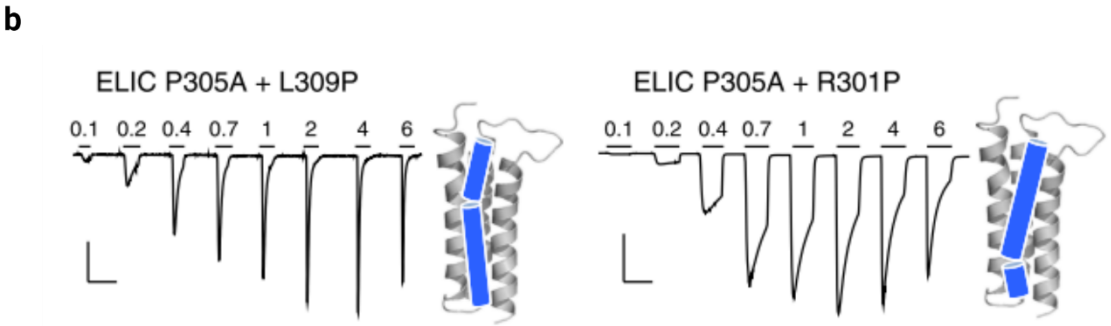
b
ELIC P305A + L309P
0.1 0.2 0.4 0.7 1 2 4 6
ELIC P305A + R301P
0.1 0.2 0.4 0.7 1 2 4 6

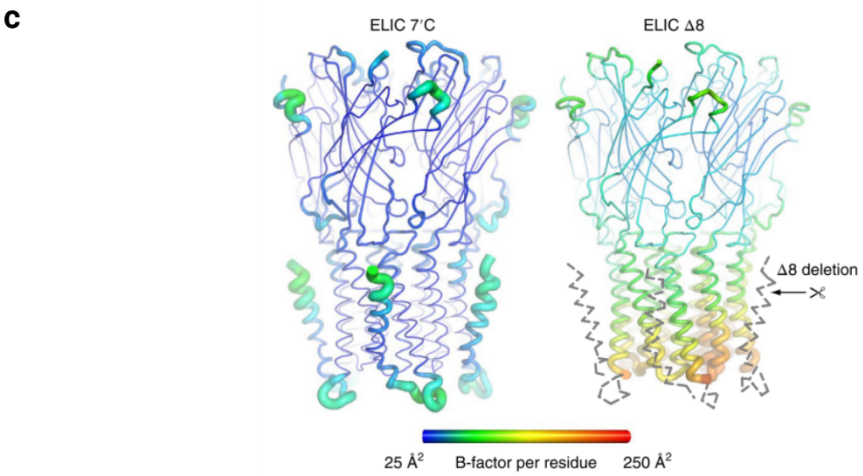
c
ELIC 7′C
ELIC Δ8
Δ8 deletion
25 Å²
B-factor per residue
250 Å²

Figure 1-8 The proposed M4 dynamics model for modulating ELIC desensitization .

Proposed model for lipid-dependent modulation of channel desensitization. M4 helix is conformationally dynamic between a Pro305-induced kinked and an unkinked conformation, with enhanced M4 dynamics correlating with enhanced rates of desensitization.

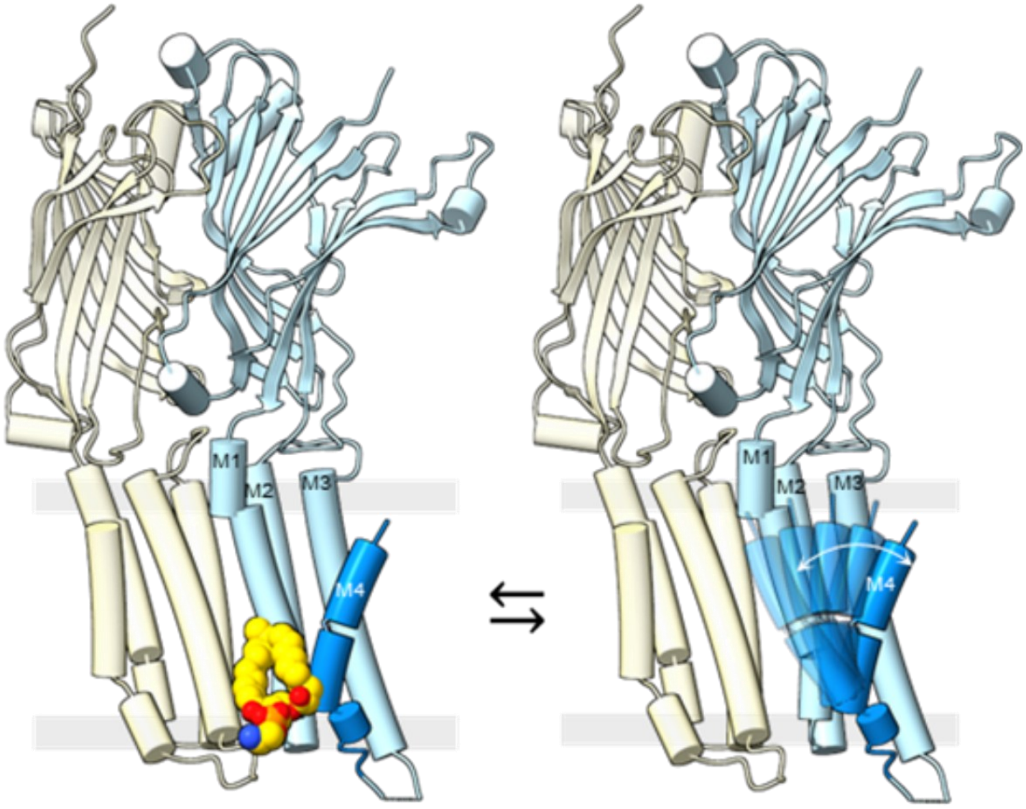
M1
M2
M3
M4
M1
M2
M3
M4

position of M4 relative to M1 and M3, or in both, cannot be distinguished from these observations alone.

As noted above, research from the Cheng group suggests that PG binds to ELIC at both inner- and the outer-leaflet sites (Tong et al., 2019). At the inner-leaflet site, three arginines at the M3-M4 interface (Arg286, Arg299, and Arg301) contribute to PG binding, with Arg301 being the W-R-P arginine itself. Notably, detergent molecules were resolved at the same ECD-TMD site in the 2019 ELIC x-ray structure, confirming that the W-R-P pocket and the binding site characterized by native MS overlap (Hénault et al., 2019). Mutating these arginines reduced PG binding and accelerated ELIC desensitization, while an unrelated mutation (L238A) that slowed desensitization increased PG binding by approximately 1.7-fold. Together, these results support a direct link between PG binding at the W-R-P pocket and the rate of ELIC desensitization (Tong et al., 2019).

Later, cryo-EM structures of ELIC extracted directly from *E. coli* membranes using styrene-maleic acid (SMA) confirmed PG binds at the same inner-leaflet site in each of the five subunits. These structures also revealed cardiolipin bound at an intersubunit site in the outer-leaflet, with its four acyl chains extending toward both the M4-M3 interface of the principal subunit and down through the bilayer toward the inner-leaflet, adding to the evidence of a consistent lipid binding site in the outer-leaflet (Kumar et al., 2021).

Following up on these results, a distinct but adjacent lipid interaction involving Trp206 at the top of M1 was identified at the outer-leaflet of the TMD. Using unnatural amino acid mutagenesis with progressively fluorinated tryptophan derivatives, Sridhar et al. demonstrated a cation-π interaction between Trp206 and zwitterionic lipid headgroups in the resting state, with a strong linear correlation between agonist EC_{50} and cation-π binding energy. Molecular dynamics simulations showed that PC headgroups contact Trp206 within cation-π interaction

distances in the resting state, while PG headgroups do not, suggesting that the resting-state outer-leaflet site preferentially engages zwitterionic lipids. The homologous aromatic residue was identified in the human $GABA_AR$ ε subunit, where equivalent mutations altered the GABA EC_{50}, pointing to a conserved outer-leaflet lipid interaction across the pLGIC family (Sridhar et al., 2021).

The structural basis for outer-leaflet lipid modulation was further advanced by Cheng group who solved the first open-channel cryo-EM structure of any pLGIC with a bound phospholipid (Petroff et al., 2022). Using an engineered non-desensitizing ELIC mutant (ELIC5) reconstituted into lipid nanodiscs, a 3.4 Å structure captured an open-channel conformation with a phospholipid headgroup positioned at the outer-leaflet intersubunit groove formed by M4, M3, and M1, adjacent to the β6-β7 loop and within contact distance of Arg117. Consistent with the Sridhar et al. findings, Trp206 was found to undergo a conformational switch upon activation: in the resting state it faces outward into the bilayer, but upon channel opening it rotates into the intersubunit space, restructuring the site from one that favours zwitterionic lipids to one that accommodates anionic lipids. Alchemical free energy calculations suggest that PG binds with greater affinity to the open-channel conformation than to the resting state (Petroff et al., 2022). These calculations depend on assumptions about the conformational state of the protein during binding and on the accuracy of the force fields used. Of note, the same study also reported that M4 density is weaker in non-conducting structures than in the open-channel ELIC5 structure, with M4 straightening and tilting outward upon channel opening. This is an independent cryo-EM evidence that M4 is conformationally dynamic and that its dynamics correlate with the gating state, consistent with the M4 dynamics model. These findings support the view that PG acts as a state-dependent ligand that preferentially stabilises the open channel, thereby slowing the transition to the desensitized state. To test which leaflet mediates this modulation, Petroff et al. used asymmetric liposomes

Figure 1-9 Outer leaflet lipid-binding site in ELIC5 and conformational changes associated with channel opening.

a. Left: Extracellular view of the ELIC5 transmembrane domain (TMD) showing POPG (yellow) resolved within the electron density map (green mesh). Right: Side view of the ELIC5 phospholipid-binding site, showing POPG (yellow) within the electron density map (green mesh). The R117 side chain is shown for reference. **b.** Top: Overlay of the β6-β7 loop and M2-M3 linker in wild-type (WT) apo, WT cysteamine-activated (CA), and ELIC5 CA structures. The W206 side chain is shown for each structure. Bottom: Top-down view of the same overlay, highlighting conformational differences in the M2-M3 linker and W206 across the three structures. **c.** Extracellular view of the TMD helices at the 9' position, comparing WT CA and ELIC5 CA. Distances between C-α atoms of each transmembrane helix are shown in red. Figure adapted from Petroff et al. (2022).

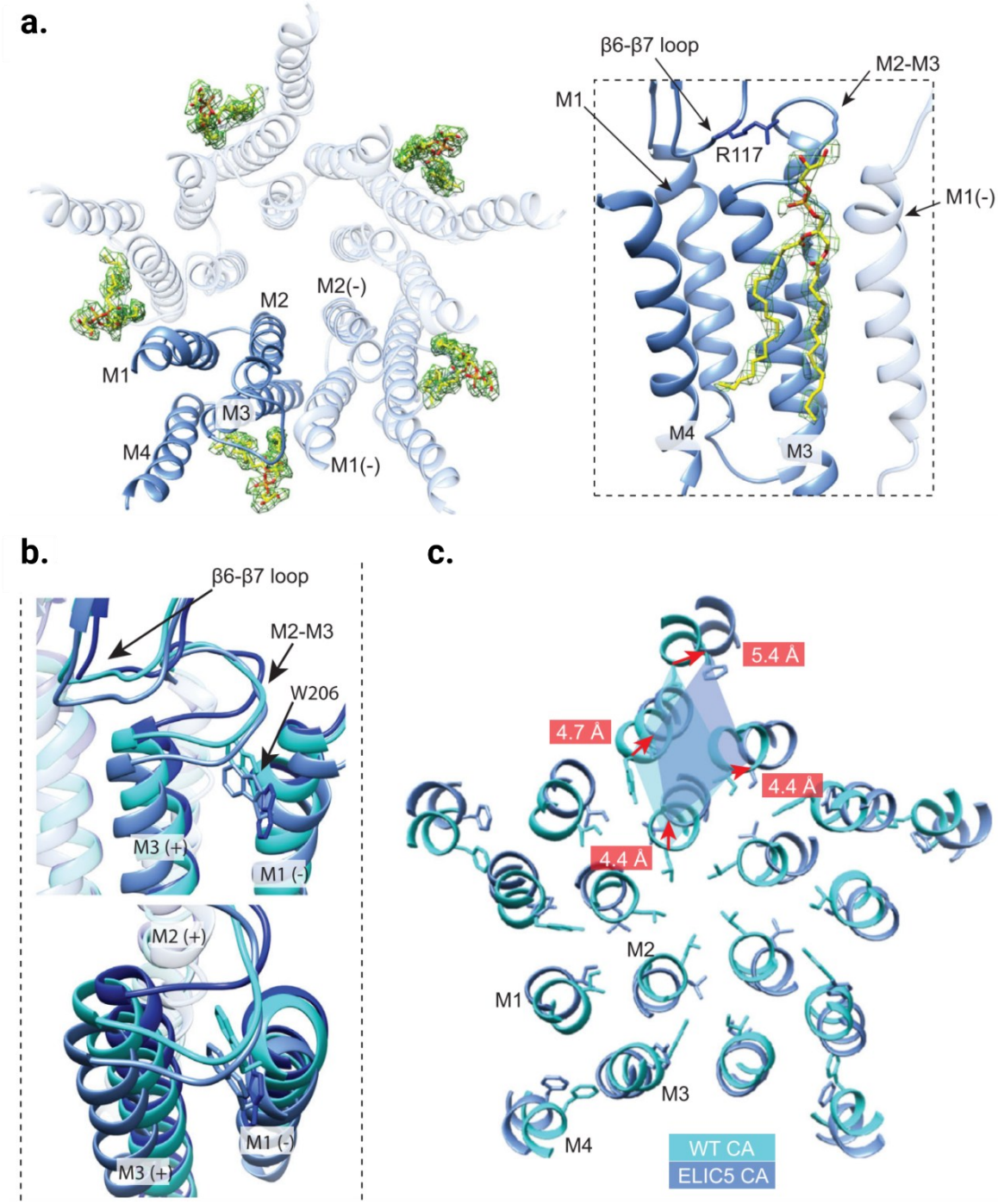
a.
β6-β7 loop
M2-M3
M1
R117
M1(-)
M2(-)
M2
M1
M3
M4
M1(-)
M4
M3
b.
β6-β7 loop
M2-M3
W206
M3 (+)
M1 (-)
M2 (+)
M1 (-)
M3 (+)
c.
5.4 Å
4.7 Å
4.4 Å
4.4 Å
M2
M1
M3
M4
WT CA
ELIC5 CA

in which PG was restricted to either the inner- or outer-leaflet. Introducing PG to the outer-leaflet alone was sufficient to increase peak agonist response and reduce desensitization, demonstrating that the outer-leaflet site is the primary site of functional modulation. This experiment, however, tested only PG and was performed in the ELIC5 background, which does not desensitize like WT ELIC. Whether the outer-leaflet site is sufficient for the modulation observed with PE or CL, and whether the same conclusion holds in WT ELIC, is not addressed by this assay.

The functional mechanisms of other lipid species at ELIC have also been studied. Studies showed that DHA, a polyunsaturated fatty acid, inhibits ELIC through two distinct TMD binding sites and that PG competes with DHA at one of these sites, suggesting that the outer-leaflet intersubunit groove can accommodate structurally diverse lipid-like molecules with opposing functional effects. These findings raise the possibility that the modulatory effects of specific membrane lipids on ELIC reflect competition and selectivity at shared binding sites, rather than independent allosteric mechanisms (N. M. Dietzen et al., 2022).

More recent pre-prints have examined the contribution of cardiolipin and PE to ELIC activation. CL and PE were shown to support robust ELIC activation in liposomes, while ELIC5 in PC-only membranes showed reduced peak agonist responses and increased structural heterogeneity in the resting state, with conformations that partially resembled agonist-induced changes even in the absence of agonist. Cryo-EM structures identified CL binding at an outer-leaflet M3-M4 intersubunit site. Together, these data suggest that CL and PE stabilize a properly poised resting state that can efficiently transition to the open channel upon agonist binding, while PG preferentially stabilizes the open state itself. In this way, different lipid species may act on different gating transitions through binding at overlapping sites on the outer-leaflet TMD periphery (Tan et al., 2025).

An additional consideration is the influence of the reconstitution environment on structural conclusions. Nanodisc scaffold type and size were shown to systematically alter ELIC structures, with effects extending from the TMD to the agonist-binding site in the ECD (Dalal et al., 2024). Subsequent cryo-EM structures solved with ELIC reconstituted in liposomes showed a more loosely packed TMD, with M4 shifted outward by approximately 1 Å compared to nanodisc structures (Dalal et al., 2025). These findings are an important caution for interpreting lipid-dependent structural changes observed in nanodisc-based studies.

Taken together, these studies show that ELIC function depends on lipid interactions at the TMD periphery, with the M4 helix playing a central role in lipid modulation of channel function. The inner-leaflet W-R-P pocket and the outer-leaflet intersubunit groove represent two distinct lipid-binding sites that influence different aspects of ELIC function. Lipids at the inner-leaflet site are proposed to act primarily by governing M4 conformational dynamics and the rate of desensitization, while lipids at the outer-leaflet site are proposed to modulate both the stability of the resting state and the propensity for the open channel to desensitize. Structural evidence supports M4 conformational dynamics: ELIC crystal structures show M4 in both kinked and unkinked conformations across different deposits (Gonzalez-Gutierrez et al., 2012; Zimmermann & Dutzler, 2011), the Δ8 ELIC structure lacks density for the M4 helix entirely (Hénault et al., 2019), and cryo-EM density for M4 is weaker in non-conducting WT structures than in the open-channel ELIC5 structure, with M4 straightening and tilting outward upon activation (Petroff et al., 2022). The reconstitution environment also affects M4 tilt, with M4 shifted outward in liposomes compared to nanodiscs (Dalal et al., 2024, 2025).

The two groups have assessed lipid modulation of ELIC from different angles. The M4 dynamics model places the W-R-P pocket and M4 dynamics at the centre of the mechanism that tunes ELIC desensitization (Hénault et al., 2019). Work from the Cheng group has focused on the outer-leaflet site and on how lipids stabilize different gating states, with the asymmetric

liposome experiment in the ELIC5 background showing that outer-leaflet PG alone is sufficient to reduce desensitization by stabilizing the open state (Petroff et al., 2022; Tan et al., 2025). Earlier work from the Cheng group identified inner-leaflet Arg residues as critical for PG binding and showed that mutations at these residues accelerate desensitization (Tong et al., 2019), supporting a functional role for the inner-leaflet site as well. The two sites likely act on different functional transitions: the outer-leaflet site appears to influence channel activation and the stability of the open state, while the W-R-P pocket has been linked specifically to the rate of desensitization through M4 dynamics. Whether the two sites act independently, sequentially, or in coordination is an open question. In this thesis, I take a deeper dive into how the W-R-P pocket and the surrounding M4-M1/M3 interface shape desensitization, both across the pLGIC family and within ELIC.

1.7 Summary and thesis objectives

The goal of my thesis has been to gain a deeper understanding of how membrane lipids influence pLGIC activity, with a particular focus on TMD interactions that shape channel desensitization. I chose to focus on the W-R-P motif and the M4-M1/M3 interface in ELIC. I use two-electrode voltage clamp (TEVC) electrophysiology in *Xenopus laevis* oocytes to measure desensitization across mutants in ELIC, the α1 GlyR, and GLIC. I also test the M4 dynamics model proposed for ELIC and ask whether the same mechanism operates in other pLGICs that share the W-R-P motif.

The W-R-P motif is conserved in eukaryotic anion-selective pLGICs, such as $GABA_AR$ and GlyR, as well as in the prokaryotic pLGIC, GLIC (**Figure *1-10***). The W-R-P pocket overlaps with binding sites for neurosteroids in α1- or α5-based $GABA_AR$ chimeras (Laverty et al., 2017b; A. G. Lee, 2021b), neurosteroids and PC binding in α1 $GABA_ARs$ (Sun et al., 2023), PC in GLIC (Bocquet, Nury, Baaden, Le Poupon, et al., 2009), and cannabinoids and phospholipid fragments in α1 GlyRs (A. Kumar et al., 2022a; Yu et al., 2021b). The W-R-P motif also lies adjacent to residues implicated in the desensitization of anion-selective pLGICs (Gielen et al., 2015b; Gielen & Corringer, 2018b), which are thought to influence desensitization rates through closure of a cytoplasmic desensitization gate. The proximity of the W-R-P pocket to this proposed gate raises an alternative possibility that mutations or lipid binding at this site could affect desensitization independently of M4. The conservation of the W-R-P motif across both anion-selective pLGICs and GLIC, the demonstrated binding of both neurosteroids and lipids to the W-R-P pocket of anion selective pLGICs and GLIC, and the extensive data suggesting that lipid binding to the W-R-P pocket in ELIC alters desensitization via effects on M4 dynamics collectively raise the possibility that lipid binding to pLGICs containing a W-R-P motif influences desensitization via a similar mechanism of action to that proposed for ELIC.

The overarching hypothesis of this thesis is that the W-R-P pocket plays a conserved role in modulating desensitization across ELIC, GLIC, and anionic pLGICs; and that lipid binding to the W-R-P pocket in ELIC modulates channel desensitization by tuning M4 structure or dynamics through specific interactions at the M4-M1/M3 interface.

In Chapter 2, I describe the materials and methods used in this work, including the analysis approaches used to quantify desensitization across mutants in this thesis.

In Chapter 3, I test whether the W-R-P pocket plays a conserved role in modulating desensitization across pLGICs that share the motif. I compare the effects of mutations to the W-R-P motif, the W-R-P pocket, the Pro-kink position, and the M4 C-terminus on desensitization in ELIC, α1 GlyR, and GLIC. The results show that the W-R-P pocket plays different roles in modulating desensitization across the three receptors, and that the broader architecture of the M4-M1/M3 interface, in particular the density of aromatic interactions at this interface, shapes how mutations to the W-R-P pocket influence desensitization across pLGICs.

In Chapter 4, I focus on ELIC and examine how interactions at the M4-M1/M3 interface modulate desensitization. I test the contribution of the Trp224-Arg301 cation-π interaction on desensitization by eliminating, weakening, and reversing it. I also test how additional aromatic interactions at the M4-M1/M3 interface, and other interactions surrounding the Pro305 kink, modulate desensitization rates. The results show that the strength of interactions at the M4-M1/M3 interface modulates the rate of ELIC desensitization and identify the Trp224-Arg301 cation-π interaction at the W-R-P motif and the Pro305 kink as distinct features that contribute to slow desensitization.

In Chapter 5 I summarize the main findings of the thesis and discuss future experiments to extend this work. Finally, Chapter 6 lists the thesis references and Chapter 7 is the appendix.

Figure 1-10 The W-R-P pocket is conserved.

a. Structure of ELIC with a bound lipid (PDB: 6HJX). Left side: side view of ELIC represented as white surface with two subunits highlighted as cartoon colored by α- helices: M1 yellow; M2, green; M3, pink; M4, blue. Right side: Top-down view of the TMD. **b.** (left) Cartoon/sticks representation of the lipid-binding site in ELIC. The W-R-P triad residues are highlighted in light blue sticks (carbon). Lipid is shown in yellow (carbon) (middle) PC bound to GLIC (PDB: 3EAM). (right) Potentiating neurosteroid tetrahydrodeoxycorticosterone (THDOC) bound to the α1 $GABA_AR$ (PDB: 5OSB). **c.** Sequence alignment of residues forming the lipid binding site in ELIC. The sequence alignment shows highly conserved residues of the lipid binding site in ELIC and compared to anion-selective eukaryote pLGICs. Residues of the W-R-P triad are highlighted in blue.

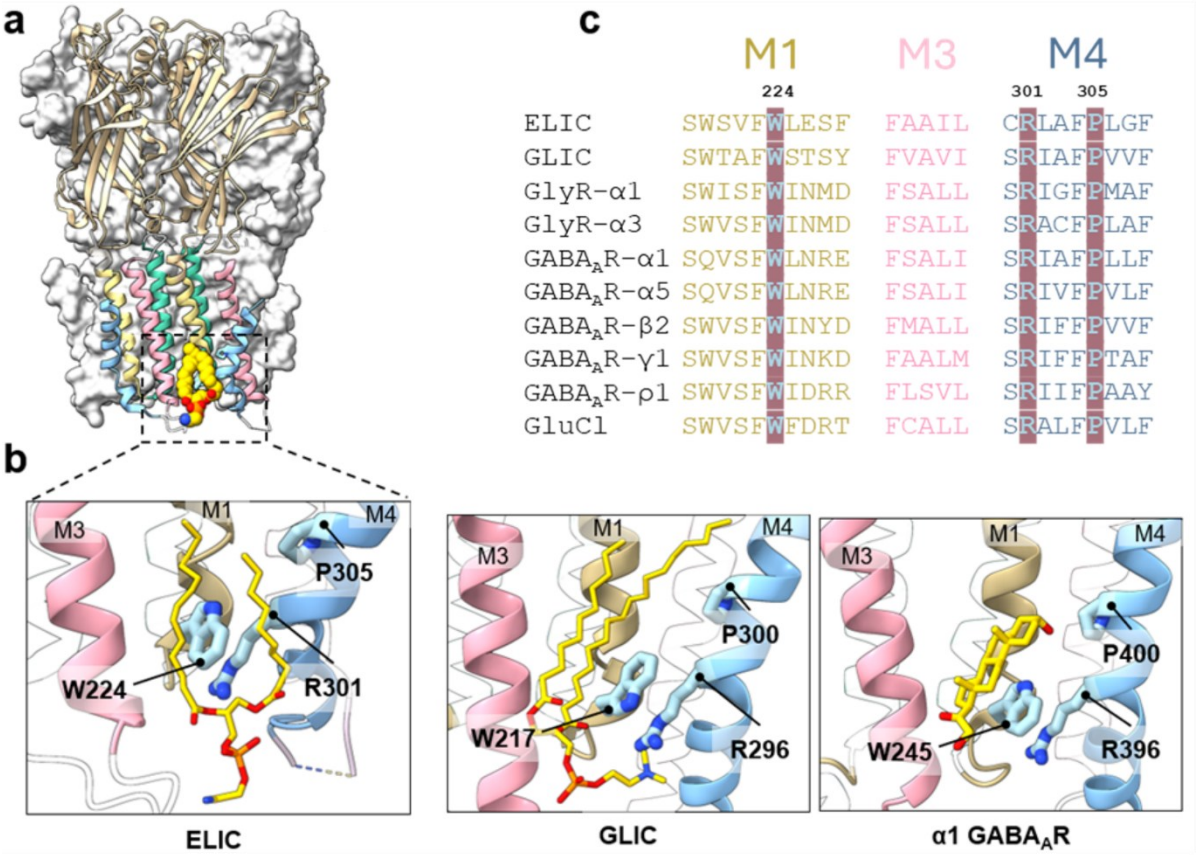
a
b
c
M1
M3
M4
224
301
305
ELIC SWSVFWLESF FAAIL CRLAFPLGF
GLIC SWTAFWSTSY FVAVI SRIAFPVVF
GlyR-α1 SWISFWINMD FSALL SRIGFPMAF
GlyR-α3 SWVSFWINMD FSALL SRACFPLAF
GABA$_A$R-α1 SQVSFWLNRE FSALI SRIAFPLLF
GABA$_A$R-α5 SQVSFWLNRE FSALI SRIVFPVLF
GABA$_A$R-β2 SWVSFWINYD FMALL SRIFFPVVF
GABA$_A$R-γ1 SWVSFWINKD FAALM SRIFFPTAF
GABA$_A$R-ρ1 SWVSFWIDRR FLSVL SRIIFPAAY
GluCl SWVSFWFDRT FCALL SRALFPVLF
M3
M1
M4
P305
W224
R301
ELIC
M3
M1
M4
P300
W217
R296
GLIC
M3
M1
M4
P400
W245
R396
α1 GABA$_A$R

2 Chapter 2 – Experimental Methods

2.1 Cloning of human α1 GlyR and human ρ1 $GABA_AR$ into oocyte expression vector

The cDNA encoding both the human α1 GlyR and the human ρ1 $GABA_AR$ constructs were first cloned into the pcDNA3.1 expression vector for heterologous expression in *Xenopus laevis* oocytes. Primers were designed using a PCR-based cloning method to introduce restriction sites compatible with the pcDNA3.1 vector. Because several commonly used restriction sites were present within the receptor coding sequences, Acc65I (G^GTACC) was selected for insertion at the 5′ end and NotI (GC^GGCCGC) at the 3′ end of each cDNA, as both sites were unique within the receptor sequences and available in the vector multiple cloning site.

PCR amplification generated inserts containing the desired restriction sites, which were assembled into the pcDNA3.1 backbone using a Gibson assembly protocol. During cloning, digestion of the pcDNA3.1 vector with Acc65I was unsuccessful. This was attributed to methylation of the Acc65I recognition sequence due to overlap with a Dcm methylation site (CC*TGG) in plasmid DNA propagated in Escherichia coli.

To overcome this issue, the full-length pcDNA3.1 vector was amplified by PCR using primers available in the laboratory, generating methylation-free DNA. The resulting PCR product was then used for Gibson assembly with the receptor inserts. Using this approach, both α1 GlyR and ρ1 $GABA_AR$ constructs were successfully generated and expressed as functional receptors in *Xenopus laevis* oocytes (see below). All constructs were confirmed by Sanger sequencing performed at the Université Laval (uLaval) sequencing facility.

2.2 Site-directed mutagenesis and cRNA preparation of ELIC, GLIC, α1 GlyR and the ρ1 $GABA_AR$.

GLIC-pMT3 was kindly provided by Dr. Pierre-Jean Corringer (Bocquet, Nury, Baaden, Poupon, et al., 2009). The GLIC coding sequence was subcloned into pSP64 without the C-terminal hemagglutinin tag (GLIC-pSP64). ELIC-pTLN was kindly provided by Dr. Raimund Dutzler (Zimmermann et al., 2012). In both constructs, the receptor coding sequence is preceded by the α7 nAChR signal sequence.

For cRNA preparation, GLIC-pSP64 and ELIC-pTLN were linearized with MluI and capped cRNA was synthesized by *in vitro* transcription using the mMESSAGE mMACHINE® SP6 kit (Ambion). The α1 GlyR and ρ1 $GABA_AR$ constructs were linearized with MluI and used to generate capped cRNA using the mMESSAGE mMACHINE® T7 kit (Ambion).

All mutations were introduced into the corresponding wild-type constructs using QuikChange site-directed mutagenesis kits (Agilent) and verified by Sanger sequencing (uLaval).

2.3 Animal Protocol

Ovulating female *Xenopus laevis* were purchased from Nasco (Fort Atkinson, Wisconsin), and later Xenopus1 (Dexter, Michigan), and were housed in the Animal Care and Veterinary Service (ACVS) of University of Ottawa, Faculty of Medicine. The experimental protocol involving the use of these animals has been approved by the Animal Care Committee of University of Ottawa under the protocol BMIe-4328. Ovulating females were anesthetized by immersion in water containing MS-222 (3-aminobenzoic acid ethyl ester methane sulfonate salt, 2g per liter of water). After 20 minutes of immersion, a pinch test was performed to confirm the frog was fully anesthetized. Sacrifice was performed by guillotine, followed by pithing. An incision was made through the skin in the lower half of the anterior abdominal wall,

to both sides of the midline. The connective tissue and muscle layer under the skin were also opened using small scissors, creating an incision into the coelomic cavity. Ovaries were then extracted using a pair of forceps and transferred to a falcon tube containing ND96 buffer (5 mM HEPES, 96 mM NaCl, 2 mM KCl, 1 mM $MgCl_2$, 2 mM pyruvate, pH 7.0). The carcass was stored at -20°C until disposal by incineration.

To obtain individual oocytes for electrophysiology, oocyte lobes were cut into smaller fragments using scissors and defolliculated enzymatically using defolliculation buffer (ND96 buffer, 1 mg/mL collagenase B (Millipore Sigma), and 1 mg/mL trypsin inhibitor (ThermoFisher Scientific) for 2 hours at room temperature under constant stirring. The defolliculation buffer was gradually removed by washing the oocytes in $ND96^+$ buffer (5 mM HEPES, 96 mM NaCl, 2 mM KCl, 1 mM $MgCl_2$, 1 mM $CaCl_2$, 2 mM pyruvate, pH 7.0) for several iterations. The oocytes were allowed to stir for an additional hour at room temperature under constant stirring with the buffer being periodically replaced until clear. Healthy oocytes were then individually selected from this collection for cRNA injection.

2.4 Electrophysiology

2.4.1 Two-electrode voltage clamp (TEVC) recordings

Defolliculated stage V-VI *Xenopus laevis* oocytes were injected with the appropriate amount of cRNA and allowed to incubate for 2-7 days at 16°C, as described elsewhere (Carswell, Sun, et al., 2015). Whole-cell currents of ELIC, GLIC, GlyR, or GABA were measured in response to either cysteamine, pH, glycine, or GABA concentration jumps using a TEVC apparatus, respectively (OC-725C oocyte clamp; Harvard Apparatus, Holliston, MA).

Whole-cell recordings were performed in the following solutions: ELIC in HEPES buffer (10 mM HEPES, 150 mM NaCl, 0.5 mM $BaCl_2$, and 1 mM DTT, pH 7.0); GLIC in MES buffer (10 mM MES, 140 mM NaCl, 2.8 mM KCl, and 2 mM $MgCl_2$, pH 7.0); α1 GlyR in

HEPES buffer (5 mM HEPES, 96 mM NaCl, 2 mM KCl, 1.8 mM $CaCl_2$, and 1 mM $MgCl_2$, pH 7.5); and ρ1 $GABA_AR$ in $ND96^+$ buffer (5 mM HEPES, 96 mM NaCl, 2 mM KCl, 1 mM $MgCl_2$, 1 mM $CaCl_2$, 2 mM pyruvate, pH 7.0). The membrane potential was clamped at -20 mV for ELIC and GLIC, and -40 mV for α1 GlyR and ρ1 $GABA_AR$. Solutions were perfused through the oocyte chamber at 10-12 mL/min.

Dose-response data were collected from at least two independent oocyte batches from different frogs, with at least 8 oocytes per construct or condition unless otherwise stated. Individual dose-response curves were fit with a variable-slope sigmoidal function using GraphPad Prism. The half-maximal effective concentration (EC_{50}) and Hill coefficient were determined for each experiment, and values were averaged and reported as mean ± standard deviation (S.D.). For the presented dose-response curves, the individual dose responses were normalized prior to averaging; averaged data are shown with standard error, and fits to the averaged data are presented. Statistical significance of EC_{50} values and Hill coefficients was assessed using a one-way analysis of variance (ANOVA), followed by Dunnett's post hoc test. Analysis of desensitization is discussed in detail in the next section.

2.5 Quantitative analysis of desensitization

Macroscopic desensitization is the decay of the whole-cell current observed during sustained agonist application in TEVC recordings (**Figure *2-1***). As my thesis primarily examines the effect of different mutants on the rate of macroscopic desensitization, the first step was to establish a quantitative method that assesses both the rate and extent of desensitization from each whole-cell current recording at each studied agonist concentration. To do so, I used two approaches to quantify desensitization: the current decay time constant (τ), which measures the rate of current decay, and the extent of desensitization (%Des), which measures how much the current decays during a defined agonist application. τ is derived from exponential curve fitting and is the primary measure used to compare desensitization rates

across constructs. %Des is the fractional current decay measured between the peak response and the end of the recording, measured from the trace at a defined time point rather than at equilibrium. Recording times differed by experiment: concentration-response recordings used 30s applications, and the single-concentration comparisons in Chapter 4 used 1-minute applications. These two approaches are described below.

2.5.1 Estimation of current decay time constant (τ)

To estimate the macroscopic desensitization rate at each agonist concentration, the region of the trace corresponding to the current decay was fit in GraphPad Prism to the single exponential equation (**Eq. [1]**):

$$\textbf{Eq. [I]} \qquad y = (y_0 - plateau)\mathrm{e}^{(-Kx)} + \textbf{plateau}$$

where y_0 is the y value at time zero (corresponding to the peak current), K is the rate constant for the decay, τ (= 1/K) is the time constant, and the Span (= y_0 - plateau) is the total amplitude of the decay. The plateau represents the predicted y value at infinite time, estimated by Prism by extrapolating the fitted curve beyond the recorded data. **Figure *2-1*** illustrates the components of the fit on a representative trace.

Figure 2-1 Schematic of the single-exponential decay fit applied to TEVC desensitization currents.

(left) Schematic whole-cell trace showing the baseline, agonist-induced peak current, decay during sustained agonist application, and recovery after agonist removal. The shaded region indicates the decay portion of the trace selected for fitting. (right) Ideal exponential fit to the selected decay region. Black circles represent the experimental data, and the red line represents the fitted curve. An ideal fit returns $R^2 = 1.00$, a well-defined τ within the agonist application time, and a plateau value that corresponds to the predicted extent of desensitization at equilibrium.

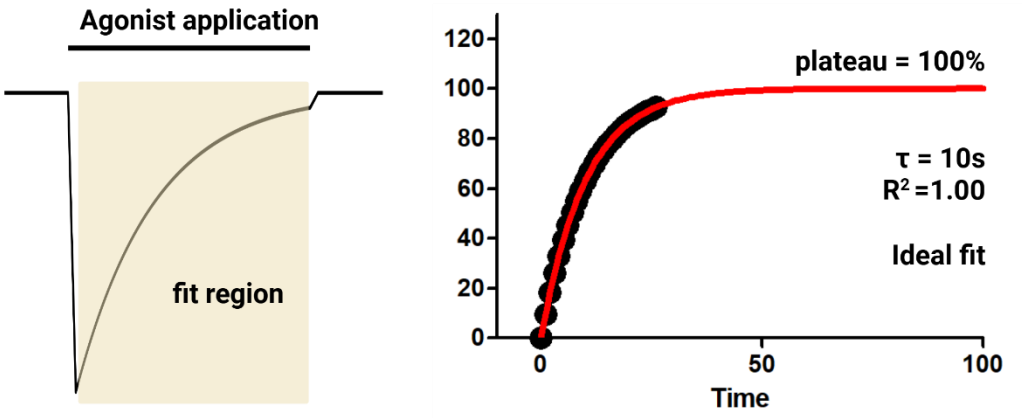
Agonist application
fit region
120
100
80
60
40
20
0
0
50
100
Time
plateau = 100%
τ = 10s
R2 =1.00
Ideal fit

2.5.2 Establishing reliable τ estimates

To estimate τ, I first evaluated desensitization curves across the full agonist concentration response. At low agonist concentrations (or slow rates of desensitization), the current decay within the 30 s application was insufficient to allow for unambiguous fitting using the exponential equation. At saturating concentrations, fits converged with well-defined parameters as shown in **Figure 2-1**.

The quality of each fit was assessed using the coefficient of determination (R^2), which measures how closely the fitted curve matches the data. An R^2 value greater than or equal to 0.99 is considered an excellent fit, values between 0.95 and 0.99 are indicative of a reasonable fit, and values below 0.95 indicate a poor fit. I considered the derived τ values from the fit to be reliable when two conditions were met: (1) the R^2 was ≥ 0.99, and (2) the fitted τ value fell within the agonist application time. The second condition was used because it ensured that the curve fits produce plateau values that fall between the peak current and the baseline, corresponding to a meaningful extent of desensitization at equilibrium. In contrast, when the τ value fell outside the agonist application time, plateau values typically occurred at values above the baseline, suggesting that the extent of desensitization at equilibrium is greater than 100%, which is not physically possible. Data points where the plateau was not physically meaningful were flagged as unreliable and thus excluded (**Figure 2-2**).

Figure 2-2 Representative exponential fits from recorded TEVC traces.

Whole-cell traces (left) and corresponding exponential fits to the decay region (right) for three constructs illustrating the three categories of fit behaviour. Shaded regions in the middle panels indicate the segment of the trace selected for fitting. **(a) Reliable fits with realistic plateau values.** P305A ELIC at 6 mM cysteamine (30-fold EC_{50}) shows a well-defined exponential decay within the 30 s recording window. The fit returns $R^2 = 0.998$, $\tau = 4.4$ s (within the recording window), and plateau = 85% (physically meaningful). All reliability criteria are met. **(b) Ambiguous fits.** The exponential model cannot reliably fit the decay of WT α1 GlyR at 0.5 mM glycine (2-fold EC_{50}) thus the fit parameters are classified as ambiguous. **(c) Unambiguous fit with unrealistic plateau values.** WT ELIC at 50 mM cysteamine (50-fold EC_{50}) shows minimal decay within the recording window. Although the fit returns a high R^2 (0.999), $\tau = 155$ s exceeds the recording window, and the fitted plateau (211%) is not physically meaningful. The fit extrapolates beyond what the data supports and is classified as unreliable. Red lines indicate the fitted curves.

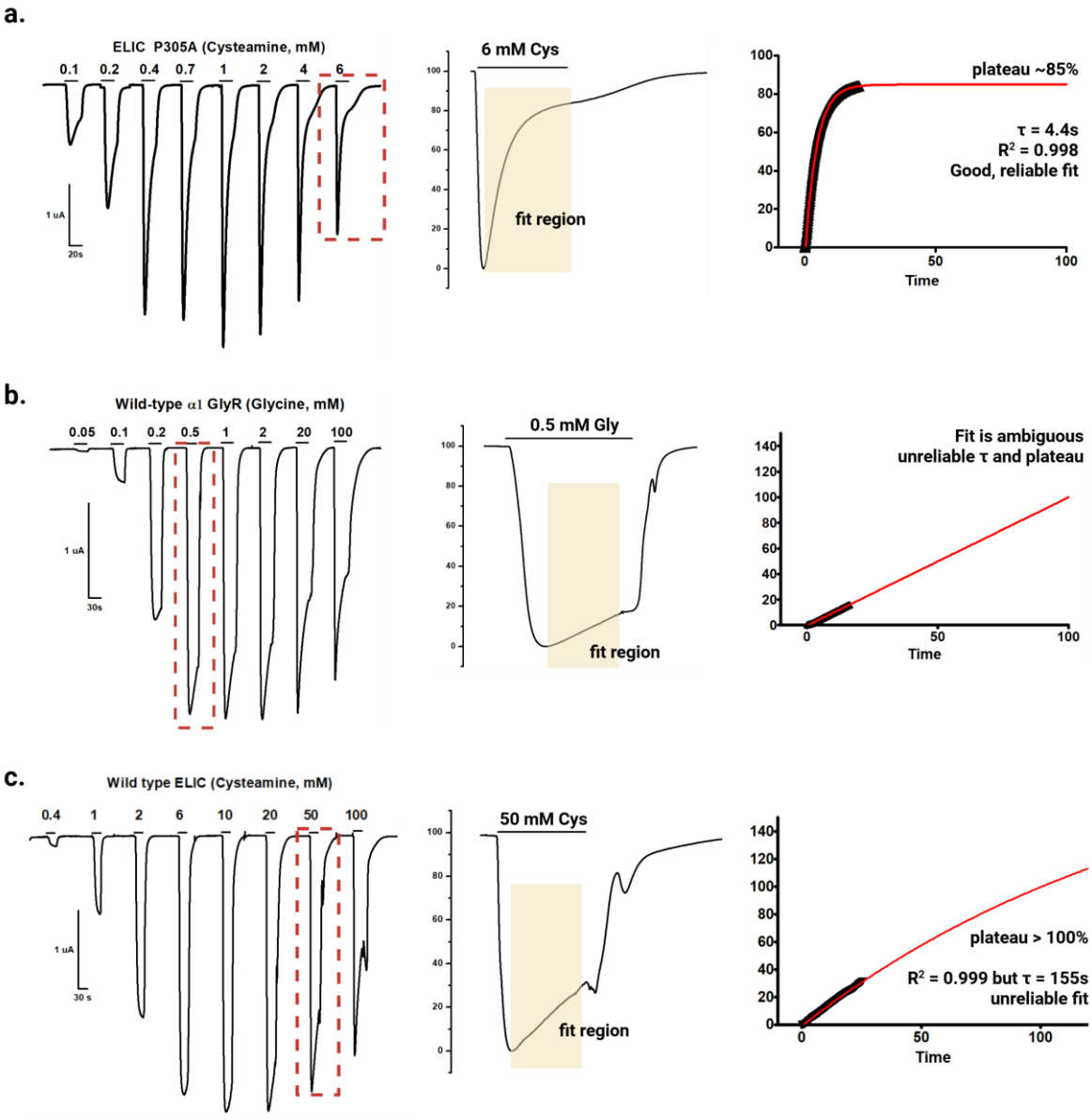
a.
ELIC P305A (Cysteamine, mM)
0.1 0.2 0.4 0.7 1 2 4 6
1 uA
20s
6 mM Cys
fit region
plateau ~85%
τ = 4.4s
R² = 0.998
Good, reliable fit
Time
b.
Wild-type α1 GlyR (Glycine, mM)
0.05 0.1 0.2 0.5 1 2 20 100
1 uA
30s
0.5 mM Gly
fit region
Fit is ambiguous
unreliable τ and plateau
Time
c.
Wild type ELIC (Cysteamine, mM)
0.4 1 2 6 10 20 50 100
1 uA
30 s
50 mM Cys
fit region
plateau > 100%
R² = 0.999 but τ = 155s
unreliable fit
Time

Note that I also assessed the influence of curve selection on fitted τ values. Although the entire decay would normally be used for fitting, manual selection of the decay region introduces potential variability across recordings, so I wanted to test whether this affects τ. Three selection ranges were tested: minimum to plateau, slightly above minimum to plateau, and minimum to just before the plateau (**Figure *2-3***). For the α1 GlyR at 100-fold EC_{50}, variation in τ across these selection ranges was approximately 1 s, comparable to the variability observed between different oocytes at the same agonist concentration. The same comparison was repeated for P305A ELIC at 30-fold EC_{50}, which desensitizes roughly an order of magnitude faster than the α1 GlyR, and yielded similarly small variation in τ across the three selection ranges. This comparison supports the observation that curve selection does not meaningfully affect the resulting τ when the underlying fit is reliable, regardless of the desensitization rate of the construct. To ensure consistent quantification of τ, the decay region from the minimum point to the plateau was used for all measurements in this thesis.

2.5.3 Concentration-dependence of desensitization rate (the 1/τ plot)

To assess the concentration-dependence of macroscopic desensitization, the reciprocal of the fitted τ (1/τ) was plotted against agonist concentration expressed as log [Agonist] for each construct. For a process characterized by a single exponential component, this relationship should be linear. I use this slope because it summarizes how strongly agonist concentration drives the channel into the desensitized state (Franke et al., 1993; Hénault et al., 2019). A steeper slope indicates that the macroscopic desensitization rate increases more sharply with agonist concentration. This slope is used throughout this thesis to compare macroscopic desensitization between constructs and across receptors.

Figure 2-3 Desensitization curve selection and fits

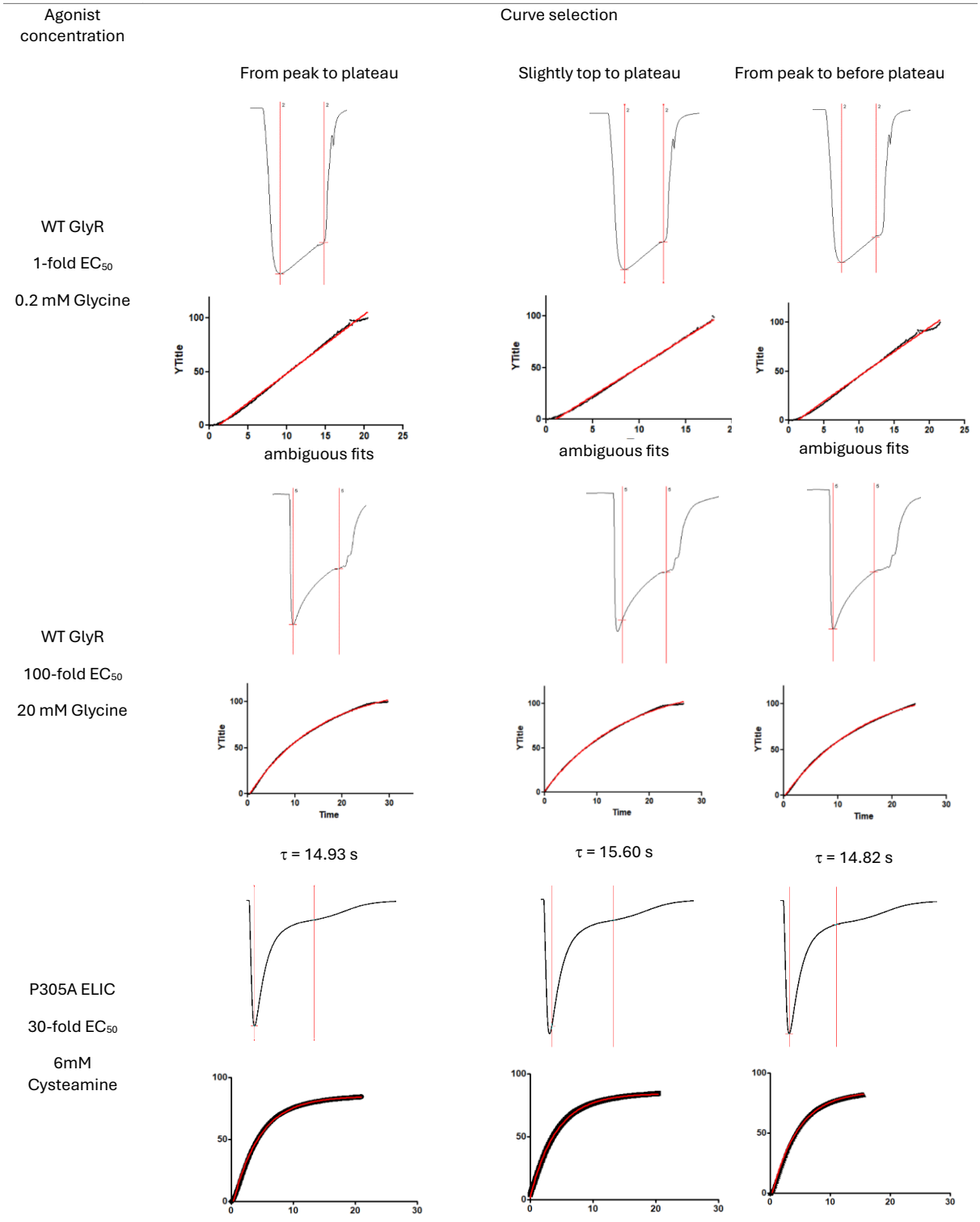

Although a single exponential is used here, macroscopic desensitization in pLGICs can in some cases be better described by two components, fast and slow (Auerbach & Akk, 1998; Cachelin & Colquhoun, 1989). TEVC recordings, however, are limited by buffer exchange and have a kinetic resolution on the seconds scale, which makes it difficult to resolve fast components from a two-component fit. For the constructs studied in this thesis, single-exponential fits gave $R^2 \geq 0.99$ across the agonist concentrations where τ was reliable (see above), supporting its use as the simplest description of the decay under these recording conditions.

In some cases, where no measurable desensitization was observed or where the fit was ambiguous, the $1/\tau$ values are shown as hollow symbols on the $1/\tau$ plots and were not included in the linear fit to derive the slope. For these very slow-desensitizing constructs, τ is large and $1/\tau$ approaches zero, so these points are plotted at $1/\tau = 0$ to indicate the absence of measurable desensitization on the timescale of the recording.

To demonstrate how the criteria above were applied in practice, I used the P305A mutant of ELIC as an example. P305A was chosen because it desensitizes fast enough at every agonist concentration across the utilized agonist concentration range to produce a substantial decay of the current. For P305A, fits of the current decay cysteamine concentration between 0.4 and 6 mM (2 to 30-fold EC_{50}) met all three reliability criteria, with $R^2 \geq 0.997$, τ values between 4.3 and 7.7 s (well within the 30s recording window), and physically meaningful plateau values converging to roughly 85%. At the lower cysteamine concentrations of 0.1 and 0.2 mM (0.5 and 1-fold EC_{50}), the plateau values exceeded 100% even though the fits were deemed unambiguous. The obtained τ values were thus flagged as unreliable. As a result, the resulting $1/\tau$ versus agonist concentration plots showed a linear relationship across the reliable concentrations (**Figure *2-4***).

Figure 2-4 Example of the desensitization analysis for P305A ELIC.

(a) TEVC trace from a single oocyte across cysteamine concentrations (0.1 to 6 mM) shown at scale. (b) Exponential fits to the decay region of each trace, normalized such that 0% corresponds to the peak current and 100% corresponds to the baseline. The fits at 0.1 and 0.2 mM cysteamine extrapolate to plateau values exceeding 100%, indicating that the fit is extrapolating beyond what the data supports. The dashed line marks the 100% threshold. (c) $1/\tau$ versus log [cysteamine] plot. Filled symbols represent data points meeting all reliability criteria ($R^2 \geq 0.99$, τ within the recording window, and physically meaningful plateau). Hollow symbols at 0.1 and 0.2 mM represent data points excluded due to non-meaningful plateau values. The solid red line represents a linear fit to the reliable data points, with the $1/\tau$ slope value shown.

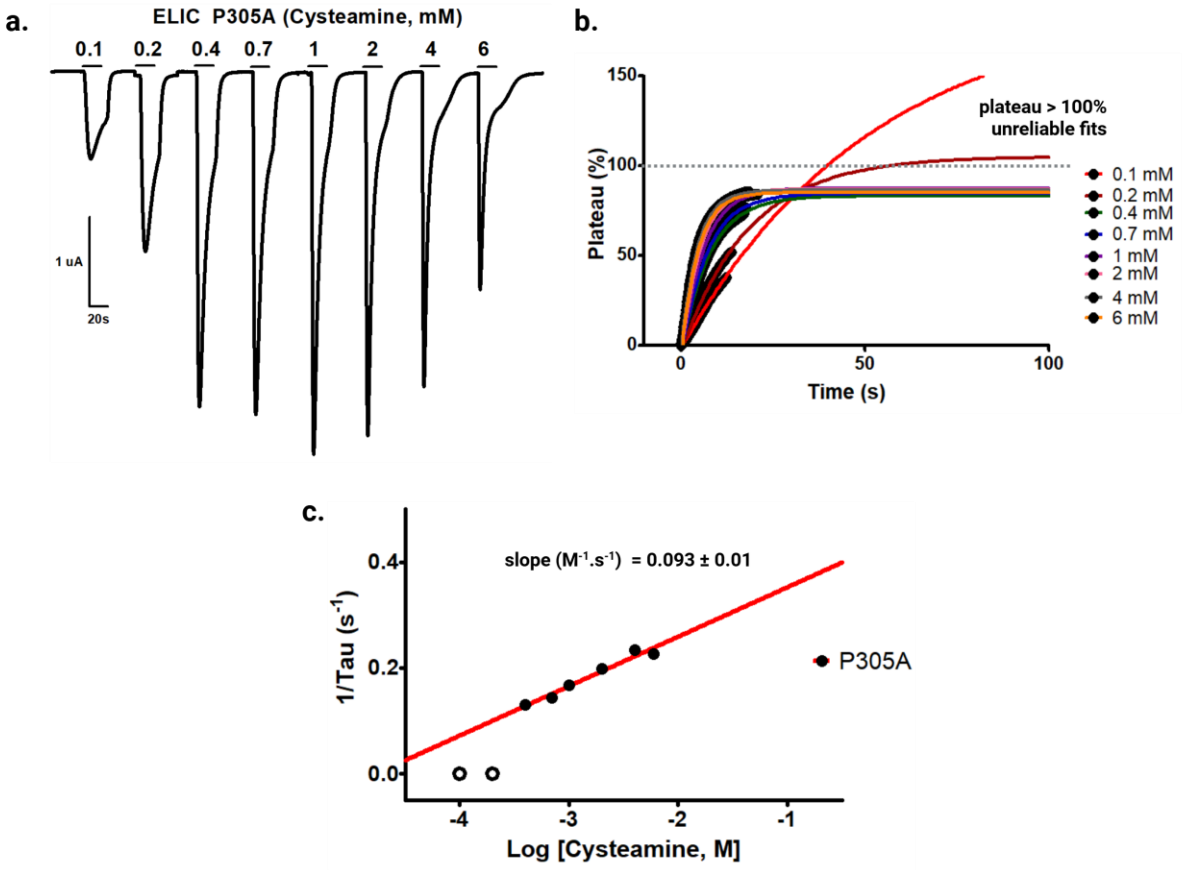
a.
ELIC P305A (Cysteamine, mM)
0.1
0.2
0.4
0.7
1
2
4
6
1 uA
20s
b.
plateau > 100%
unreliable fits
Plateau (%)
150
100
50
0
0
50
100
Time (s)
0.1 mM
0.2 mM
0.4 mM
0.7 mM
1 mM
2 mM
4 mM
6 mM
c.
slope (M-1.s-1) = 0.093 ± 0.01
1/Tau (s-1)
0.4
0.2
0.0
-4
-3
-2
-1
Log [Cysteamine, M]
P305A

2.5.4 Calculation of the extent of desensitization (% Des)

For the analysis of ELIC Ala mutants in Chapter 4, the extent of desensitization (%Des) is reported alongside the τ for each mutant. Desensitizing currents were induced by 1-minute applications of agonist at 10-fold EC_{50}. And the %Des was calculated directly from the TEVC traces as

$$\textbf{Eq. 2} \quad \%\boldsymbol{Des} = \mathbf{1} - \frac{\boldsymbol{I_{residual}}}{\boldsymbol{I_{peak}}}$$

where I_{peak} is the agonist-induced peak current and $I_{residual}$ the steady-state residual current remaining at the end of the agonist application. The 10-fold EC_{50} concentration was chosen because it falls within the reliable range for most ELIC mutants tested while remaining below the conditions that compromise oocyte integrity.

2.5.5 Desensitization analysis concluding remarks

In conclusion, the two analyses described here provided a framework for comparing macroscopic desensitization across receptors and mutants in this thesis. In Chapter 3, the 1/τ slope is used to compare W-R-P motif and pocket mutants across ELIC, GlyR, and GLIC. This analysis was chosen because the slope summarizes the concentration dependence of 1/τ as a single value per mutant, which allows for comparisons across receptors with very different agonist potencies and across mutants where reliable τ values cannot be determined at all concentrations.

In Chapter 4, τ and %Des values at 10-fold EC_{50} are used to compare ELIC mutants. This analysis was chosen because the conditions are the same across all mutants and allows direct measurement of τ and %Des without relying on a curve fit across multiple concentrations.

3 Chapter 3 – A conserved lipid-binding pocket has divergent roles across pLGICs

3.1 Background and rationale:

As described in the Introduction, the W-R-P motif observed in the inner leaflet lipid binding site of ELIC is conserved in the prokaryote, GLIC, and across the anion-selective pLGIC families, raising the possibility that lipid binding to this site in other pLGICs influences desensitization by the same mechanism proposed for ELIC. To test this possibility, I initially chose to focus on the human ρ1 $GABA_AR$ and the *zebrafish* α1 GlyR (hereafter referred to as the $GABA_AR$ and GlyR, respectively) for three main reasons. First, both the $GABA_AR$ and the GlyR are representatives of the two major anion-selective pLGIC families. Second, published studies suggest that both exhibit desensitization rates that are qualitatively similar to the rates of desensitization of ELIC and are thus accessible to characterization using TEVC electrophysiology (Gielen et al., 2015a). Finally, both the pLGICs exist as homo-pentamers, like ELIC. Note that I also included the prokaryote, GLIC, in my study because it is a close structural homolog of ELIC yet exhibits a more extensive network of aromatic interactions at its M4-M1/M3 interface (Hénault et al., 2015; Therien & Baenziger, 2017). Both the $GABA_AR$ and the GlyR also exhibit extensive networks of aromatic interactions at their M4-M1/M3 interfaces, and these networks play an important role driving M4 interactions with M1/M3 during folding and maturation (Cory-Wright et al., 2018; Haeger et al., 2009). I was conscious that these aromatic networks could influence M4 conformation and/or reduce M4 dynamics to limit the effects of lipid binding to their W-R-P pocket. GLIC, which also exhibits a similar aromatic network, thus provides an additional test as to whether the conserved W-R-P motif implies a functional conservation.

As mentioned, the key phenotypic observations that led to the suggestion that M4 dynamics influence desensitization in ELIC are (1) Ala mutations to W-R-P residues that frame the lipid binding site, particularly P305A, have modest effects on the EC_{50}, but lead to a dramatic increase in channel desensitization rates; (2) Ala mutations to residues in the W-R-P pocket, which could alter lipid binding, also increase desensitization rates; (3) Repositioning the M4 kink either up or down by one helical turn on the P305A background increases desensitization rates, possibly by affecting how the conformation of M4 and thus how it interacts with M1 and M3, and (4) the Δ8 C-terminal deletion of M4 leads to both increased rates of desensitization and enhanced M4 dynamics, the latter suggested by a crystal structure of the Δ8 ELIC mutant. As a step towards addressing whether lipid binding to the W-R-P pocket in other pLGICs influences desensitization via a similar mechanism to that proposed in ELIC, I set out to assess whether these same mutations lead to similar effects on desensitization in the GlyR, the $GABA_AR$, and GLIC.

3.2 Results

3.2.1 Desensitization onset differs between ELIC, GlyR, and GLIC

I first characterized the agonist-induced responses of wild type (WT) ELIC, the $GABA_AR$, the GlyR and GLIC expressed individually in *Xenopus laevis* oocytes. All but the $GABA_AR$ expressed robustly allowing characterization of both their agonist (cysteamine, glycine, and protons, respectively) concentration response and their rates of desensitization. WT ELIC and GlyR yielded EC_{50} values of 0.96 ± 0.23 mM and 0.23 ± 0.05 mM, respectively. For GLIC, the pH_{50} was 4.82 ± 0.16 (corresponding to a proton concentration of 9.33 ± 1.70 μM) (**Figure 3-1,Table 3-1**). These values are consistent with published values (Hénault et al., 2015; P. Kumar et al., 2020). Despite exploring an extensive range of conditions (amount of RNA injected, expression days), I was unable to express the $GABA_AR$ at sufficient levels to accurately assess either its concentration response to agonist application or its rates of desensitization. Studies with the $GABA_AR$ were thus not pursued further.

I next compared desensitization across the agonist concentration response of each receptor (**Figure 3-2**). Qualitatively, the three receptors differ in both the agonist concentration at which desensitization becomes apparent, and the extent to which the current decays during agonist application. In ELIC, current decay is not clearly detectable at low agonist concentrations but became progressively evident as the cysteamine concentration increases, with measurable desensitization clearly apparent at approximately 10-fold EC_{50}. In GlyR, desensitization is evident at concentrations as low as the EC_{50} for glycine, and both the rate and extent of desensitization increases with agonist concentration. In contrast, GLIC showed no detectable current decay until exposed to H^+ concentrations roughly 100-fold EC_{50} consistent with previous studies reporting that GLIC displays intrinsically slow desensitization kinetics that are difficult to quantify using TEVC (Basak et al., 2017; Gielen & Corringer, 2018a;

Velisetty & Chakrapani, 2012). At these high concentrations of protons, the rates of GLIC desensitization increase rapidly with increasing proton concentrations.

To quantify these observations, I applied the desensitization analysis approach described in Chapter 2. The current decay at each agonist concentration was fit to a one-phase exponential to obtain the time constant (τ), and $1/\tau$ was plotted against the log of agonist concentration to estimate the slope describing the concentration dependence of macroscopic desensitization (Franke et al., 1993; Hénault et al., 2019). For ELIC, only the decay curve at 100 mM cysteamine led to both a reliable fit and a realistic τ value. I attempted to record agonist responses at concentrations above 100 mM cysteamine to establish additional τ values, but higher concentrations of cysteamine led to problems with oocyte membrane integrity thus preventing further analysis. For GlyR, only the fits at 20 and 100 mM glycine met the reliability criteria (Chapter 2), which was insufficient to define a linear $1/\tau$ versus agonist concentration relationship. For GLIC, no observable decay was observed at pH values until pH 3.0. At pH values between 3.0 and 2.0, however, the high H^+ concentrations led to a rapid onset of apparent desensitization, as exemplified by both the rapid decay of each whole cell current and the reduction in the whole cell response observed in subsequent proton applications. An alternative interpretation of these effects, however, is that the extreme protons concentrations lead to inactivation due to pH-induced denaturation of GLIC. It is thus difficult to determine whether the observed decay solely reflects desensitization. Consequently, reliable $1/\tau$ slopes could not be calculated for any of the three WT receptors, and their slopes are all reported as $<0.01\ M^{-1}\ s^{-1}$ (**Figure 3-2,Table 3-1**).

Note that at high agonist concentrations, both ELIC and GLIC exhibit rebound currents, which are transient outward or inward currents observed shortly after agonist washout. These rebound currents have been attributed to channel block by the agonist itself, where the agonist binds within the open pore and prevents ion flow, and upon washout, the channel is relieved of

Figure 3-1 WT ELIC, GlyR, and GLIC are functional in *Xenopus laevis* oocytes

(**a-c**) (left) Representative whole-cell TEVC recordings from oocytes expressing: **a.** WT ELIC, **b.** WT GlyR, and **c.** WT GLIC, in response to increasing agonist concentrations. Scale bars are shown on each trace. Horizontal bars above each trace represent the time the indicated concentration of agonist was exposed to the oocyte. (right) Dose-response curves (normalized current (I/I_{max}) versus ligand concentration) for **a.** ELIC, **b.** GlyR, and **c.** GLIC. Data were fit with a variable-slope sigmoidal function. Error bars represent the standard deviation (S.D.) from at least 3 independent measurements ($n \geq 3$).

a.

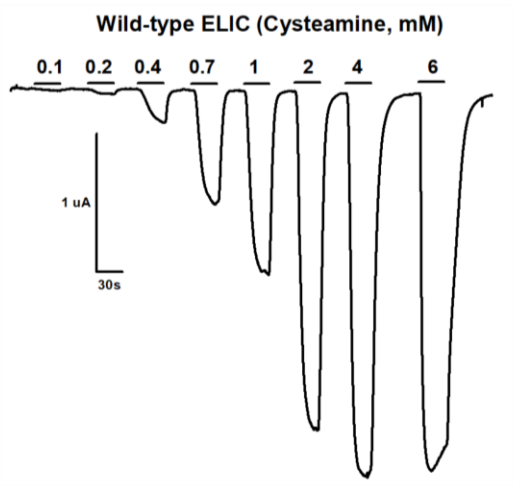
Wild-type ELIC (Cysteamine, mM)
0.1 0.2 0.4 0.7 1 2 4 6
1 uA
30s

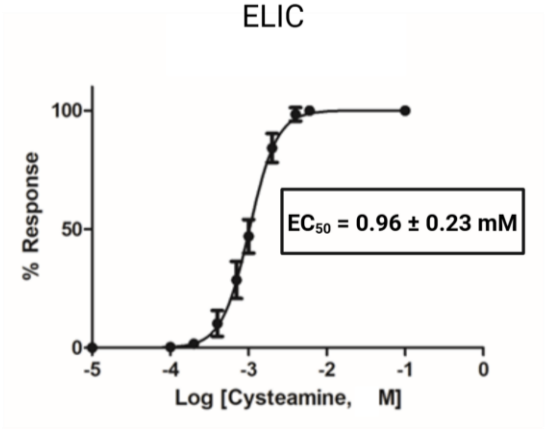
ELIC
% Response
100
50
0
-5 -4 -3 -2 -1 0
Log [Cysteamine, M]
EC50 = 0.96 ± 0.23 mM

b.

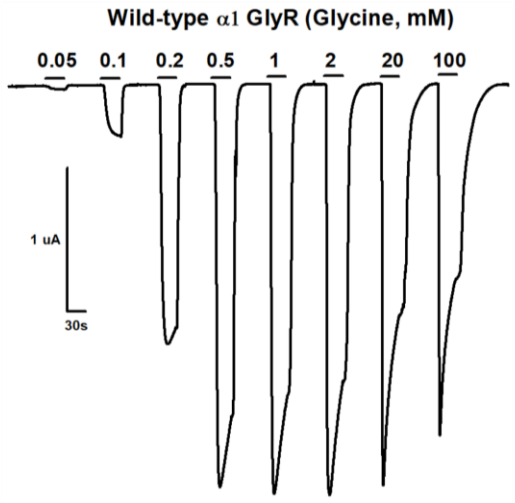
Wild-type α1 GlyR (Glycine, mM)
0.05 0.1 0.2 0.5 1 2 20 100
1 uA
30s

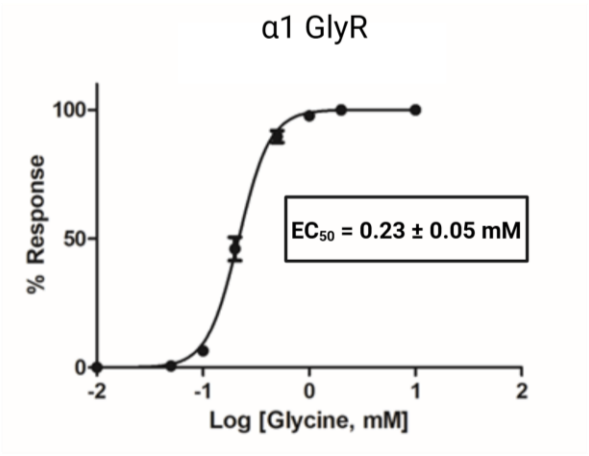
α1 GlyR
% Response
100
50
0
-2 -1 0 1 2
Log [Glycine, mM]
EC50 = 0.23 ± 0.05 mM

c.

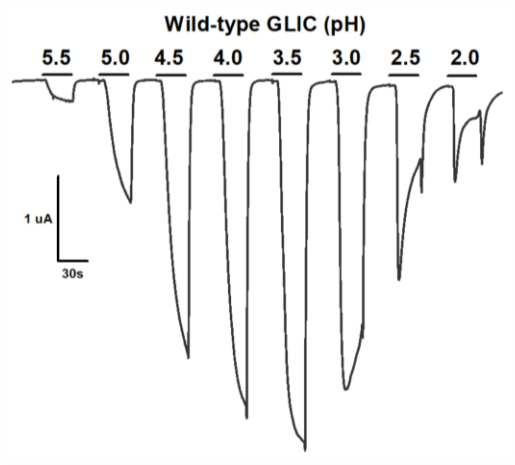
Wild-type GLIC (pH)
5.5 5.0 4.5 4.0 3.5 3.0 2.5 2.0
1 uA
30s

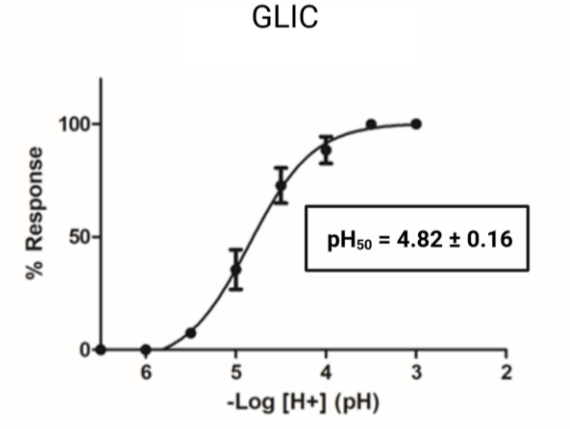
GLIC
% Response
100
50
0
6 5 4 3 2
-Log [H+] (pH)
pH50 = 4.82 ± 0.16

Figure 3-2 Desensitization onset and concentration dependence differ across WT ELIC, GlyR, and GLIC.

a, c, e. Representative whole-cell TEVC recordings from oocytes expressing **a.** WT ELIC, **c.** WT GlyR, and **e.** WT GLIC, at increasing agonist concentrations. Scale bars are shown on each trace. Horizontal bars above each trace represent the time the indicated concentration of agonist was exposed to the oocyte. **b, d, f.** Plots of $1/\tau$ versus agonist concentration for **b.** ELIC, **d.** GlyR, and **f.** GLIC. Filled symbols represent data points where the exponential fit met reliability criteria. Hollow symbols represent data points that did not meet one or more criteria. Dashed red lines connect adjacent reliable data points as a visual aid and do not represent linear fits. Error bars represent S.D. from at least 3 independent measurements ($n \geq 3$).

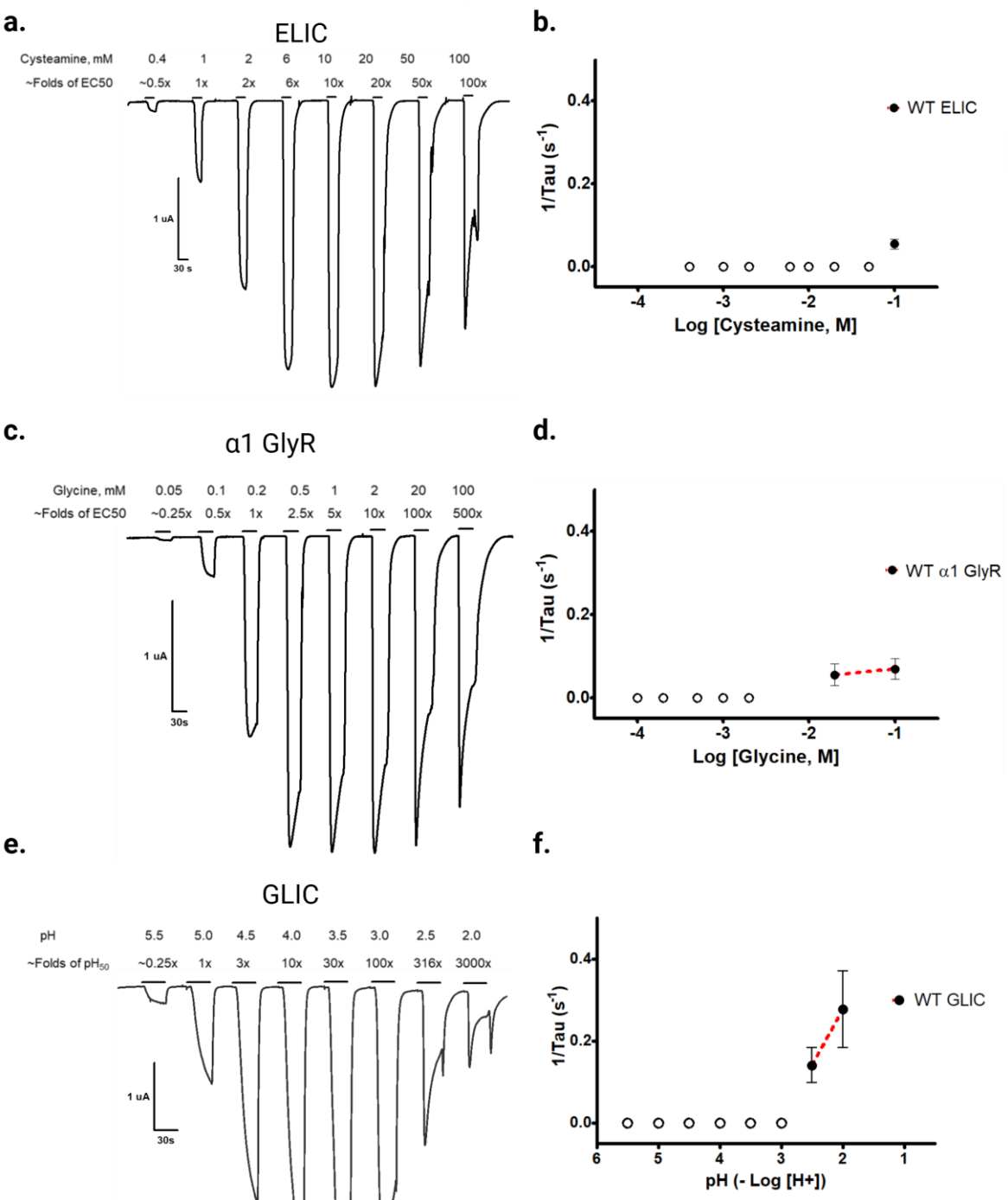
a.
ELIC
Cysteamine, mM 0.4 1 2 6 10 20 50 100
~Folds of EC50 ~0.5x 1x 2x 6x 10x 20x 50x 100x
1 uA
30 s
b.
WT ELIC
1/Tau (s-1)
0.4
0.2
0.0
-4 -3 -2 -1
Log [Cysteamine, M]
c.
α1 GlyR
Glycine, mM 0.05 0.1 0.2 0.5 1 2 20 100
~Folds of EC50 ~0.25x 0.5x 1x 2.5x 5x 10x 100x 500x
1 uA
30s
d.
WT α1 GlyR
1/Tau (s-1)
0.4
0.2
0.0
-4 -3 -2 -1
Log [Glycine, M]
e.
GLIC
pH 5.5 5.0 4.5 4.0 3.5 3.0 2.5 2.0
~Folds of pH50 ~0.25x 1x 3x 10x 30x 100x 316x 3000x
1 uA
30s
f.
WT GLIC
1/Tau (s-1)
0.4
0.2
0.0
6 5 4 3 2 1
pH (- Log [H+])

block and transiently re-open before inactivating (Marabelli et al., 2015). The presence of rebound currents at high agonist concentrations in ELIC and GLIC therefore suggests that channel block contributes to the apparent decay of the whole-cell current under these conditions, complicating the interpretation of desensitization rates from raw decay traces. Such rebound currents were not observed with GlyR.

3.2.2 Effects of W-R-P motif mutations on desensitization in ELIC, GlyR, and GLIC

To test whether the W-R-P motif is functionally conserved across the three pLGICs, I introduced Ala substitutions at each of the three motif residues in ELIC, GlyR, and GLIC, and compared their effects on both agonist sensitivity and desensitization.

In ELIC, each of the three Ala mutations expressed robustly in *Xenopus laevis* oocytes with minimal effects on EC_{50} values relative to WT (**Figure 3-3,Table 3-1**). The W224A mutant gave a WT-like EC_{50} while R301A and P305A led to roughly 2- and 4- fold gains in function, respectively. P305A also showed reduced cooperativity (Hill slope of 1.39 ± 0.44 versus 2.26 ± 0.79 for WT), although its rapid desensitization may limit the accuracy of the dose-response curves as desensitization may occur before full activation. In GlyR, only the R415A mutant yielded measurable glycine-induced currents, indicating that W267 and P419 are essential for folding and/or function. In GLIC, W217A and R296A expressed robustly and led to roughly 4- and 2-fold losses of function, respectively, while P300A did not result in a measurable proton-induced current, consistent with previous studies (Hénault et al., 2015; Therien & Baenziger, 2017). Although the conclusions are limited by the lack of expression of three of the nine mutants, for those that did express, the lack of substantive changes to the measured EC_{50} values suggests that the W-R-P motif does not play a critical role in agonist-induced activation.

In terms of desensitization (**Figure 3-3, Figure 3-4**), each of the three Ala substitutions in ELIC led to an increase in the rate of macroscopic desensitization. Whole-cell currents across the full agonist concentration response are shown in **Figure 3-3**, with peak-scaled traces at 10-fold EC_{50} (relative to WT) superimposed with WT ELIC in **Figure 3-4**. Decay was detectable across a broad range of agonist concentrations, but reliable τ values could only be estimated at higher concentrations where the decay was sufficient to constrain the fit. Qualitatively, the extent of decay varied across the three mutants as exemplified by the superimposed traces recorded at 10-fold EC_{50}. At these concentrations, all three mutants reach a steady-state plateau within the 1-minute application (**Figure 3-4**), but the magnitude of decay differs. P305A shows near-complete decay at 10-fold EC_{50}, with a rate qualitatively comparable to the intrinsically fast-desensitizing α7 nAChR (McCormack et al., 2010; Mike et al., 2000; Williams et al., 2011), whereas W224A and R301A showed partial decay.

I then compared 1/τ slopes across the ELIC W-R-P motif mutants. In WT ELIC, the 1/τ slope could not be reliably derived because desensitization was too slow to fit at most tested cysteamine concentrations (**Table 3-1)**. The 1/τ slopes ranged from 0.029 ± 0.011 $M^{-1}s^{-1}$ for R301A to 0.137 ± 0.052 $M^{-1}s^{-1}$ for P305A, with W224A intermediate at 0.073 ± 0.008 $M^{-1}s^{-1}$ (**Figure 3-4, Table 3-1**). These results are consistent with previous observations that disrupting the W-R-P motif in ELIC accelerates desensitization (Hénault et al., 2019).

In GlyR, R415A was the only W-R-P motif mutant that yielded measurable glycine-evoked currents (**Figure 3-3, Figure 3-4**). Whole-cell currents across the full agonist concentration response are shown in **Figure 3-3**, with peak-scaled traces at 10-fold EC_{50} (relative to WT) superimposed with WT GlyR in **Figure 3-4**. R415A produced a measurable 1/τ slope (0.053 ± 0.007 $M^{-1}s^{-1}$), in contrast to WT GlyR where reliable rates could not be quantified. As W267A and P419A did not produce measurable agonist-evoked currents , the comparison of mutations to the W-R-P motif between the GlyR and ELIC is limited to a single

residue. To further explore how a loss of the Trp residue itself accelerates desensitization in GlyR, I generated a series of substitutions, including W267F, W267Y, and W267L, to find a mutant that retained function but lacked the native Trp. Only the aromatic substitutions W267F and W267Y resulted in agonist-induced currents, and both showed desensitization rates similar to WT. This suggests that the aromatic character at this position is essential for channel function, consistent with previous work showing that the aromatic network at the GlyR M4-M1/M3 interface is required for folding and surface expression (Haeger et al., 2009). The lack of function for non-aromatic substitutions at this position thus prevents a direct test of how removing the Trp side chain affects desensitization in GlyR.

In GLIC, neither W217A nor R296A had a measurable effect on desensitization rates at H^+ concentrations exceeding 10-fold EC_{50}. As in GlyR, P300A did not yield measurable currents, indicating that the Pro residue is also essential for folding and/or function in GLIC. These results suggest that the W-R-P motif in GLIC does not modulate desensitization.

Ala substitutions in the W-R-P motif led to different conclusions for each of the three pLGICs regarding the role of M4 conformation/dynamics in desensitization (**Figure 3-3, Figure 3-4**). As discussed in more detail below and in Chapter 4, Ala mutations to each of these three residues should alter the conformation and/or dynamics of the M4 α-helix in each pLGIC. In ELIC, altered M4 conformation and/or dynamics accelerates desensitization, with the magnitudes of the observed changes in the $1/\tau$ slopes differing between the three mutants. In GlyR, R415A also accelerates desensitization with a phenotype qualitatively similar to that of ELIC R301A at 10-fold EC_{50}, although their slopes differ by approximately 2-fold (0.053 vs 0.029 $M^{-1}s^{-1}$ for R415A and R301A, respectively; **Figure 3-4, Table 3-1**. On the surface, this observation is consistent with the hypothesis that M4 conformation and/or dynamics in the GlyR also impacts desensitization rates. It is possible, however, that the mutation instead influences desensitization via an M4 independent mechanisms (see below). The lack of

expression of W267A and P419A limits the comparison between ELIC and the GlyR to a single residue mutation.

In contrast, neither the W217A nor the R296A mutation had a measurable effect on desensitization in GLIC. One possible interpretation of these two results is that the change in M4 conformation and/or dynamics in GLIC that result from the two mutations simply do not influence desensitization, as they do in ELIC. This would imply that desensitization in GLIC is not affected by M4 conformation and/or dynamics. Alternatively, additional aromatic interactions at the M4-M1/M3 interface in GLIC may strengthen M4-M1/3 interactions to minimize the structural consequences of both the W217A and R296A mutants, so that the mutations do not lead to the changes in M4 conformation and/or dynamics that are required to alter desensitization rates. Regardless, both interpretations suggest that the link between M4 conformation and/or dynamics and the rates of desensitization in GLIC differ between that in ELIC, although this conclusion is limited by the fact that the comparison involves only two residues.

Figure 3-3 Ala mutations to the W-R-P motif accelerate desensitization in ELIC and GlyR but not in GLIC

a. ELIC (left) Representative whole-cell TEVC recordings from oocytes expressing WT ELIC, W224A, R301A, and P305A in response to increasing cysteamine concentrations. Scale bars are shown on each trace. Horizontal bars above each trace represent the time the indicated concentration of agonist was exposed to the oocyte. (right) Plot of $1/\tau$ versus Log [Cysteamine, M] for WT, W224A, R301A, and P305A. **b. GlyR** (left) Representative TEVC recordings from oocytes expressing WT GlyR and R415A in response to increasing glycine concentrations. Horizontal bars above each trace represent the time the indicated concentration of agonist was exposed to the oocyte (right) Plot of $1/\tau$ versus Log [Glycine, M] for WT and R415A. **c. GLIC.** Representative TEVC recordings from oocytes expressing wildtype GLIC, R296A, and W217A in response to decreasing pH. Horizontal bars above each trace represent the time the indicated concentration of agonist was exposed to the oocyte. No measurable current decay was detected in GLIC W-R-P motif Ala mutants; a $1/\tau$ plot is therefore not shown. Horizontal bars above each trace represent the time the indicated concentration of agonist was exposed to the oocyte. Filled symbols represent data points where the exponential fit met reliability criteria; data points that did not meet reliability criteria are not shown. Solid lines represent linear fits to reliable data points. Error bars represent S.D. from at least 3 independent measurements ($n \geq 3$).

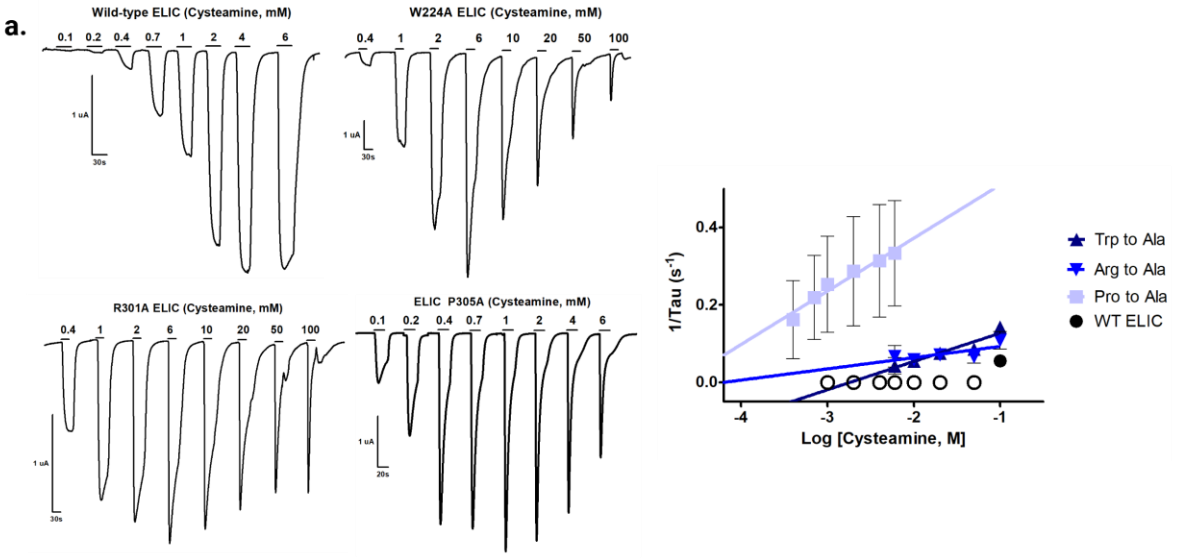
a.
Wild-type ELIC (Cysteamine, mM)
0.1 0.2 0.4 0.7 1 2 4 6
W224A ELIC (Cysteamine, mM)
0.4 1 2 6 10 20 50 100
R301A ELIC (Cysteamine, mM)
0.4 1 2 6 10 20 50 100
ELIC P305A (Cysteamine, mM)
0.1 0.2 0.4 0.7 1 2 4 6
1 uA
30s
20s
1/Tau (s-1)
Log [Cysteamine, M]
Trp to Ala
Arg to Ala
Pro to Ala
WT ELIC

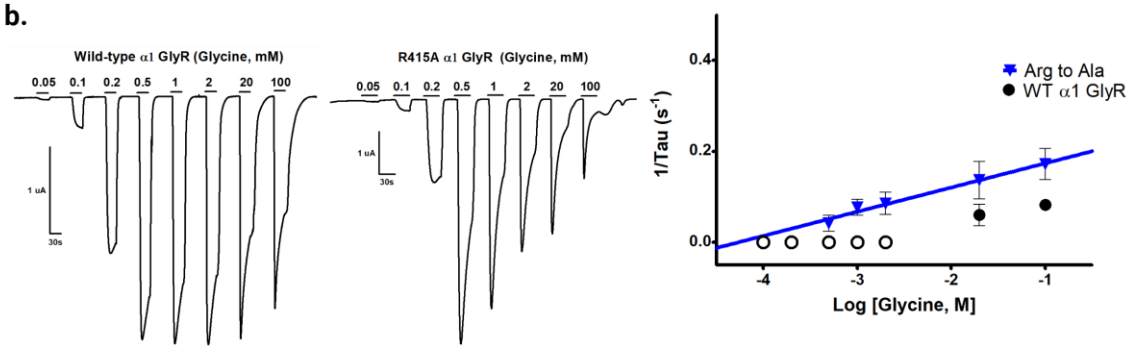
b.
Wild-type α1 GlyR (Glycine, mM)
0.05 0.1 0.2 0.5 1 2 20 100
R415A α1 GlyR (Glycine, mM)
0.05 0.1 0.2 0.5 1 2 20 100
1 uA
30s
1/Tau (s-1)
Log [Glycine, M]
Arg to Ala
WT α1 GlyR

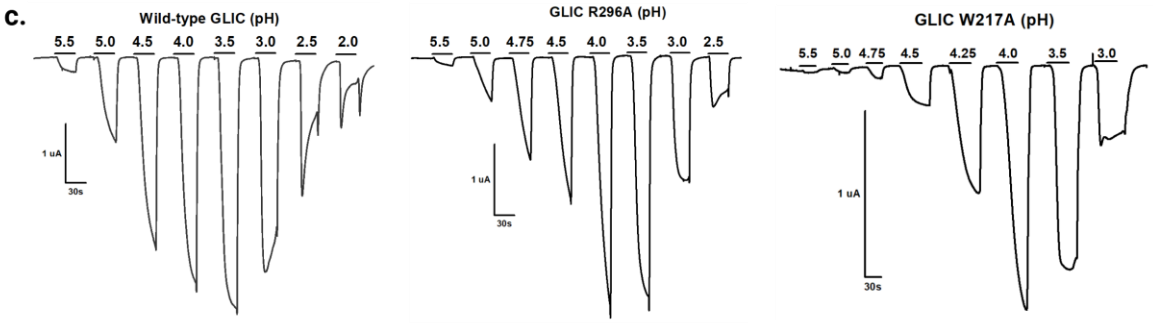
c.
Wild-type GLIC (pH)
5.5 5.0 4.5 4.0 3.5 3.0 2.5 2.0
GLIC R296A (pH)
5.5 5.0 4.75 4.5 4.0 3.5 3.0 2.5
GLIC W217A (pH)
5.5 5.0 4.75 4.5 4.25 4.0 3.5 3.0
1 uA
30s

Figure 3-4 Ala mutations to the W-R-P motif produce distinct effects on desensitization in ELIC, GlyR, and GLIC.

a. Structural view of the ELIC TMD showing the W-R-P motif residues (Trp224, Arg301, Pro305) at the inner-leaflet lipid binding site. A bound PE molecule (yellow, carbon) is shown with its acyl chains wedged into the pocket between M1 (wheat), M3 (pink), and M4 (light blue). **b-d**. Effects of W-R-P motif Ala mutations in **b.** ELIC, **c.** GlyR, and **d.** GLIC. (left) Dose-response curves (normalized current (I/I_{max}) versus ligand concentration) overlaying WT (black) and the W→A (dark blue), R→A (bright blue), and P→A (light blue) Ala mutants. Data were fit with a variable-slope sigmoidal function. (right) Peak-scaled membrane currents elicited by 1-minute application of agonist at ~10-fold EC_{50} of the WT receptor: 10 mM cysteamine for ELIC, 2 mM glycine for GlyR, and pH 4.0 for GLIC. Error bars represent S.D. from at least 3 independent measurements ($n \geq 3$).

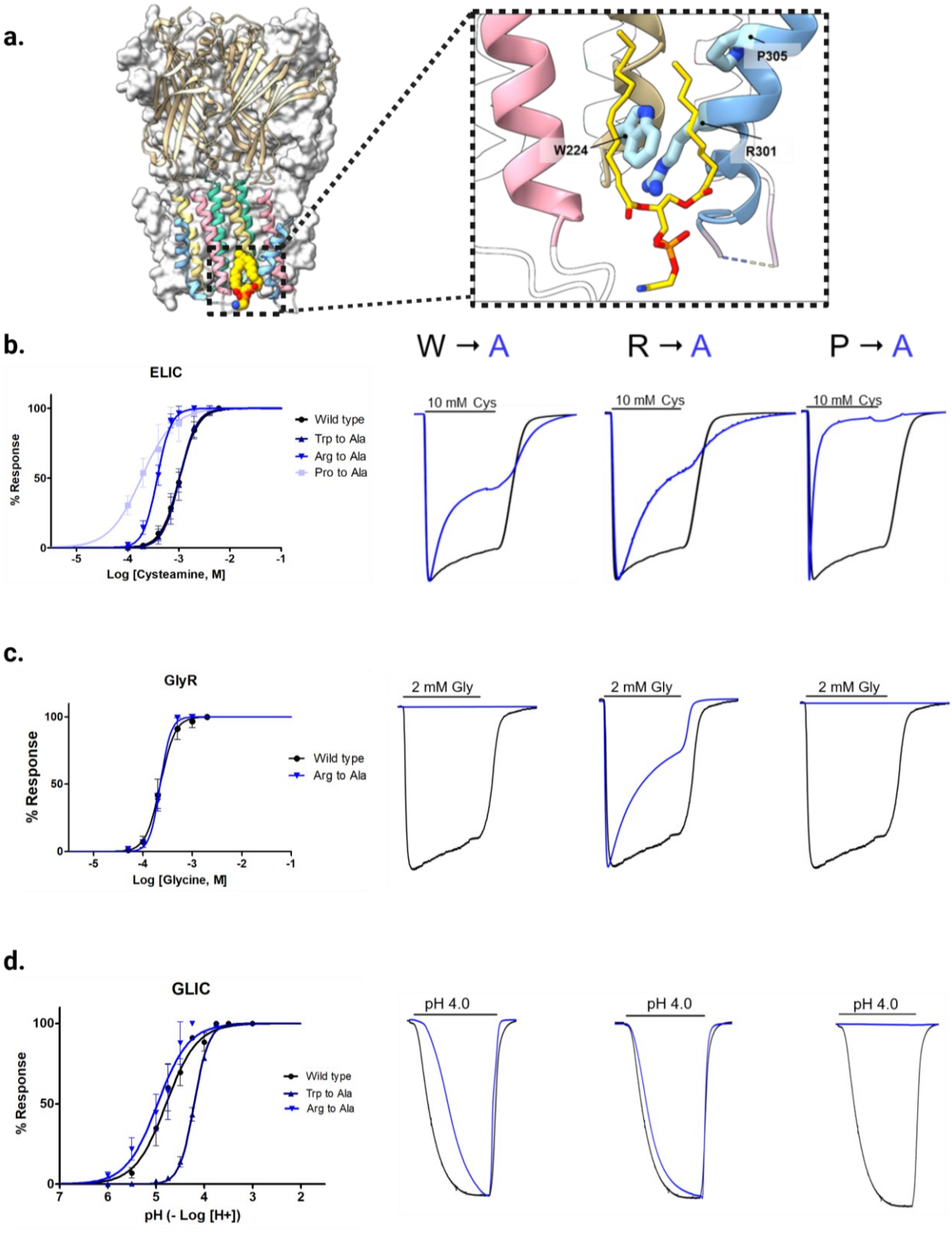
a.
P305
W224
R301
b.
W → A
R → A
P → A
ELIC
% Response
Log [Cysteamine, M]
Wild type
Trp to Ala
Arg to Ala
Pro to Ala
10 mM Cys
c.
GlyR
% Response
Log [Glycine, M]
Wild type
Arg to Ala
2 mM Gly
d.
GLIC
% Response
pH (- Log [H+])
Wild type
Trp to Ala
Arg to Ala
pH 4.0

Table 3-1 Effect of mutations to the W-R-P motif in ELIC, GlyR, and GLIC

pLGIC	Mutant	EC_{50} (Agonist) / pH_{50}	Hill slope	n	1/τ slope (M^{-1} s^{-1})	n
ELIC	WT	0.96 ± 0.23 (Cysteamine, mM)	2.26 ± 0.79	58	N.D.	3
	W224A	1.06 ± 0.21 (Cysteamine, mM)	2.84 ± 0.6	8	0.073 ± 0.008	4
	R301A	0.46 ± 0.12 [a] (Cysteamine, mM)	2.64 ± 0.98	8	0.029 ± 0.011	4
	P305A	0.27 ± 0.17 [a] (Cysteamine, mM)	1.39 ± 0.44	22	0.137 ± 0.052	5
GlyR	WT	0.23 ± 0.05 (Glycine, mM)	3.35 ± 0.81	24	N.D.	5
	W267A	NC	-	8	-	-
	W267F	0.28 ± 0.02	2.80 ± 0.20	6	0.019 ± 0.01	-
	W267L	NC	-	5	-	-
	W267A+R415W	NC	-	8	-	-
	W267A +R415A	NC	-	8	-	-
	W267R+R415W	NC	-	8	-	-
	R415A	0.25 ± 0.03 (Glycine, mM)	3.54 ± 0.62	8	0.053 ± 0.007	4
	P419A	NC	-	10	-	-
GLIC	WT	16.26 ± 6.14 (H^+, μM) (pH_{50}: 4.82 ± 0.16)	1.32 ± 0.53	32	N.D.	3
	W217A	66.1 ± 3.0 (H^+, μM) (pH_{50}: 4.18 ± 0.02)	2.53 ± 0.29	8	N.D.	-
	R296A	30.21 ± 6.71 [a] (H^+, μM) (pH_{50}: 4.53 ± 0.11)	1.28 ± 0.31	13	N.D.	-
	P300A	NC	-	10	-	-

Measurements performed 1-3 days after cRNA injection (V_{hold} ranging from -20 to -40 mV). Error values represent standard deviation. [a] $p < 0.001$ relative to wild type via one-way ANOVA followed by Dunnett's post hoc test. [b] $p<0.01$ relative to wild type via one-way ANOVA followed by Dunnett's post hoc test. [c]Data from Henault et al 2015. [d]Data from Therien & Baenziger 2017. N.D.: not determined; the slope could not be reliably extracted from the 1/τ versus log[agonist] plot due to slow desensitization at most tested agonist concentrations. NC: no agonist-activated current observed.

3.2.3 Effects of W-R-P pocket mutations in ELIC, GlyR, and GLIC

Given the limited functional expression with mutations to the W-R-P motif in the GlyR, I further tested the hypothesized conserved mechanism of lipid action by extending the Ala mutagenesis to those residues lining the W-R-P pocket in each of the three pLGICs. In ELIC, limited mutations to residues lining this pocket invariably lead to accelerated rates of desensitization. One interpretation is that the mutations reduce lipid binding leading to enhanced desensitization rates (Hénault et al., 2019). A definitive interpretation, however, is complicated because it is not possible to predict whether a given Ala mutation to a pocket lining residue will enhance, reduce or have no effect on lipid binding. Furthermore, some residues in the pocket lie close to the proposed cytoplasmic desensitization gate (Gielen et al., 2015a; Gielen & Corringer, 2018a) and could thus influence desensitization by an M4 independent mechanism. As a result, I limit my interpretations of the mutations performed in this section to a comparison of whether mutations to residues lining the W-R-P pocket in each pLGIC ultimately influence the observed macroscopic desensitization rates.

In ELIC, Ala substitutions of residues lining the W-R-P pocket had minimal effects on the EC_{50} for the agonist cysteamine relative to WT (**Figure 3-5**). Several pocket mutations, however, produced measurable increases in desensitization rates. Specifically, F274A, L278A, I281A and H285A, each resulted in a fast-desensitizing phenotype consistent with previous studies (Hénault et al., 2019). Notably, the mutations W220A on M1 and L278A on M3 enhanced the rates of desensitization (at least ~10-fold increase in the $1/\tau$ slope values), despite being positioned in the upper part of the pocket, away from the lipid headgroup region. Changes to the W-R-P pocket in ELIC therefore modulate desensitization across a broad range of residues, not only at the W-R-P motif.

In the GlyR, Ala substitutions within the W-R-P pocket produced mixed outcomes. Five of the ten mutations expressed well and had minimal effect on the EC_{50} for glycine relative

to WT, while the other five yielded no glycine-evoked currents. Among the functional mutations, the mutations L323A and R333A, and L423A enhanced desensitization rates, with L323A producing the fastest decay ($1/\tau$ slope ~ 0.16 $M^{-1}s^{-1}$), approximately 3-fold faster than R333A and 5-fold faster than L423A (**Figure 3-6, Table 3-2**). All Ala mutations of aromatic residues in the GlyR W-R-P pocket (W263A, F319A, F330A) abolished glycine-activated current. To obtain expressing mutants at these positions for functional characterization, I tested conservative substitutions that retained aromatic character. W263F, W267F, F319Y, and F330Y restored function, with EC_{50} values comparable to WT (**Figure 3-6, Table 3-2, Appendix**). These rescued receptors showed desensitization rates similar to WT.

In GLIC, Ala substitutions to residues lining the W-R-P pocket had modest effects on pH_{50} values relative to WT, except for W213A, which abolished proton-activated currents (**Figure 3-7, Table 3-2**). Significantly, none of the functional Ala substitutions measurably altered desensitization rates. Slight current decay was observed in some mutants (for example, I271A) at extreme pH values, but the decay was too slow to be reliably quantified and occurred only at the same H^+ concentrations where the apparent decay in WT GLIC could reflect inactivation rather than desensitization. Residues lining the W-R-P pocket in GLIC therefore do not appear to influence desensitization under the conditions tested.

Figure 3-5 Ala mutations to the W-R-P pocket accelerate ELIC desensitization

a. Structural representation of the ELIC W-R-P pocket highlighting the core W-R-P residues (Trp224, Arg301, Pro305) and the pocket residues tested (sticks, carbon). **b.** Representative whole-cell TEVC recordings from oocytes expressing wildtype ELIC, F274A, H285A, and L278A in response to increasing cysteamine concentrations. Horizontal bars above each trace represent the time the indicated concentration of agonist was exposed to the oocyte. Scale bars are shown on each trace. **c.** Dose-response curves (normalized current (I/I_{max}) versus ligand concentration) for wildtype (red) and H285A, L278A, and F274A Ala mutants. Data were fit with a variable-slope sigmoidal function. **d.** Plot of $1/\tau$ versus Log [Cysteamine, M] for P305A, H285A, L278A, and F274A. Solid lines represent linear fits to data points meeting reliability criteria. Error bars represent S.D. from at least 3 independent measurements ($n \geq 3$).

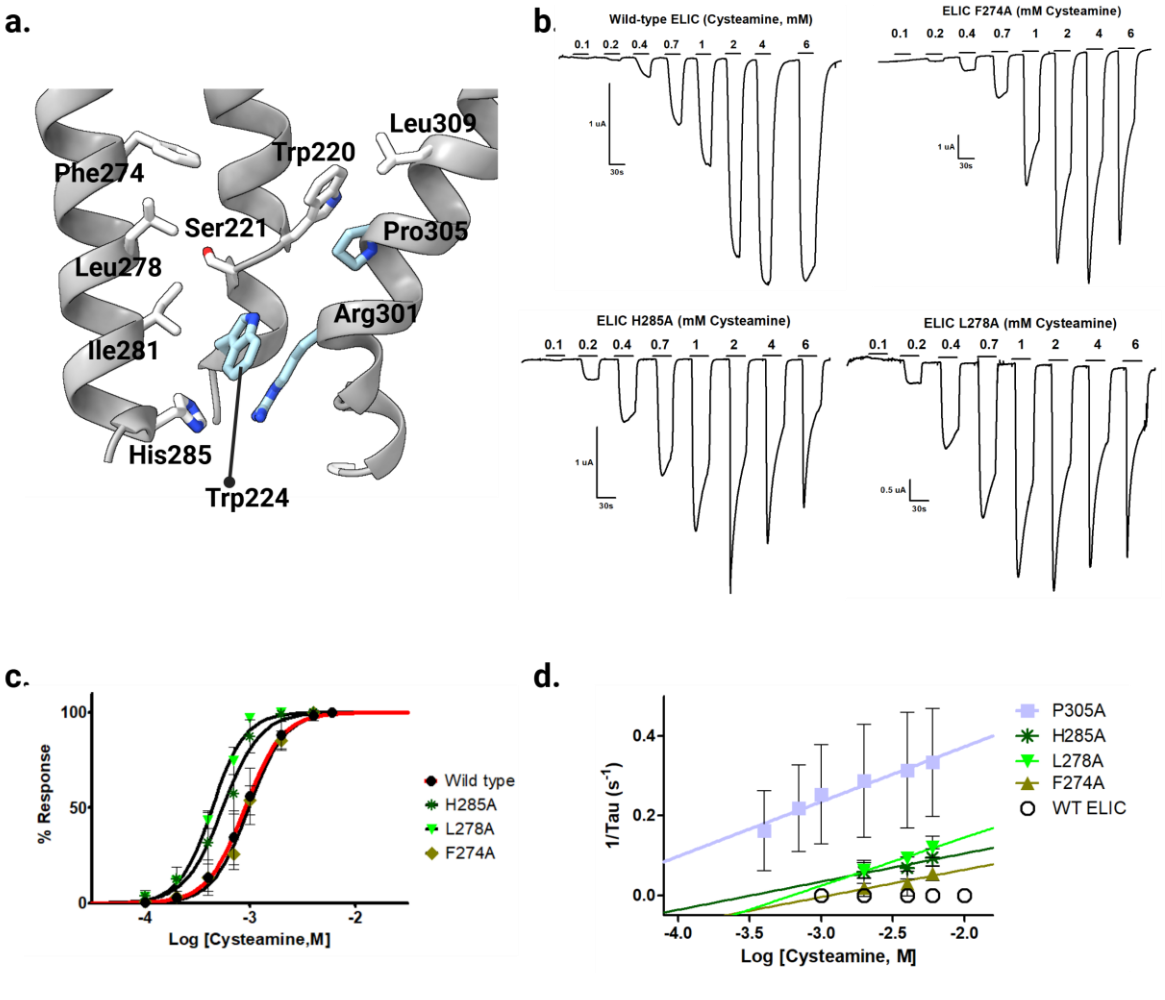
a.
Leu309
Trp220
Phe274
Ser221
Pro305
Leu278
Arg301
Ile281
His285
Trp224
b.
Wild-type ELIC (Cysteamine, mM)
0.1 0.2 0.4 0.7 1 2 4 6
1 uA
30s
ELIC F274A (mM Cysteamine)
0.1 0.2 0.4 0.7 1 2 4 6
1 uA
30s
ELIC H285A (mM Cysteamine)
0.1 0.2 0.4 0.7 1 2 4 6
1 uA
30s
ELIC L278A (mM Cysteamine)
0.1 0.2 0.4 0.7 1 2 4 6
0.5 uA
30s
c.
% Response
100
50
0
-4
-3
-2
Log [Cysteamine,M]
Wild type
H285A
L278A
F274A
d.
1/Tau (s-1)
0.4
0.2
0.0
-4.0
-3.5
-3.0
-2.5
-2.0
Log [Cysteamine, M]
P305A
H285A
L278A
F274A
WT ELIC

Figure 3-6 Some W-R-P pocket Ala mutations accelerate desensitization in GlyR while others abolish function.

a. Structural representation of the GlyR W-R-P pocket with the core motif residues (Trp267, Arg415, Pro419) and the pocket residues tested shown as sticks (carbon). **b.** Representative whole-cell TEVC recordings of WT GlyR, R415A, L323A, and V264A in response to increasing glycine concentrations. Horizontal bars above each trace represent the time the indicated concentration of agonist was exposed to the oocyte. Scale bars are shown on each trace. **c.** Agonist concentration-response curves for WT (red) and R415A, R333A, L423A, V264A, T412A, and L323A. **d.** Dose-response curves (normalized current (I/I_{max}) versus ligand concentration) for WT (red) and the aromatic substitutions F330Y, W267F, W263F, and F319Y. **e.** Plot of $1/\tau$ versus Log [Glycine, M] for L323A, R333A, R415A, and L423A. Solid lines represent linear fits to data points meeting reliability criteria. Error bars represent S.D. from at least 3 independent measurements ($n \geq 3$).

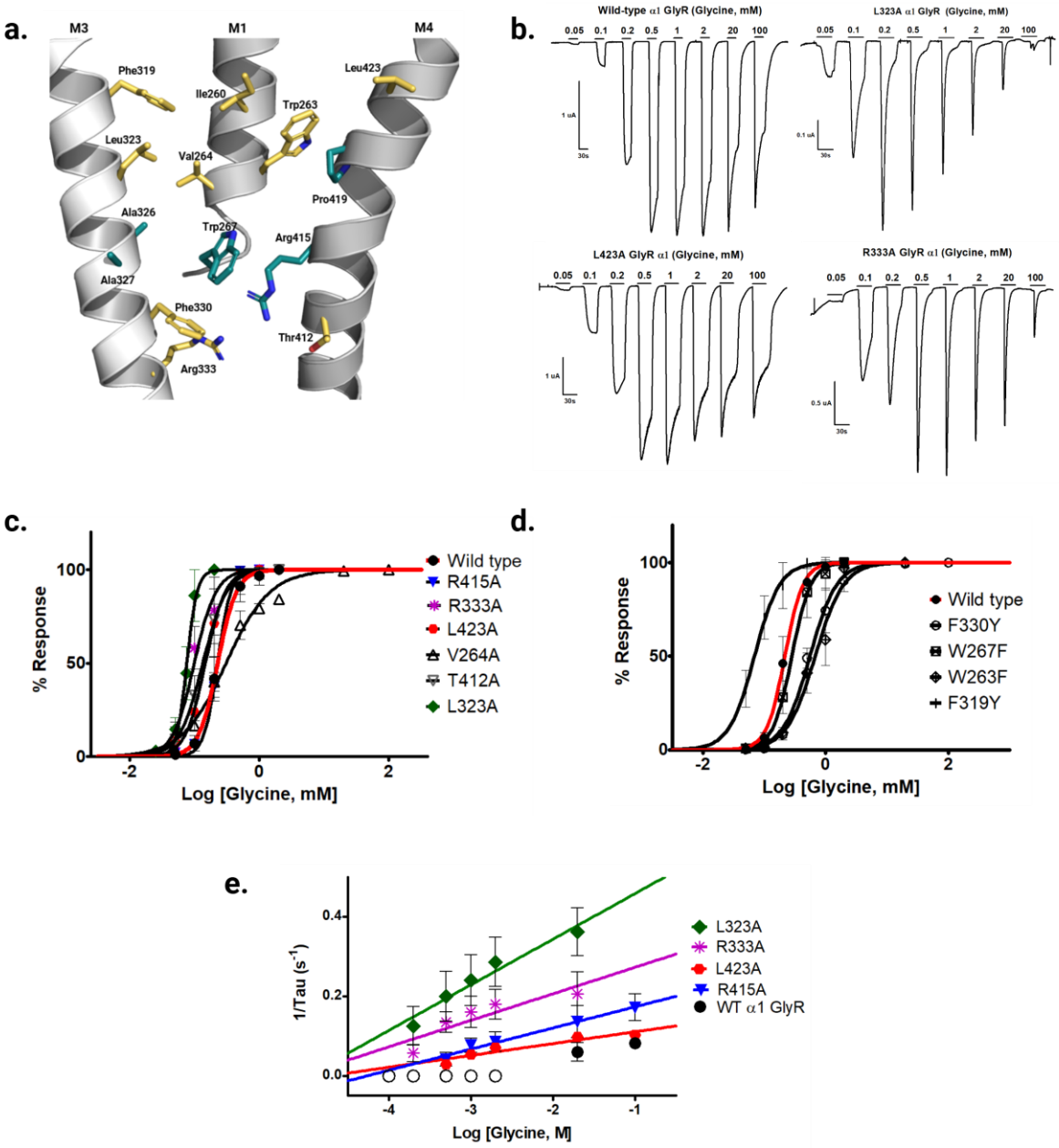
a.
M3
M1
M4
Phe319
Ile260
Trp263
Leu423
Leu323
Val264
Pro419
Ala326
Trp267
Arg415
Ala327
Phe330
Thr412
Arg333
b.
Wild-type α1 GlyR (Glycine, mM)
L323A α1 GlyR (Glycine, mM)
L423A GlyR α1 (Glycine, mM)
R333A GlyR α1 (Glycine, mM)
0.05 0.1 0.2 0.5 1 2 20 100
c.
% Response
Log [Glycine, mM]
Wild type
R415A
R333A
L423A
V264A
T412A
L323A
d.
% Response
Log [Glycine, mM]
Wild type
F330Y
W267F
W263F
F319Y
e.
1/Tau (s-1)
Log [Glycine, M]
L323A
R333A
L423A
R415A
WT α1 GlyR

Figure 3-7 Ala mutations to the W-R-P pocket do not measurably affect GLIC desensitization.

a. Structural representation of the GLIC W-R-P pocket with the core motif residues (Trp217, Arg296, Pro300) and the pocket residues tested shown as sticks (carbon). **b.** Representative whole-cell TEVC recordings of WT GLIC, R296A, Q284A, and I271A in response to increasing H^+ concentrations (decreasing pH). Horizontal bars above each trace represent the time the indicated concentration of agonist was exposed to the oocyte. Scale bars are shown on each trace. **c.** Agonist concentration-response curves for WT (red) and R296A, E282A, L279A, Q284A, Y278A, I271A, and T274A. Data were fit with a variable-slope sigmoidal function. Error bars represent S.D. from at least 3 independent measurements ($n \geq 3$).

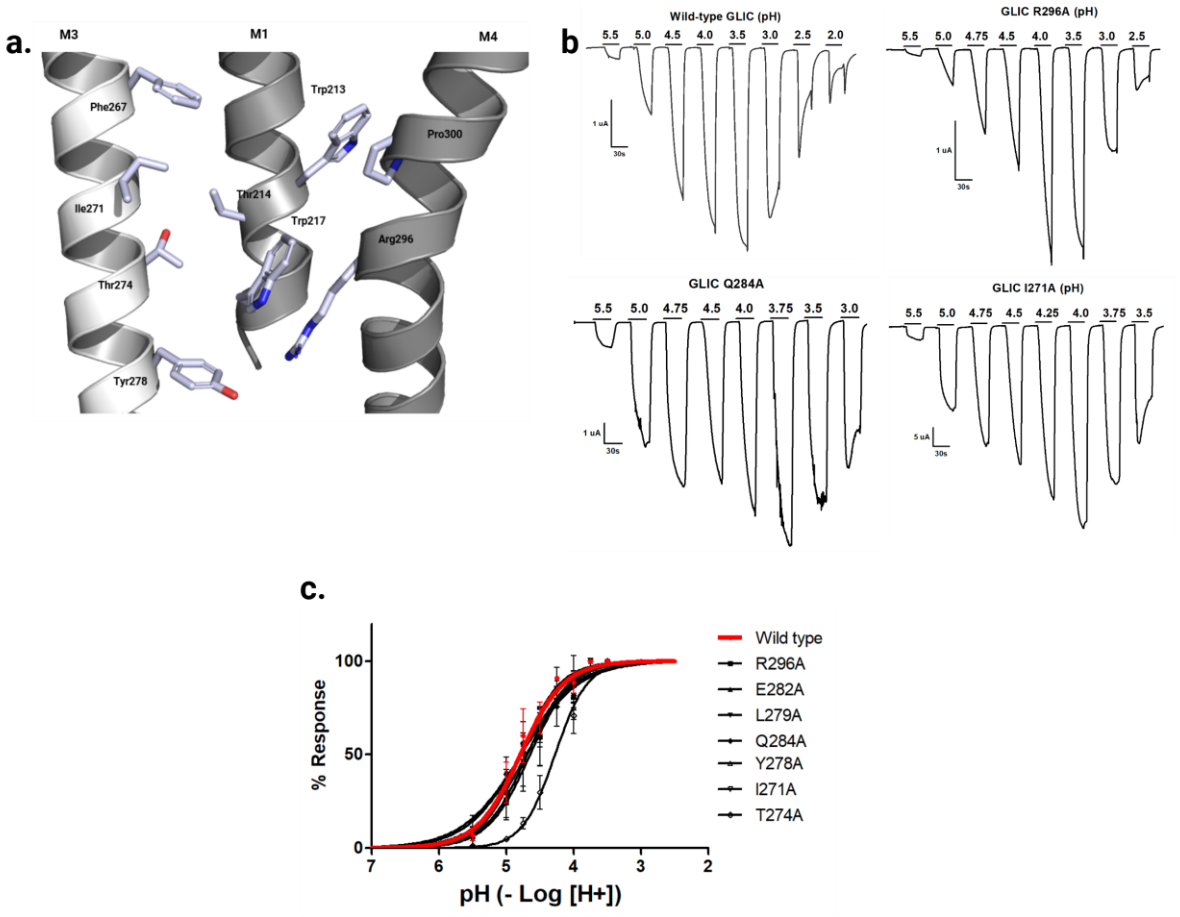
a.
M3
M1
M4
Phe267
Trp213
Pro300
Ile271
Thr214
Trp217
Arg296
Thr274
Tyr278
b
Wild-type GLIC (pH)
5.5 5.0 4.5 4.0 3.5 3.0 2.5 2.0
GLIC R296A (pH)
5.5 5.0 4.75 4.5 4.0 3.5 3.0 2.5
GLIC Q284A
5.5 5.0 4.75 4.5 4.0 3.75 3.5 3.0
GLIC I271A (pH)
5.5 5.0 4.75 4.5 4.25 4.0 3.75 3.5
c.
% Response
100
50
0
7 6 5 4 3 2
pH (- Log [H+])
Wild type
R296A
E282A
L279A
Q284A
Y278A
I271A
T274A

Table 3-2 Effects of W-R-P pocket mutations on desensitization in ELIC, GlyR, and GLIC.

pLGIC	Mutant	EC_{50} (Agonist) / pH_{50}	Hill slope	n	1/τ slope (M^{-1} s^{-1})	n
ELIC	WT	0.96 ± 0.23 (Cysteamine, mM)	2.26 ± 0.79	58	N.D.	-
	W220A	0.76 ± 0.18 (Cysteamine, mM)	2.96 ± 0.20	9	0.111 ± 0.066	3
	S221A	1.97 ± 0.40 [a] (Cysteamine, mM)	2.37 ± 0.25	9	N.D.	-
	F274A	1.04 ± 0.12 (Cysteamine, mM)	2.77 ± 1.08	8	0.069 ± 0.032	5
	L278A	0.48 ± 0.01 [b] (Cysteamine, mM)	2.62 ± 0.23	5	0.121 ± 0.035	2
	I281A	0.26 ± 0.02 (Cysteamine, mM)	2.61 ± 0.45	6	0.061 ± 0.017	4
	H285A	0.61 ± 0.16 [a] (Cysteamine, mM)	2.54 ± 1.02	8	0.071 ± 0.043	3
	Q298A	0.56 ± 0.09 [b] (Cysteamine, mM)	2.90 ± 0.22	7	N.D.	-
	L309A	0.52 ± 0.08 [a,c] (Cysteamine, mM)	2.76 ± 0.53	8	N.D.	
GlyR	WT	0.23 ± 0.05 (Glycine, mM)	3.35 ± 0.81	24	N.D.	5
	W263A	NC	-	-	N/A	-
	W263F	0.67 ± 0.03 [a] (Glycine, mM)	1.87 ± 0.20	5	N.D.	-
	V264A	0.26 ± 0.05 (Glycine, mM)	1.45 ± 0.20	8	N.D.	3
	F319A	NC	-	6	-	-
	F319H	NC		4	-	-
	F319Y	0.07 ± 0.04 (Glycine, mM)	2.11 ± 0.40	2*	N.D.	-
	F319L	NC	-	6	-	-
	L323A	0.11 ± 0.02 (Glycine, mM)	3.60 ± 1.81	8	0.159 ± 0.038	4
	F330A	NC	-	-	-	-
	F330Y	0.55 ± 0.01 [a] (Glycine, mM)	2.01 ± 0.11	9	N.D.	-
	F330H	NC	-	4	-	-
	F330L	NC	-	4	-	-
	R333A	0.11 ± 0.03 (Glycine, mM)	2.84 ± 1.14	5	0.122 ± 0.025	3
	T412A	0.13 ± 0.02	2.42 ± 0.54	7	N.D.	-
	P419A	NC	-	10	-	-

	L423A	0.16 ± 0.03 (Glycine, mM)	3.07 ± 0.70	8	0.030 ± 0.004	3
GLIC	WT	16.26 ± 6.14 (H^+, µM) (pH_{50}: 4.82 ± 0.16)	1.32 ± 0.53	32	N.D.	-
	W213A	NC	-	10	-	-
	T214A	2.33 ± 0.94 [a] (H^+, µM) (pH_{50}: 5.67 ± 0.18)	0.90 ± 0.06	6	N.D.	-
	F267A	8.21 ± 6.02 (H^+, µM) (pH_{50}: 5.21 ± 0.33)	2.68 ± 0.36	8	N.D.	-
	I271A	25.7 ± 18.03 (H^+, µM) (pH_{50}: 4.68 ± 0.27)	1.30 ± 0.20	7	N.D.	-
	T274A	59.1 ± 17.30 [a] (H^+, µM) (pH_{50}: 4.25 ± 0.12)	1.88 ± 0.20	6	N.D.	-
	Y278A	3.06 ± 0.68 [d] (H^+, µM) (pH_{50}: 5.52 ± 0.10)	2.73 ± 0.44	8	N.D.	-
	F303A	33.1 ± 6.20 [d] (H^+, µM) (pH_{50}: 4.48 ± 0.09)	1.85 ± 0.65	8	N.D.	-

Measurements performed 1-3 days after cRNA injection (V_{hold} ranging from -20 to -40 mV). Error values represent standard deviation. [a] $p < 0.001$ relative to wild type via one-way ANOVA followed by Dunnett's post hoc test. [b] $p<0.01$ relative to wild type via one-way ANOVA followed by Dunnett's post hoc test. [c]Data from Henault et al 2015. [d]Data from Therien & Baenziger 2017. N.D.: not determined; the 1/τ slope could not be reliably extracted from the 1/τ versus log[agonist] plot due to slow desensitization at most tested agonist concentrations. NC: no agonist-activated current observed.

Taken together, the results show that residues lining the W-R-P pocket influence desensitization in ELIC and GlyR, but not in GLIC. In ELIC, Ala mutations at nearly every residue lining the pocket, whether charged, aromatic, hydrogen bonding, or aliphatic, produced measurable increases in desensitization rates. In GlyR, only a subset of pocket mutations accelerated desensitization, but the 1/τ slopes span a broader range than for ELIC W-R-P pocket mutants, with L323A, in particular, approaching the rate seen with ELIC P305A. Notably, L323 in GlyR is the structural equivalent to L278 in ELIC, which also showed strong effects on desensitization. In GLIC, none of the functional pocket mutations measurably altered desensitization, including I271A, the structural equivalent of L278 in ELIC and L323 in GlyR.

3.2.4 Effects of the Pro-kink position on desensitization in ELIC, GlyR, and GLIC

The Pro-induced kink in M4 appears critical for the slow desensitizing phenotype in ELIC, with the Pro to Ala mutation in ELIC, which eliminates the kink, producing the most dramatic effect on desensitization of any single-site W-R-P motif mutant. The elimination of the kink should lead to a dramatically altered binding conformation of M4 relative to the rest of the TMD. In the GlyR (P419A) and GLIC (P300A), elimination of the kink leads to non-functional expression, preventing a direct test of the role of the M4 conformation in desensitization. To test how more subtle changes in M4 conformation influence desensitization in the GlyR and GLIC, I shifted the Pro-induced kink either one helical turn above or below its native position. In ELIC, such subtle repositioning increases desensitization rates relative to WT, although not to the same extent of P305A itself (Hénault et al., 2019). In GlyR and GLIC, however, both shifts resulted in non-functional and/or unexpressed receptors at the cell surface (**Table 3-3**). These results suggest that in the GlyR and GLIC, the native Pro-kink position is critical for folding and/or function, with even subtle disruptions in the position of the kink affecting folding, trafficking, and/or channel function. In ELIC, by contrast, the TMD appears more permissive to geometric changes in M4 or dynamics.

Table 3-3 Effects of shifting the M4 Pro-kink on GlyR and GLIC function.

pLGIC	Mutant	EC_{50} (Agonist)	Hill slope	n
ELIC	WT	0.96 ± 0.23 (Cysteamine, mM)	2.26 ± 0.79	58
	P304A + R301P	0.49 ± 0.20[a] (Cysteamine, mM)	2.68 ± 0.34	7
	P305A + L309P	0.18 ± 0.03[a] (cysteamine, mM)	2.85 ± 0.22	8
GlyR	WT	0.23 ± 0.05 (Glycine, mM)	3.35 ± 0.81	24
	P419A + R415P	NC	-	8
	P419A + L423P	NC	-	10
GLIC	WT	16.26 ± 6.14 (H^+, μM) (pH_{50}: 4.82 ± 0.16)	1.32 ± 0.53	32
	P300A + R296P	NC	-	5
	P300A + L304P	NC	-	5

Measurements performed 1-3 days after cRNA injection (V_{hold} ranging from -20 to -40 mV). Error values represent standard deviation. [a] Data from Henault et al 2015 NC: no agonist-activated current observed.

3.2.5 M4 C-terminal truncations accelerate desensitization in ELIC but abolish function in GlyR and GLIC

The post-M4 region differs across the three pLGICs. ELIC and GLIC have no post-M4 extension as M4 ends at the C-terminus of the protein. The GlyR, by contrast, has a post-M4 extension of approximately 10 residues that extends up toward the ECD and approaches the agonist-binding site (A. Kumar et al., 2020a). Deletions of up to seven residues (Δ7) at the C-terminus of M4 in ELIC are well tolerated with minimal impact on either EC_{50} values or the rates of desensitization. Deletion of the final eight residues (Δ8) or the entire M4, however, leads to a rapid desensitizing phenotype similar to that of P305A. Furthermore, density for M4 was not observed in the crystal structure of the Δ8 mutant, consistent with increased M4 disorder or dynamics in the absence of these C-terminal interactions. In GLIC, by contrast, C-terminal deletions are not tolerated. Specifically, deletion of the final three or more residues at the C-terminus of M4 in GLIC results in a complete loss of receptor expression and/or function (Hénault et al., 2015) (**Table 3-4**).

To determine whether M4 C-terminal deletions in the GlyR influence desensitization, I generated Δ1 (Gln 444; dQ), Δ2 (Lys 443 and Gln 444; dKQ), Δ4 (Ile 441, His442, Lys 443 and Gln 444; dIHKQ), Δ8 (Arg 437 to Gln 444; dRSEDIHKQ) and Δ16 (Tyr429 to Gln 444; dYWITYKIIRSEDIHKQ) mutants, with the position of the Δ16 truncation corresponding roughly to the position of the fast-desensitizing Δ8 mutation in ELIC. Surprisingly, none of these GlyR deletions produced measurable agonist-evoked currents, including the minimal Δ1 deletion that removes only the C-terminal Gln 444 from the post-M4 extension (**Figure 3-8**). These results suggest that the post-M4 region is essential for channel expression and/or function in GlyR, likely through stabilizing interactions with the ECD.

The contribution of the M4 C-terminus to the folding and/or function clearly differs across pLGICs. In ELIC, deleting the C-terminus enhances desensitization, consistent with increased M4 disorder or dynamics in the absence of these C-terminal interactions. In contrast, in GlyR and GLIC, even minimal deletions compromise receptor expression and/or function. As with the Pro-kink shifts, ELIC tolerates C-terminal deletions to M4 that are not tolerated in GlyR or GLIC, preventing a direct test of how these deletions affect desensitization in those receptors.

Figure 3-8 M4 C-terminal deletions are tolerated in ELIC but abolish function in α1 GlyR and GLIC

(a) Structural representation of the ELIC TMD highlighting the deleted M4 C-terminal residues as black Cα sphere (left), and representative whole-cell TEVC recordings from Δ7 and Δ8 ELIC mutants. Horizontal bars above each trace represent the time the indicated concentration of agonist was exposed to the oocyte. (right).

(b) Structural representation of the GlyR TMD highlighting the deleted M4 C-terminal residues as black Cα sphere (left), and representative recordings from GlyR C-terminal deletion mutants. Horizontal bars above each trace represent the time the indicated concentration of agonist was exposed to the oocyte (right).

(c) Structural representation of the GLIC TMD highlighting the deleted M4 C-terminal residues as black Cα sphere (left), and representative proton-activated currents from GLIC deletion mutants (right). Data obtained from Henault et al 2015.

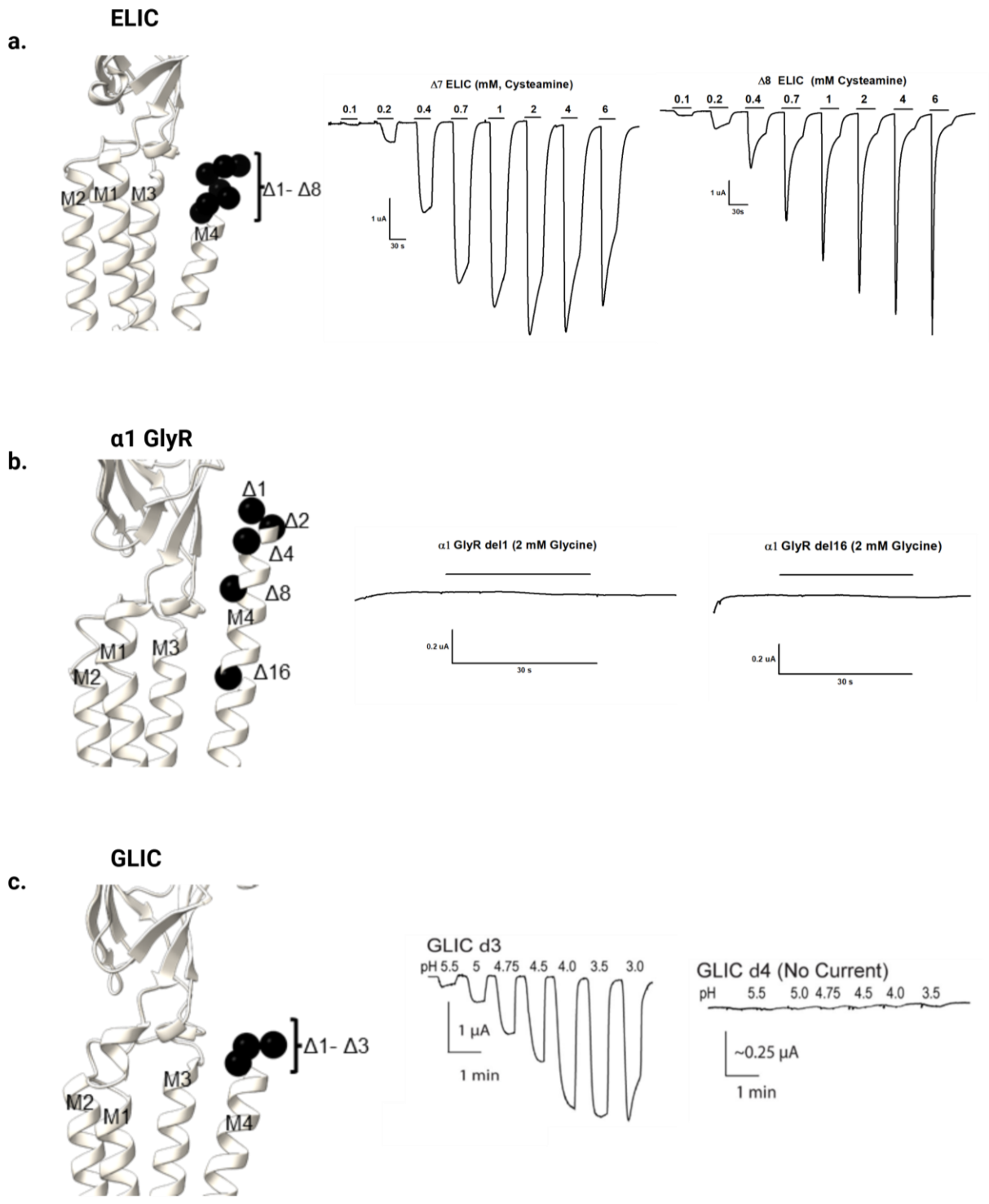
a.
ELIC
M2
M1
M3
M4
Δ1- Δ8
Δ7 ELIC (mM, Cysteamine)
0.1
0.2
0.4
0.7
1
2
4
6
1 uA
30 s
Δ8 ELIC (mM Cysteamine)
0.1
0.2
0.4
0.7
1
2
4
6
1 uA
30s
b.
α1 GlyR
Δ1
Δ2
Δ4
Δ8
M4
M1
M3
M2
Δ16
α1 GlyR del1 (2 mM Glycine)
0.2 uA
30 s
α1 GlyR del16 (2 mM Glycine)
0.2 uA
30 s
c.
GLIC
Δ1- Δ3
M3
M2
M1
M4
GLIC d3
pH 5.5 5 4.75 4.5 4.0 3.5 3.0
1 μA
1 min
GLIC d4 (No Current)
pH 5.5 5.0 4.75 4.5 4.0 3.5
~0.25 μA
1 min

Table 3-4 Effects of M4 C-terminal deletions on channel function in ELIC, GlyR, and GLIC.

pLGIC	Mutant	EC_{50} (Agonist)	Hill slope	n
ELIC [c]	WT	0.96 ± 0.23 (Cysteamine, mM)	2.26 ± 0.79	58
	Δ1- dL	0.62 ± 0.04[b] (Cysteamine, mM)	2.30 ± 0.26	5
	Δ2- dTL	0.56 ± 0.05[b] (Cysteamine, mM)	2.67 ± 0.42	11
	Δ3- dITL	0.81 ± 0.08[a] (Cysteamine, mM)	2.62 ± 0.36	8
	Δ4- dGITL	0.68 ± 0.07[b] (Cysteamine, mM)	2.66 ± 0.43	9
	Δ5- dRGITL	0.68 ± 0.09[b] (Cysteamine, mM)	2.63 ± 0.55	9
	Δ6- dIRGITL	0.54 ± 0.08[b] (Cysteamine, mM)	2.40 ± 0.55	10
	Δ7- dVIRGITL	0.50 ± 0.06[b] (Cysteamine, mM)	2.45 ± 0.28	12
GlyR	WT	0.23 ± 0.05 (Glycine, mM)	3.35 ± 0.81	24
	Δ1 dQ	NC	NC	15
	Δ2- dKQ	NC	NC	8
	Δ4- dIHKQ	NC	NC	8
	Δ8- dRSEDIHKQ	NC	NC	8
	Δ16-dYWITYKIIRSEDIHKQ	NC	NC	10
GLIC[c]	WT	16.26 ± 6.14 (H^+, μM) (pH_{50}: 4.82 ± 0.16)	1.32 ± 0.53	32
	Δ1- dF	pH_{50}: 5.15 ± 0.13[a]	1.65 ± 0.26	9
	Δ2- dGF	pH_{50}: 5.03 ± 0.20	1.42 ± 0.20	8
	Δ3- dFGF	pH_{50}: 4.42 ± 0.18[b]	1.64 ± 0.46	10
	Δ4- dFFGF	NC	NC	8
	Δ5- LFFGF	NC	NC	8

Measurements performed 1-3 days after cRNA injection (V_{hold} ranging from -20 to -40 mV). Error values represent standard deviation. Error values represent standard deviation. [a] $p < 0.001$ relative to wild type via one-way ANOVA followed by Dunnett's post hoc test. [b] $p<0.01$ relative to wild type via one-way ANOVA followed by Dunnett's post hoc test. [c]Data from Henault et al 2015. NC: no agonist-activated current observed.

3.3 Discussion

Compelling data suggested that lipid binding to the W-R-P pocket in ELIC modulates channel desensitization (Hénault et al., 2019). The current model proposes that lipids bind to this pocket, shaped by the W-R-P motif (Trp 224, Arg301, Pro305), and stabilize a kinked conformation of M4. In the absence of lipid-binding, M4 adopts a different position relative to M1/M3 and/or becomes more dynamic, leading to faster desensitization (Hénault et al., 2019). Although the W-R-P motif is conserved in anion-selective pLGICs and GLIC, it is not known whether this model applies more broadly across the pLGIC family. Structural data show that lipids or lipidic modulators bind at the homologous site in $GABA_A$Rs (Laverty et al., 2017a; A. G. Lee, 2021a) and GLIC (Bocquet, Nury, Baaden, Le Poupon, et al., 2009), establishing the W-R-P pocket as a conserved lipid binding site. In this chapter, I *indirectly* tested whether lipid binding to this pocket influences desensitization in the GlyR and GLIC by a similar M4-dependent mechanism by comparing the effects of perturbations to the W-R-P motif, the W-R-P pocket, the Pro-kink position, and the M4 C-terminus on desensitization across the three pLGICs. The results suggest that the W-R-P pocket plays different roles in modulating desensitization across the three pLGICs tested. This conclusion is based on the following observations:

First, despite the conservation of the W-R-P motif across ELIC, GlyR, and GLIC, mutations to these conserved residues produced different effects on desensitization in each receptor. In ELIC and GlyR, those mutations that expressed accelerated desensitization, while in GLIC they had no measurable effect. Given the importance of the W-R-P motif in establishing M4 conformation and/or dynamics (Chapter 4), these results suggest that either 1) M4 conformation/dynamics in GLIC do not influence desensitization or 2) that additional aromatic residues strengthen M4-M1/M3 interactions in GLIC to dampen the effects of the W-

R-P mutations on M4 conformation/dynamics. The results suggest that M4 structure plays a less dominant role in modulating desensitization in GLIC versus ELIC.

Second, most alanine mutations (8 out of 10) to residues lining the W-R-P pocket in ELIC accelerate desensitization, consistent with previous data (Hénault et al., 2019). One possible interpretation is that replacing bulky sidechains with alanine's methyl group weakens the van der Waals interactions between lipid acyl chains and pocket residues, which could lower the binding affinity of the lipid and thereby increase M4 dynamics or M4 conformation relative to M1/M3 to accelerate desensitization. Enhanced desensitization of ELIC is also observed when reconstituted into membranes lacking PE/PG (Hénault et al., 2019). Note that the Ala mutations could also relieve steric constraints in the pocket and enhance lipid binding, in which case the observed acceleration of desensitization would have to be explained by an M4 independent mechanism. The mutagenesis data alone cannot distinguish these possibilities. Direct evidence for PG binding at the W-R-P pocket comes from the native mass spectrometry, which showed that mutating three arginines at or adjacent to the W-R-P pocket - R286, R299, and R301 (the W-R-P arginine) - reduces PG binding (Tong et al., 2019). Subsequent work from the Cheng group has identified another outer leaflet PG site (Petroff et al., 2022; Tan et al., 2025), and the relative contributions of the two sites to ELIC desensitization remain to be determined.

Third, Pro305 defines a kink in M4, and its substitution to Ala results in fast desensitization kinetics in ELIC. The exact geometry of the M4 kink is also important for tuning desensitization, as shifting the Pro-kink by one helical turn up or down accelerates desensitization (Hénault et al., 2019). The cation-π interaction between Trp224 and Arg301 provides an additional structural anchor within the pocket. Cation-π interactions between Arg and Trp side chains are among the strongest non-covalent interactions in proteins (Gallivan & Dougherty, 1999), with binding energies in solvated regions of approximately -4.7 kcal/mol

(Calinsky & Levy, 2024) and are enriched at the interfaces of protein complexes. Disrupting this interaction by mutating either residue (W224A or R301A) results in fast-desensitizing phenotypes. The relative contributions of pocket geometry, lipid binding, and the Trp224-Arg301 cation-π interaction to ELIC desensitization are examined in detail in Chapter 4.

In the GlyR, mutations that were functional gave a phenotype broadly consistent with ELIC. R415A, the only W-R-P motif mutant that expressed, accelerated desensitization. Several pocket mutations (L323A, R333A, and L423A) also accelerated desensitization, with L323A approaching the fastest rates seen with ELIC P305A. L323 in GlyR is the structural equivalent of L278 in ELIC, which is also one of the fast-desensitizing mutants in the ELIC pocket. The Ala substitutions of the pocket aromatic residues (W267A, F319A, F330A) abolished function, preventing a direct test of how these residues contribute to desensitization. Together, these results suggest that the W-R-P pocket plays a role in modulating desensitization in GlyR.

Several caveats hinder a direct interpretation of the mechanism by which these residues modulate desensitization. Two of the GlyR pocket mutations that increased desensitization (L323A and R333A) are positioned near the M2-M3 interface, close to residues involved in the proposed desensitization gate at the -2' position (Gielen et al., 2015a). Whether their effects on desensitization arise from altered lipid binding and changes in M4 position relative to M1 and M3 or M4 dynamics, or from direct structural effects on the desensitization gate, cannot be distinguished from the current mutagenesis data alone.

In GLIC, mutations to the W-R-P motif and pocket had no measurable effect on desensitization. The simplest interpretation is that the proposed model of lipid binding to the W-R-P pocket modulating desensitization through changes in M4 dynamics or M4 position relative to M1 and M3 does not apply in GLIC. Previous functional and spectroscopic studies have shown that GLIC desensitizes slowly, with slower kinetics that are difficult to quantify

by TEVC (Basak et al., 2017; Gielen & Corringer, 2018a; Velisetty & Chakrapani, 2012), so subtle effects of pocket mutations may fall below the resolution of TEVC. More sensitive techniques such as outside-out patch recordings could test this. Another possibility is that WT GLIC openings are shorter-lived or less frequently populated, so that desensitization rarely occurs within the recording window. If this is the case, pocket mutations could affect desensitization in GLIC without producing a measurable change in the TEVC current. This remains to be tested directly through single-channel measurements of GLIC open times and open probability.

One explanation for the different phenotypes across the three pLGICs is that M4 itself could be intrinsically more dynamic in ELIC than in GlyR or GLIC, so the link between M4 conformation or dynamics and desensitization can be probed in ELIC more directly than in the other two receptors. One structural reason for this difference is the density of aromatic interactions at the M4-M1/M3 interface. GLIC and GlyR both have extensive networks of aromatic interactions at this interface (Cory-Wright et al., 2018; Haeger et al., 2009), while ELIC has relatively few aromatic interactions in the same region (Therien & Baenziger, 2017) (**Figure 3-9**). A dense aromatic network would constrain M4 motion and tighten M4-M1/M3 packing, making M4 less dynamic and less tolerant of perturbations. This is consistent with the experimental observations: in ELIC, all of the M4 perturbations tested in this chapter were tolerated, including M4-kink shifts, C-terminal deletions, and pocket Ala mutations. In GLIC, by contrast, similar perturbations either abolished function (Pro-kink elimination, kink shifts, C-terminal deletions) or had limited effects on desensitization (pocket Ala mutations). GlyR sits between these two extremes: some Ala mutations to pocket residues were tolerated and accelerated desensitization in a manner similar to ELIC, but more disruptive perturbations such as kink shifts and C-terminal deletions abolished function, as in GLIC. GlyR also has a large ICD, absent in ELIC and GLIC, that has been shown to influence channel function and

desensitization (Ivica et al., 2021; Langlhofer et al., 2015; Langlhofer & Villmann, 2016; Papke & Grosman, 2014)., which may contribute to its intermediate behavior.

This interpretation is consistent with the observation that GLIC retains agonist-induced conformational transitions in PC-only membranes, while ELIC does not, a difference attributed to the strength of aromatic interactions at the M4-M1/M3 interface (Carswell, Hénault, et al., 2015; Carswell, Sun, et al., 2015; Hénault et al., 2015). In this context, it is notable that the *Torpedo* nAChR, like ELIC, exhibits relatively few aromatic residues at the M4-M1/M3 interface and is also highly sensitive to its lipid environment (Baenziger et al., 2015; Mody et al., 2025; Thompson & Baenziger, 2020). More recently, a comprehensive Ala scan of the M4 helix in each subunit of the muscle nAChR showed that alanine substitutions of aromatic residues at the M4-M1/M3 interface typically led to subtle gains in function, consistent with the idea that bulky aromatic side chains may sterically constrain M4-M1/M3 interactions and that reducing side chain size promotes tighter packing (Thompson et al., 2022). These findings support a model in which the density of aromatic interactions at the M4-M1/M3 interface sets the intrinsic dynamics of M4 and, as a result, the sensitivity of each pLGIC to perturbations at this region. In ELIC, where M4 packing against M1 and M3 is weaker, lipid binding to the W-R-P pocket can have a measurable effect on desensitization through changes in M4 dynamics or M4 position relative to M1 and M3. In GlyR, pocket mutations do affect desensitization, but whether this occurs through M4 dynamics, M4 position, or through the cytoplasmic desensitization gate cannot be distinguished from the current data. In GLIC, where M4 is most constrained, lipid binding to the pocket may not produce a measurable effect on desensitization.

A further consideration for interpreting pocket mutation effects across the three pLGICs is the position of the desensitization gate. The gate itself is not proposed to be at the same position in all three receptors.

Figure 3-9 GLIC and GlyR have dense aromatic networks at the M4-M1/M3 interface, while ELIC has relatively few aromatic interactions.

Ribbon representations of the transmembrane domains highlighting residues at the M4-M1/M3 interface. Aromatic side chains are shown as red sticks.

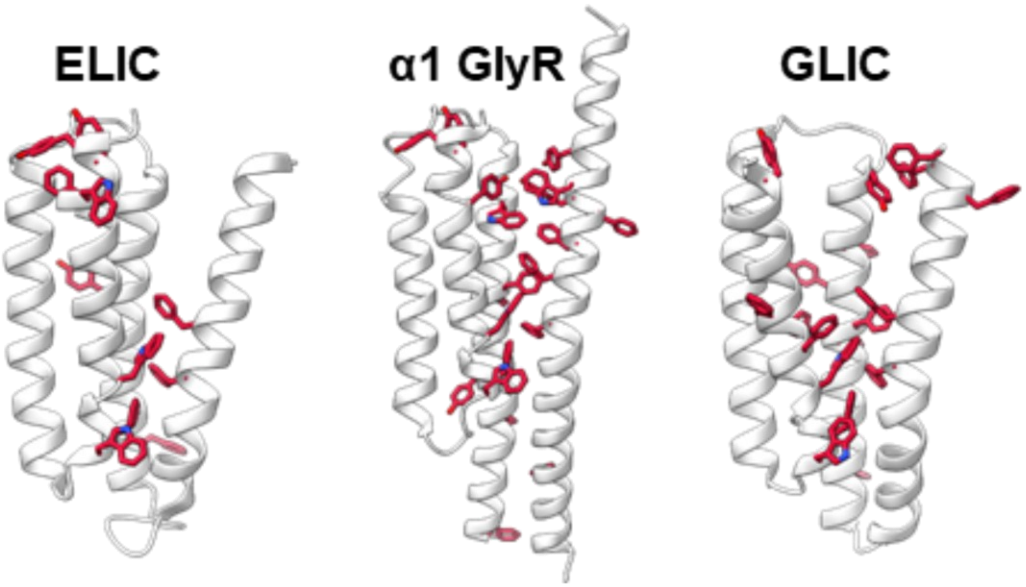
ELIC
α1 GlyR
GLIC

In ELIC, previous spectroscopy work showed that desensitization involves expansion at the extracellular end and contraction at the intracellular end of the pore, which initially suggested that the ELIC desensitization gate may overlap with that of the anion-selective ion channels (Kinde et al., 2015). Contrary to this suggestion, recent cryo-EM structures of ELIC suggest that the desensitization gate is near the L9' in the channel pore (Dalal et al., 2025). In GlyR, structural and functional data propose that the desensitization gate lies at the -2' position at the intracellular end of M2 (Gielen et. al., 2015; Gibbs et al., 2023; A. Kumar et al., 2020). In GLIC, EPR data suggests a desensitization gate near mid-membrane rather than at the intracellular end (Velisetty et al., 2012), and more recent cryo-EM structures of GLIC in nanodiscs show that the pore narrows at the I9' position in closed and pre-open states (Bharambe et al., 2024). These structural differences across the three pLGICs indicate that the desensitization gate is not at a conserved position. This means that a residue that lies near the gate in one receptor may not lie near the gate in another, so the same Ala mutation may have different downstream consequences depending on the receptor's gate position. To further define the functional and structural link between M4 and the gate in ELIC and across pLGICs more broadly, more detailed structural and functional studies will be needed.

The W-R-P pocket binds lipids and other modulators across pLGICs (A. Kumar et al., 2022a; Laverty et al., 2017a; Sun et al., 2023). In ELIC, multiple structures show lipids bound at the W-R-P pocket: PE in the first lipid-bound ELIC crystal structure (Hénault et al., 2019), PG in the cryo-EM structure of ELIC reconstituted in SMA (P. Kumar et al., 2021), and PG binding confirmed by native mass spectrometry (Tong et al., 2019). This binding is associated with effects on desensitization through changes in M4 dynamics or M4 position relative to M1 and M3, as discussed earlier. In α1 GlyR, cryo-EM structures with the cannabinoid Δ^9-tetrahydrocannabinol (THC), used for pain relief, revealed that the THC-binding site lies within the W-R-P pocket (A. Kumar et al., 2022b). Cholesterol depletion reduced cannabinoid

potentiation of glycine-activated currents in α1/α3 GlyR expressed in HEK 293T cells and in cultured spinal neurons (Yao, Wells, et al., 2020), and cross-linking mass spectrometry studies identified a cholesterol binding site in α1 GlyR that overlaps with the W-R-P pocket and the THC-binding site, supporting a modulatory role at this site (Ferraro & Cascio, 2018). In GLIC, PC has been observed bound at the W-R-P pocket in the original crystal structure (Bocquet, Nury, Baaden, Poupon, et al., 2009). In $GABA_A$Rs, the W-R-P pocket overlaps with binding sites for cholesterol, POPC, and neurosteroids (Q. Chen et al., 2018; Laverty et al., 2017a; A. G. Lee, 2021a; Miller, Scott, Masiulis, De Colibus, et al., 2017; Sun et al., 2023), and neurosteroid binding at this site potentiates channel function through a mechanism involving increased open probability (Belelli & Lambert, 2005), distinct from the proposed mechanism in ELIC. Collectively, this suggests that the W-R-P pocket binds lipids and other modulators in ELIC, GlyR, GLIC, and $GABA_A$Rs, but the effects on channel function differ across these receptors. This is consistent with the different effects of pocket mutations on desensitization observed in this chapter across ELIC, GlyR, and GLIC.

Another difference observed here between the three WT pLGICs is the agonist concentration dependence of desensitization. In ELIC, current decay becomes apparent only at cysteamine concentrations approaching full agonist occupancy, whereas in GlyR, decay is evident at sub-saturating glycine concentrations where occupancy of all five binding sites is unlikely. This pattern is consistent with single-channel evidence that α1 GlyR reaches maximum efficacy when three of the five binding sites are occupied (Beato et al., 2004), and with the general framework in which desensitization transitions depend on the fraction of receptors in the agonist-bound open state (Papke & Grosman, 2014). GLIC differs from both as no detectable decay was observed until high H^+ concentrations, where any apparent decay could reflect H^+-induced inactivation rather than desensitization. This is consistent with previous reports that GLIC has intrinsically slow desensitization kinetics (Velisetty &

Chakrapani, 2012). These differences suggest that the relationship between agonist occupancy and entry into desensitization differs across the three receptors. Whether this reflects intrinsic differences in agonist gating, in the population of states that can desensitize, or in the M4-mediated coupling discussed above cannot be distinguished from these data.

In conclusion, the data presented in this chapter demonstrates that the W-R-P pocket plays different roles in modulating desensitization across ELIC, GlyR, and GLIC, despite the conservation of the W-R-P motif and the binding of lipids and modulators at the homologous site in all three receptors. In ELIC, where the M4-M1/M3 interface is stabilized by relatively few aromatic interactions, mutations to the W-R-P pocket, the Pro-kink shifts, and the M4 C-terminus deletions accelerate desensitization. In GlyR, pocket mutations also accelerate desensitization, but more disruptive mutations to M4 abolish function, and the contributions of altered lipid binding, M4 dynamics, M4 position relative to M1 and M3, and proximity to the cytoplasmic desensitization gate cannot be distinguished from the current data. In GLIC, mutations to the W-R-P pocket had no measurable effect on desensitization, consistent with the dense aromatic network at the M4-M1/M3 interface. Collectively, these results indicate that the TMD architecture surrounding the W-R-P pocket, rather than the motif itself, shapes the functional outcome of mutations at this site. Having established these receptor-specific differences, I next focused on ELIC to understand in greater detail the mechanisms by which interactions at the W-R-P motif and the M4-M1/M3 interface modulate desensitization.

4 Chapter 4 – Interactions at the M4-M1/M3 interface modulate desensitization in ELIC

4.1 Introduction

In Chapter 3, I tested whether the W-R-P motif plays a conserved role in modulating desensitization across the pLGIC family. The results showed that the W-R-P pocket plays different roles in modulating desensitization across ELIC, GlyR, and GLIC, despite the conservation of the motif. In ELIC, perturbations to the W-R-P motif, the W-R-P pocket, the Pro-kink position, and the M4 C-terminus accelerated channel desensitization. In this chapter, I examine how interactions at the M4-M1/M3 interface contribute to the modulation of desensitization in ELIC.

The model proposed for ELIC is that lipid binding to the W-R-P pocket slows desensitization by stabilizing a kinked conformation of M4 and by slowing M4 dynamics at the M4-M1/M3 interface (Hénault et al., 2019). The evidence supporting this link is, however, indirect. The Δ8 ELIC crystal structure lacks density for the M4 helix (Hénault et al., 2019), but this could reflect mobility specific to the detergent-solubilized state used for crystallization. Several deposited ELIC structures show M4 in either a kinked or an unkinked conformation (Gonzalez-Gutierrez et al., 2012; Zimmermann & Dutzler, 2011)and the P305A mutation, which is expected to favour the unkinked conformation, accelerates desensitization, although this could also reflect an altered M4 conformation rather than increased M4 dynamics. The available data therefore suggest that M4 structure or dynamics may influence desensitization in ELIC, but do not establish this link directly.

The first goal of this chapter is to test directly whether interactions at the M4-M1/M3 interface contribute to the regulation of ELIC desensitization, as a measure of how M4 structure

or dynamics influence the rate of channel desensitization. I examine the contribution of the Trp224-Arg301 cation-π interaction at the W-R-P motif by modulating its strength through a series of substitutions and ask whether changes in the strength of this M4-M1 interaction translate into changes in the rate of desensitization. I also test whether strengthening the interactions between the C-terminus of M4 and the surrounding helices, M1 and M3, through the addition of three aromatic residues (3Aro), can compensate for mutations that weaken interactions at the W-R-P motif. The second goal is to begin to address how interactions at the M4-M1/M3 interface ultimately influence desensitization. I introduced mutations at two regions: residues at the M1-M3 interface adjacent to the Pro305 kink, which lie close to the proposed L9' gate in ELIC (Dalal et al., 2025), and residues on the M3-M4 linker, which lie close to the cytoplasmic desensitization gate at the intracellular end of M2 proposed for anion-selective pLGICs (Gielen et al., 2015a; Gielen & Corringer, 2018a).

I addressed these goals using site-directed mutagenesis and TEVC electrophysiology in *Xenopus laevis* oocytes. As all of the experiments in this chapter were performed on the same ELIC background, I present whole-cell current overlays at a saturating cysteamine concentration (10 mM, ~10-fold EC_{50}), which allow direct comparison of desensitization rates across constructs. I also report the time constant of current decay (τ) for mutants where the fits met the reliability criteria established in Chapter 2, while for mutants whose decay was too slow to be reliably estimated, τ is reported as > 100 s. The extent of desensitization (%Des) at the end of a 1-minute application of agonist is also calculated to allow for quantitative comparisons between mutants.

4.2 Results

4.2.1 The Trp224-Arg301 cation-π interaction stabilizes a slow-desensitizing phenotype in ELIC

As noted, previous studies have suggested that the structure and/or dynamics of M4 are closely linked to the rates of desensitization in ELIC. Trp224 on M1 and Arg301 on M4 in the W-R-P motif are positioned with side chains within distance for a favorable cation-π interaction. Trp-Arg pairs are among the most prevalent and structurally conserved cation-π interactions in proteins (Gallivan & Dougherty, 1999). A strong cation-π interaction could enhance M4-M1 interactions, which in turn could limit M4 dynamics and/or stabilize a preferred orientation of M4 relative to M1, both of which would slow ELIC desensitization, although these two possibilities cannot be distinguished from TEVC measurements alone.

To further test the hypothesis that a cation-π interaction between these residues influences desensitization, I first examined in more detail the desensitization rates of the single Ala mutations W224A and R301A characterized in Chapter 3. WT ELIC had a slow-desensitizing phenotype, with desensitization too slow to give a reliable estimate of τ (reported as > 100 s) and a %Des of 16 ± 11% at 10 mM cysteamine after a 1-min application (**Table *4-1***). Both Ala mutants substantially accelerated desensitization, with τ values of 36 ± 2 s for W224A and 26 ± 2 s for R301A, and %Des values of 38 ± 2% and 66 ± 3%, corresponding to approximately 2- and 4-fold increases in %Des relative to WT, respectively (**Table *4-1***).

I next generated the double mutant W224A + R301A on the same background to ask whether the two residues act independently or through a shared interaction (**Figure *4-1***, **Table *4-1***). The double mutant had no measurable effect on EC_{50} (0.85 ± 0.23 mM) but substantially accelerated desensitization, with a τ of 25 ± 7 s and a %Des of 83 ± 3%, corresponding to an approximately 5-fold increase in %Des relative to WT. If Trp224 and Arg301 acted through

different interactions, mutating both residues should have accelerated desensitization more than mutating either one alone. The τ of the double mutant was instead closer to that of R301A and not faster than either single mutant, which indicates that the two residues are coupled and that mutating either residue breaks the interaction. This is consistent with the single Trp224-Arg301 cation-π interaction proposed at the M4-M1 interface.

To further test the role of this interaction, I generated the swap mutant W224R + R301W, which restores the cation-π interaction in an inverted geometry by placing Trp on M4 and Arg on M1. The swap mutant had no measurable effect on EC_{50} (0.80 ± 0.15 mM) and largely restored the slow-desensitizing phenotype, with desensitization too slow to give a reliable estimate of τ (reported as > 100 s), like WT ELIC, and a %Des of 30 ± 7% (**Figure *4-1***,**Table *4-1***). The recovery of slow desensitization, despite the inverted geometry of the cation-π pair, supports the role of the Trp-Arg cation-π interaction at this position in stabilizing the slow-desensitizing phenotype in ELIC.

To test whether the chemistry of the cation-π interaction is specifically required, or whether any stabilizing electrostatic interaction at this position is sufficient, I generated the W224D mutant. This substitution introduces the possibility of a salt bridge between Asp224 on M1 and Arg301 on M4, which differs in chemistry from the cation-π interaction but maintains a stabilizing electrostatic interaction at the same position. The W224D mutant had no measurable effect on EC_{50} (0.74 ± 0.23 mM) and showed a slow-desensitizing phenotype, with a τ too slow to be reliably estimated (> 100 s) (**Table *4-1***, Appendix). The slow desensitization of the W224D mutant indicates that the chemistry of the cation-π interaction is not specifically required, and that a stabilizing electrostatic interaction between M1 and M4 at this position is sufficient to maintain the slow-desensitizing phenotype.

Figure 4-1 The cation-π interaction at the W-R-P motif modulates ELIC desensitization. (**a-c)**. Structural representation of the lipid-binding site in ELIC: **a.** WT (light grey), **b.** W224A + R301A (firebrick red), and **c.** W224R + R301W (slate blue). Point mutations were created using ChimeraX. Residues are shown in sticks (carbon) with helices in cartoon. **(d-f)** Whole-cell TEVC recordings from oocytes expressing **d.** WT , **e.** W224A+R301A, and **f.** W224R + R301W ELIC. Horizontal bars above each trace represent the time the indicated concentration of agonist was exposed to the oocyte. **g**. Dose-response curves (normalized current (I/I_{max}) versus ligand concentration) for ELIC WT and mutants, with the number (n) of averaged traces. Error bars represent S.D. **h.** Peak-scaled membrane currents elicited by 1-minute application of 10 mM cysteamine for ELIC WT and mutants. The error bars in gray represent the standard deviation (S.D.) from at least 3 independent measurements ($n \geq 3$).

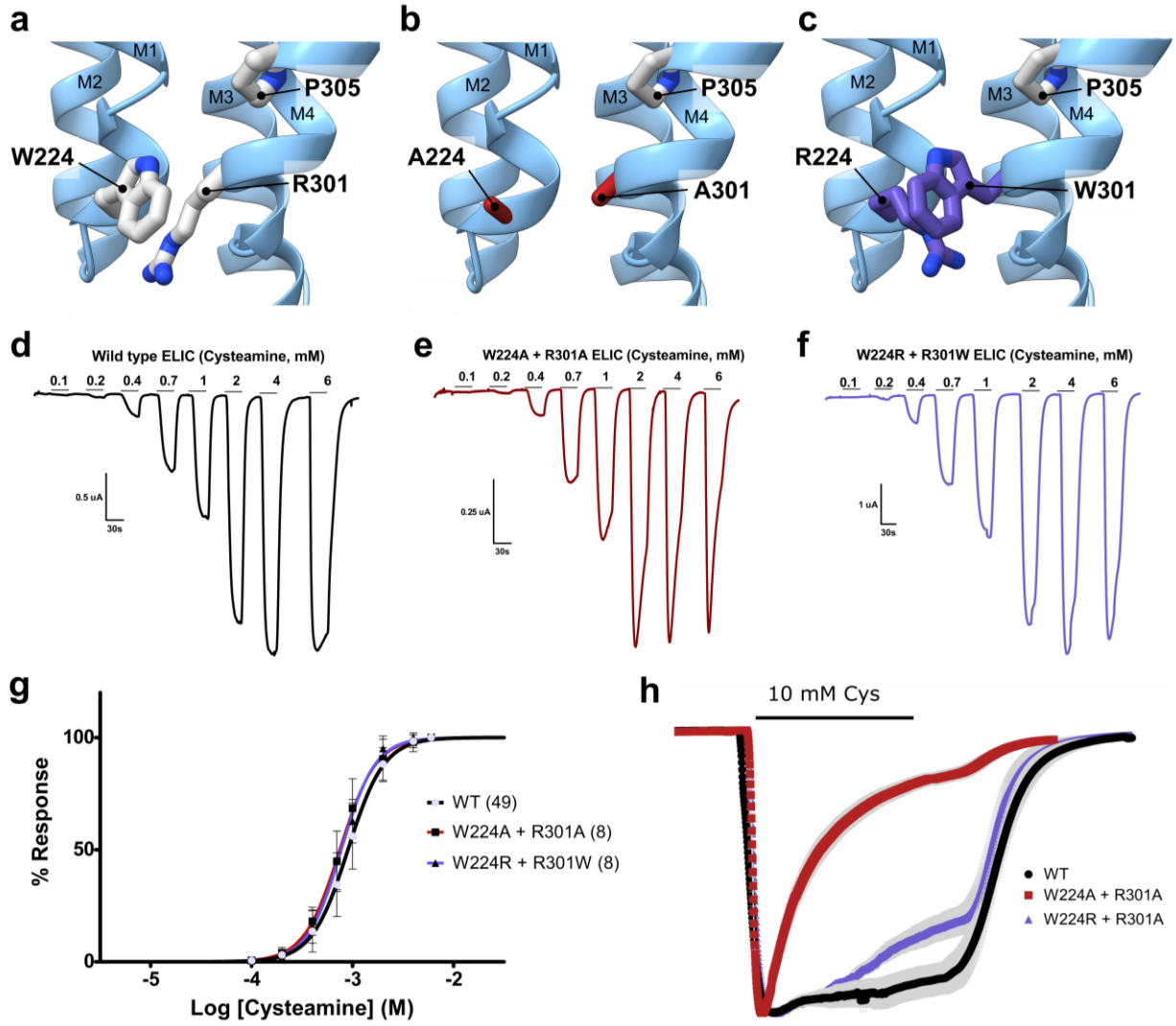
a
M1
M2
M3
M4
P305
W224
R301
b
M1
M2
M3
M4
P305
A224
A301
c
M1
M2
M3
M4
P305
R224
W301
d
Wild type ELIC (Cysteamine, mM)
0.1 0.2 0.4 0.7 1 2 4 6
0.5 uA
30s
e
W224A + R301A ELIC (Cysteamine, mM)
0.1 0.2 0.4 0.7 1 2 4 6
0.25 uA
30s
f
W224R + R301W ELIC (Cysteamine, mM)
0.1 0.2 0.4 0.7 1 2 4 6
1 uA
30s
g
% Response
100
50
0
-5
-4
-3
-2
Log [Cysteamine] (M)
WT (49)
W224A + R301A (8)
W224R + R301W (8)
h
10 mM Cys
WT
W224A + R301A
W224R + R301A

4.2.2 Side-chain substitutions at the Trp224-Arg301 cation-π pair influence ELIC desensitization

To examine in more detail how the chemistry of the Trp224-Arg301 interaction influences ELIC desensitization, I generated a series of substitutions at each position. At Trp224, I introduced Phe (W224F) and Tyr (W224Y), which both retain aromaticity but differ in their cation-π character with Arg in the same environment, with Trp > Phe > Tyr in cation-π strength (Gallivan & Dougherty, 1999). At Arg301, I introduced Lys (R301K), which preserves the positive charge on M4 but differs from Arg in its cation-π character with Trp than Arg does in the same environment (Gallivan & Dougherty, 1999). These substitutions change the chemistry of the interaction at this position without removing it, and tests whether each substitution preserves slow desensitizing phenotype in ELIC.

W224F showed an approximately 4-fold gain-of-function in EC_{50} (0.26 ± 0.01 mM) and preserved slow desensitization, with a slow current decay that prevented a reliable estimate of τ (> 100 s) and a %Des of 20 ± 3%, similar to WT (**Table 4-1, Figure 4-2**). This suggests that Phe, despite lacking the indole nitrogen of Trp, retains sufficient electrostatic and aromatic character to support a favorable cation-π interaction with Arg301. R301K had no measurable effect on EC_{50} (0.69 ± 0.16 mM) with desensitization too slow to give a reliable estimate of τ (> 100 s), suggesting that the primary amine of Lys retains sufficient electrostatic character to support a WT-like cation-π interaction with Trp224 (**Table 4-1, Appendix**).

In contrast, W224Y had a WT-like EC50 (0.73 ± 0.13 mM) but resulted in much faster desensitization, with a τ of 47 ± 10 s and a %Des of 36 ± 8%, similar to the W224A mutation *(***Table 4-1, Figure 4-2***).* The hydroxyl group of Tyr possibly alters the electron distribution of the aromatic ring and may disrupt the geometry of the cation-π interaction with Arg301, either by reducing the effective π-electron density or through steric effects on local packing.

These observations suggest that slow desensitization is preserved when an electrostatic interaction between M1 and M4 is maintained and that the differences in residue geometry and side-chain chemistry, such as the hydroxyl group in Tyr, may also contribute to ELIC desensitization rates.

Figure 4-2 The side chain chemistry of the cation-π interaction at the W-R-P motif influences ELIC desensitization rates

(**a-c)**. Structural representation of the lipid-binding site in ELIC: **a.** W224A (red), **b.** W224Y (salmon), and **c.** W224F (brown). Point mutations were created using ChimeraX. Residues are shown in sticks with helices in cartoon. (carbon). **(d-f)** Whole-cell TEVC recordings from oocytes expressing **d.** W224A, **e.** W224Y, and **f.** W224F ELIC. Horizontal bars above each trace represent the time the indicated concentration of agonist was exposed to the oocyte. **g**. Dose-response curves (normalized current (I/I_{max}) versus ligand concentration) for ELIC WT and mutants, with the number (n) of averaged traces. Error bars represent S.D. **h.** Peak-scaled membrane currents elicited by 1-minute application of 10 mM cysteamine for ELIC WT and mutants. The error bars in gray represent the standard deviation (S.D.) from at least 3 independent measurements ($n \geq 3$).

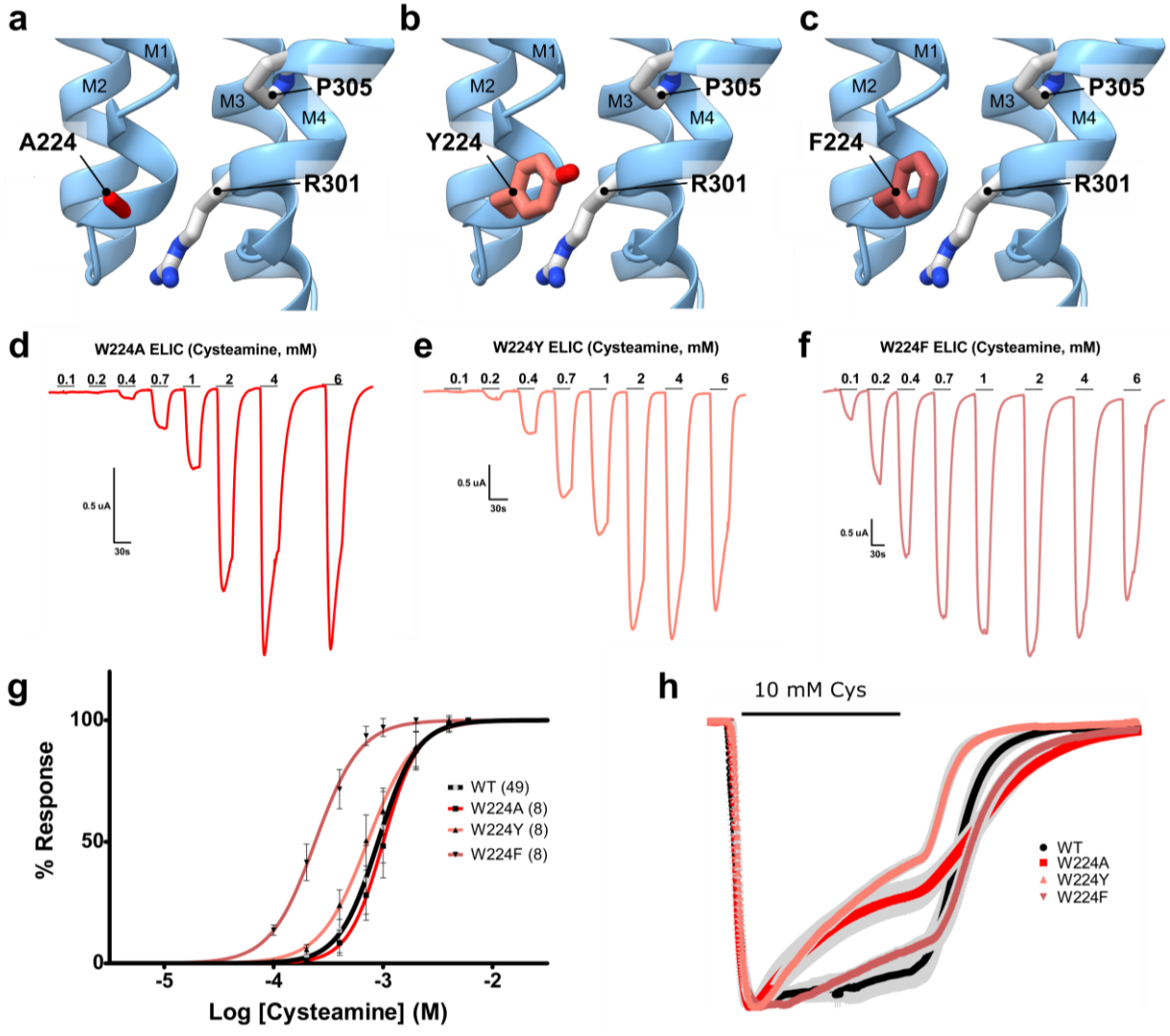
a
M1
M2
M3
M4
P305
A224
R301
b
M1
M2
M3
M4
P305
Y224
R301
c
M1
M2
M3
M4
P305
F224
R301
d
W224A ELIC (Cysteamine, mM)
0.1 0.2 0.4 0.7 1 2 4 6
0.5 uA
30s
e
W224Y ELIC (Cysteamine, mM)
0.1 0.2 0.4 0.7 1 2 4 6
0.5 uA
30s
f
W224F ELIC (Cysteamine, mM)
0.1 0.2 0.4 0.7 1 2 4 6
0.5 uA
30s
g
% Response
100
50
0
-5
-4
-3
-2
Log [Cysteamine] (M)
WT (49)
W224A (8)
W224Y (8)
W224F (8)
h
10 mM Cys
WT
W224A
W224Y
W224F

4.2.3 Aromatic additions at the M4-M1/M3 interface restore ELIC slow desensitization

The Trp224-Arg301 cation-π mutants suggested that disrupting interactions at the M4-M1/M3 interface accelerates ELIC desensitization. To test this further, I examined whether strengthening interactions at this interface can compensate for disruptions elsewhere along the M4 helix. I introduced three aromatic substitutions at the C-terminus of M4 (V261Y, G319F, and I320F; the 3Aro mutant), which were predicted from structural modelling to enhance interactions between M4 and the surrounding M1 and M3 helices (Carswell, Sun, et al., 2015). If interactions at the M4-M1/M3 interface modulate ELIC desensitization through their effects on M4 structure or dynamics, then strengthening interactions at the C-terminus of M4 should compensate for mutations that weaken interactions at the W-R-P motif and slow desensitization in those backgrounds.

The 3Aro mutant alone gave an approximately 5-fold gain-of-function in EC_{50} (0.18 ± 0.02 mM), with desensitization too slow to give a reliable estimate of τ (> 100 s) and no detectable current decay over the 1-min agonist application (**Table 4-1,Figure 4-3**). The gain-of-function in EC_{50} was previously characterized in (Carswell, Hénault, et al., 2015), where the 3Aro substitutions were suggested to enhance interactions between M4 and M1-M3. The slow-desensitizing phenotype of 3Aro alone is consistent with the prediction that strengthening interactions at the M4-M1/M3 interface should preserve, or further stabilize, the slow desensitizing phenotype of WT ELIC.

To test whether the 3Aro background compensates for disruptions to the Trp224-Arg301 cation-π interaction, I introduced the W224A and R301A single mutations on the 3Aro background. The 3Aro + W224A mutant had a WT-like EC_{50} (0.97 ± 0.10 mM) and a %Des of 34 ± 3%, similar to the 38 ± 2% observed for the W224A single mutant (**Figure 4-3, Table 4-1**). The decay of 3Aro + W224A could not be reliably fit to a single exponential within the

recording window, so τ is not reported. The 3Aro + R301A mutant showed an approximately 2-fold gain-of-function in EC_{50} (0.45 ± 0.14 mM), with desensitization too slow to give a reliable estimate of τ (> 100 s) and no detectable current decay over the 1-min agonist application, compared to a τ of 26 ± 2 s and a %Des of 66 ± 3% for the R301A single mutant alone *(***Table 4-1,Figure 4-*3)***.* The 3Aro background therefore fully restored the slow-desensitizing phenotype in R301A, but in W224A slowed the rate of decay sufficiently to prevent a reliable τ fit, while the %Des remained similar to W224A alone. This supports the hypothesis that strengthening interactions at the C-terminus of M4 can compensate for disruptions to the Trp224-Arg301 cation-π interaction.

To test whether the 3Aro background can also compensate for disruption of the M4 kink, I introduced the P305A mutation on the 3Aro background. The 3Aro + P305A mutant showed an approximately 3.5-fold gain-of-function in EC_{50} (0.26 ± 0.01 mM), similar to P305A alone, and slower desensitization rates, with a τ of 29 ± 4.5 s and a %Des of 75 ± 8%, compared to a τ of 4.4 ± 1.5 s and a %Des of 95 ± 3% for the P305A mutant *(***Table 4-1,Figure 4-*3)***.* Although the τ slowed approximately 7-fold and the %Des was reduced compared to P305A alone, the τ remained measurable and the 3Aro + P305A mutant continued to desensitize substantially faster than WT. This indicates that strengthening interactions at the C-terminus of M4 cannot fully compensate for loss of the Pro305 kink, in contrast to the slower desensitizing rates restored with the cation-π Ala mutants.

To test whether the 3Aro background can compensate for the simultaneous loss of both residues of the Trp224-Arg301 cation-π interaction, I introduced the double mutation W224A + R301A on the 3Aro background. The 3Aro + W224A + R301A mutant had no measurable effect on EC_{50} (0.57 ± 0.01 mM) and slowed desensitization, with a τ of 40 ± 6 s and a %Des of 31 ± 5%, compared to a τ of 25 ± 7 s and a %Des of 83 ± 3% for the W224A + R301A double mutant alone *(***Table 4-1,Figure 4-*3)***.* The slow-desensitizing phenotype was therefore

partially restored on the 3Aro background, with the %Des reduced approximately 3-fold compared to the double mutant alone, although the τ remained measurable and the slow-desensitizing phenotype was not as restored as for the single Ala mutants. This indicates that strengthening interactions at the C-terminus of M4 can partially compensate for the simultaneous loss of both residues of the cation-π interaction, but cannot fully restore the slow-desensitizing phenotype seen in WT.

Together, the 3Aro background restored the slow-desensitizing phenotype to varying extents across the W-R-P motif mutants. Slow desensitization was fully restored in R301A, partially restored in the W224A + R301A double mutant, and only modestly restored in W224A and in P305A. These results show that interactions at the M4-M1/M3 interface modulate ELIC desensitization. The Trp224-Arg301 cation-π interaction and the Pro305 kink are both essential to slow desensitization, with the kink contributing through a structurally distinct mechanism that is partially restored by strengthening other interactions at the M4-M1/M3 interface.

Figure 4-3 Aromatic additions at the M4-M1/M3 interface restore ELIC slow desensitization.

(**a**) Structural representation of the ELIC transmembrane domain (cyan) showing a single subunit, with the boxed regions highlighting the 3Aro substitutions at the C-terminus of M4 (solid box) and the W-R-P motif (dashed box). (**b, c**) Zoomed-in views of the 3Aro region in **b**. (Y261 on M3, F318 and F319 on M4, orange sticks) and the W-R-P motif in c. (W224 on M1, R301 on M4, and P305 on M4). Residues are shown in sticks with helices in cartoon. (**d**) Dose-response curves (normalized current (I/I_{max}) versus cysteamine concentration) for ELIC WT, 3Aro, 3Aro+W224A, 3Aro+R301A, and 3Aro+P305A. Error bars represent S.D. (**e-g**) Peak-scaled membrane currents elicited by 1-minute application of 10 mM cysteamine for ELIC WT, W224A, 3Aro, and 3Aro+W224A in **e.**; for ELIC WT, R301A, 3Aro, and 3Aro+R301A in **f.**; and for ELIC WT, P305A, 3Aro, and 3Aro+P305A in **g.** Shaded regions in grey represent S.D. from at least 3 independent measurements ($n \geq 3$).

a.

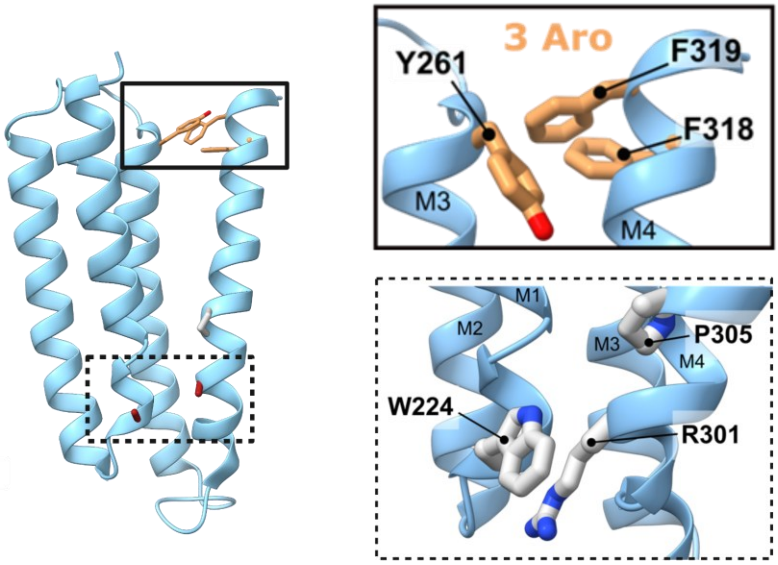
3 Aro
Y261
F319
F318
M3
M4
M1
M2
M3
P305
M4
W224
R301

b.

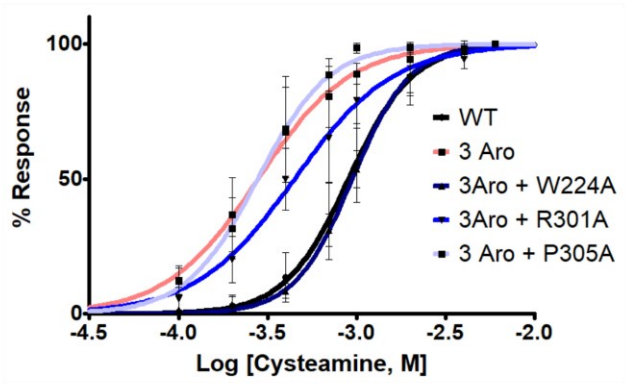
100
50
0
% Response
-4.5
-4.0
-3.5
-3.0
-2.5
-2.0
Log [Cysteamine, M]
WT
3 Aro
3Aro + W224A
3Aro + R301A
3 Aro + P305A

c.

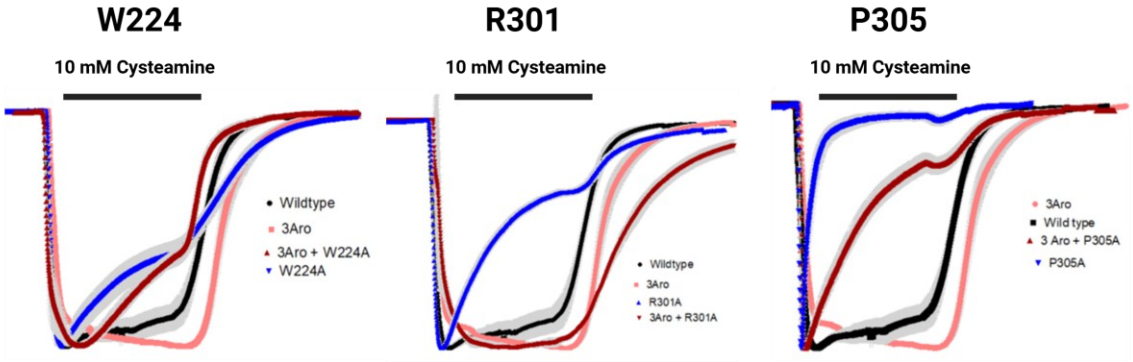
W224
10 mM Cysteamine
Wildtype
3Aro
3Aro + W224A
W224A
R301
10 mM Cysteamine
Wildtype
3Aro
R301A
3Aro + R301A
P305
10 mM Cysteamine
3Aro
Wild type
3 Aro + P305A
P305A

Figure 4-4 Aromatic additions at the M4-M1/M3 interface restores ELIC slow desensitization rates in the absence of the cation-π interaction

Structural representation of residues near the C-terminus: a. ELIC wildtype (solid outline) (top) and b. 3Aro ELIC with added aromatic residues (bottom), shown with the W224A + R301A mutant (dashed outline) on either the wildtype or the 3Aro backbone. Peak-scaled membrane currents elicited by 1-minute application of 10 mM cysteamine for W224A + R301A mutant on the a. wildtype backbone, and b. 3Aro backbone. The error bars in gray represent the standard deviation (S.D.) from at least 3 independent measurements ($n \geq 3$).

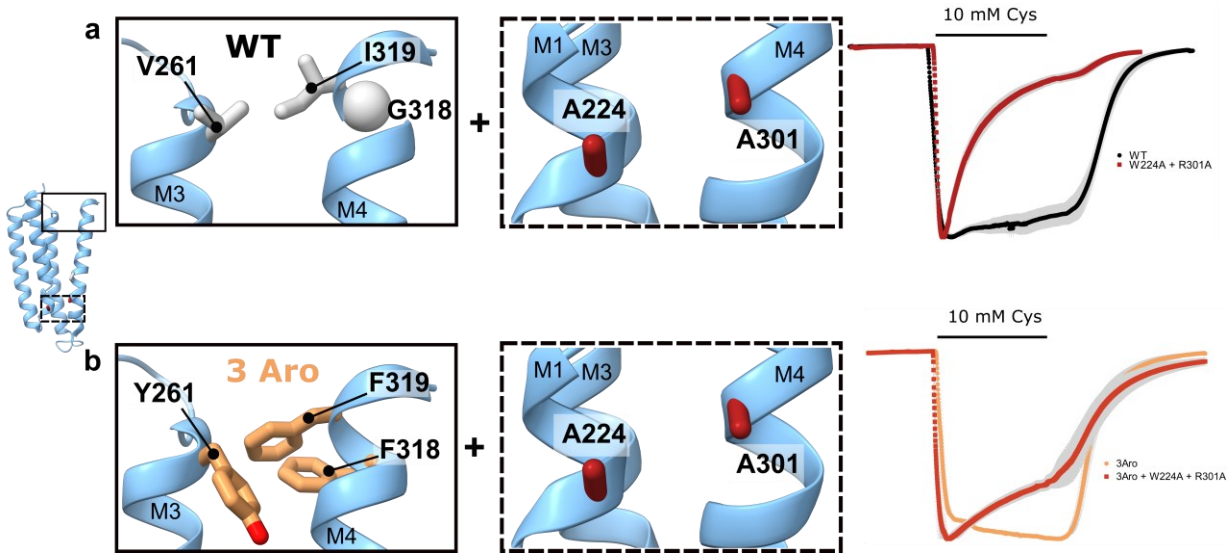
a
WT
V261
I319
G318
M3
M4
+
M1
M3
M4
A224
A301
10 mM Cys
WT
W224A + R301A
b
3 Aro
Y261
F319
F318
M3
M4
+
M1
M3
M4
A224
A301
10 mM Cys
3Aro
3Aro + W224A + R301A

Table 4-1 Effects of mutations at the M4-M1/M3 interface on ELIC function.

Mutant	EC_{50} (Cysteamine, mM)	Hill slope	n	τ (s)*	%Des*	n
WT	0.96 ± 0.23	2.58 ± 0.79	58	> 100	16 ± 11	7
Single Ala mutations at the cation-π pair						
W224A	1.06 ± 0.21	2.84 ± 0.60	8	36 ± 2	38 ± 2 [a]	4
R301A	0.46 ± 0.12	2.64 ± 0.98	8	26 ± 2	66 ± 3 [a]	4
Double Ala mutation						
W224A + R301A	0.85 ± 0.23	2.50 ± 0.58	8	25 ± 7	83 ± 3 [a]	5
Cation-π swap						
W224R + R301W	0.80 ± 0.15	2.70 ± 0.35	8	> 100	30 ± 7 [c]	4
Modulating cation-π strength						
W224F	0.26 ± 0.01 [a]	2.01 ± 0.34	8	> 100	20 ± 3	8
W224Y	0.73 ± 0.13 [b]	1.88 ± 0.29	8	47 ± 10	36 ± 8 [a]	5
R301K	0.69 ± 0.16 [c]	2.60 ± 0.53	8	> 100	N/A	3
Stabilizing electrostatic interaction (salt bridge)						
W224D	0.74 ± 0.23	1.39 ± 0.43	8	> 100	N/A	3
Aromatic additions at the M4-M1/M3 interface (3Aro)						
3 Aro	0.18 ± 0.02	2.60 ± 0.16	9	> 100	N/A	3
3 Aro + W224A	0.97 ± 0.10 [a]	2.74 ± 0.37	7	> 100	34 ± 3 [b]	3
3 Aro + R301A	0.45 ± 0.14 [a]	1.39 ± 0.36	6	> 100	N/A	3
3 Aro + W224A + R301A	0.57 ± 0.01 [a]	2.64 ± 0.11	8	40 ± 6	31 ± 5 [c]	4
3 Aro + P305A	0.26 ± 0.01 [a]	1.10 ± 0.40	6	29 ± 4.5	75 ± 8 [a]	7

[a] $p < 0.001$ relative to wild type via one-way ANOVA followed by Dunnett's post hoc test. [b] $p < 0.01$ relative to wild type via one-way ANOVA followed by Dunnett's post hoc test. [c] $p < 0.05$ relative to wild type via one-way ANOVA followed by Dunnett's post hoc test. *Data from 1-minute application of 10 mM cysteamine (~10-fold EC_{50}). τ > 100 s indicates that the decay was too slow to be reliably estimated within the recording window using the criteria established in Chapter 2. Values are reported as mean ± standard deviation. N/A: no detectable current decay over the 1-min agonist application.

4.2.4 Mutations at the M1-M3 interface adjacent to the Pro305 kink accelerates ELIC desensitization

The cation-π and 3Aro mutants showed that interactions at the M4-M1/M3 interface modulate ELIC desensitization. I next turned to the second goal of this chapter which is to begin to address how interactions at this interface ultimately influence desensitization. Here I focused on residues adjacent to the Pro305 kink, which are positioned close to the proposed L9' gate (Dalal et al., 2025). W220 on M1 and S271 on M3 lie at this position with their side chains positioned to form a hydrogen bond at the M1-M3 interface (**Figure *4-5***). I hypothesized that interactions at this region contribute to slow ELIC desensitization, and that disrupting them would alter desensitization. Given the proximity of W220 and S271 to the proposed L9' gate, an effect on desensitization would be consistent with a link between this region and the L9' gate. To test this, I introduced Ala substitutions at W220 and S271, individually and in combination (**Figure *4-5***).

W220A had no measurable effect on EC_{50} (0.91 ± 0.26 mM) and accelerated desensitization, with a τ of 24 ± 7 s and a %Des of 64 ± 2%, approximately 4-fold higher than WT (**Figure *4-5*,Table *4-2***). S271A had a WT-like EC_{50} (0.82 ± 0.05 mM) and similarly accelerated desensitization, with a τ of 23 ± 4 s and a %Des of 56 ± 4%, approximately 3.5-fold higher than WT (**Figure *4-5*,Table *4-2***). The two single mutants therefore gave similar phenotypes, suggesting that W220 and S271 contribute to slow desensitization through a shared interaction at the M1-M3 interface. The double mutant W220A + S271A had no measurable effect on EC_{50} (1.18 ± 0.01 mM) and accelerated desensitization, with a τ of 12 ± 5 s and a %Des of 86 ± 9%, approximately 5-fold higher than WT and faster than either single mutant alone (**Figure *4-5*,Table *4-2***). The double mutant accelerated desensitization beyond what was observed in either single mutant, indicating that the contribution of W220 and S271 is not limited to a shared H-bond interaction. This additional effect could reflect individual

contributions from each residue, or the loss of broader M4-M1/M3 packing in this region when both side chains are removed simultaneously.

4.2.5 Side-chain mutations at the M3-M4 linker preserve slow ELIC desensitization

I next turned to residues on the M3-M4 linker, which lie close to the cytoplasmic end of M2 where the -2' gate is proposed in anion-selective pLGICs (Gielen et al., 2015a; Gielen & Corringer, 2018a). Spectroscopic work also suggested that the desensitization gate in ELIC overlaps with the anion-selective -2' gate (Kinde et al., 2015). The Δ8 ELIC mutant, which lacks the eight C-terminal residues of M4 and accelerates desensitization, shows increased dynamics in this region of the receptor (Hénault et al., 2019), and the M3-M4 linker is positioned to couple M4 to the M2 helix through this region. I hypothesized that interactions involving residues on the M3-M4 linker contribute to slow desensitization, and that disrupting them would alter desensitization. Given the proximity of the linker to the proposed -2' gate, an effect on desensitization would be consistent with a link between the linker region and the -2' gate. To test this, I introduced Ala substitutions at three clusters of residues spanning the M3-M4 linker: R286 + Q287, N289 + G290 + V291, and E292 + D293 + D294 (**Figure *4-5*,Table *4-2***).

All three clusters of M3-M4 linker mutations preserved the slow-desensitizing phenotype. R286A + Q287A had a WT-like EC_{50} (0.81 ± 0.24 mM), with desensitization was too slow to give a reliable estimate of τ (> 100 s) and no detectable current decay over the 1-min agonist application (**Figure *4-5*,Table *4-2***). N289A + G290A + V291A and E292A + D293A + D294A both showed approximately 2-fold gain-of-function in EC_{50} (0.42 ± 0.16 mM and 0.46 ± 0.19 mM, respectively) and similarly preserved the slow-desensitizing phenotype, with desensitization was too slow to give a reliable estimate of τ (> 100 s) and no detectable current decay over the 1-min agonist application (**Figure *4-5*,Table *4-2***).

The Ala substitutions at these clusters of M3-M4 linker residues preserved the slow-desensitizing phenotype, indicating that the side chains of the residues tested are not major contributors to the regulation of slow ELIC desensitization. This does not exclude a role for main-chain interactions, but the side chains tested do not appear to have a role in modulating ELIC desensitization.

I also tested a putative salt bridge between E226 on M1-M2 linker and H284 on the M3-M4 linker, with the rationale that disrupting this electrostatic interaction could alter desensitization. The proximity of H285 to E226 raises the additional possibility of a bifurcated interaction involving both H284 and H285. E226A had a modest gain-of-function in EC_{50} (0.46 ± 0.16 mM), with desensitization too slow to give a reliable estimate of τ (> 100 s) and no detectable current decay over the 1-min agonist application (**Table *4-2***). H284A and the combinations E226A + H284A and E226A + H284A + H285A all failed to produce measurable agonist-induced currents (**Table *4-2***). The loss of currents in all H284-containing constructs suggests that H284 is essential for ELIC channel function, likely through a role in assembly, surface expression, and/or channel gating. The contribution of the proposed E226-H284 salt bridge to desensitization could therefore not be assessed.

Figure 4-5 Mutations at the M1-M3 interface near the Pro305 kink accelerate ELIC desensitization, while side-chain mutations at the M3-M4 linker preserve slow desensitization.

(a) Structural representation of the ELIC transmembrane domain showing M1, M3, and M4, with the red box outlining the M3-M4 linker region. (**b, c**) Zoomed-in views of the M1-M3 interface adjacent to the Pro305 kink in **b**. (W220, S271, P305) and the M3-M4 linker in **c.** (H284, H285, N289 to D294). Residues are shown in sticks with helices in cartoon. (**d, e**) Dose-response curves (normalized current (I/Imax) versus cysteamine concentration) for ELIC WT and M1-M3 interface mutants in **d.** and M3-M4 linker mutants in e. Error bars represent S.D. (**f, g**) Peak-scaled membrane currents elicited by 1-minute application of 10 mM cysteamine for ELIC WT and M1-M3 interface mutants in **f.** and M3-M4 linker mutants in **g**. Shaded regions in grey represent S.D. from at least 3 independent measurements ($n \geq 3$)

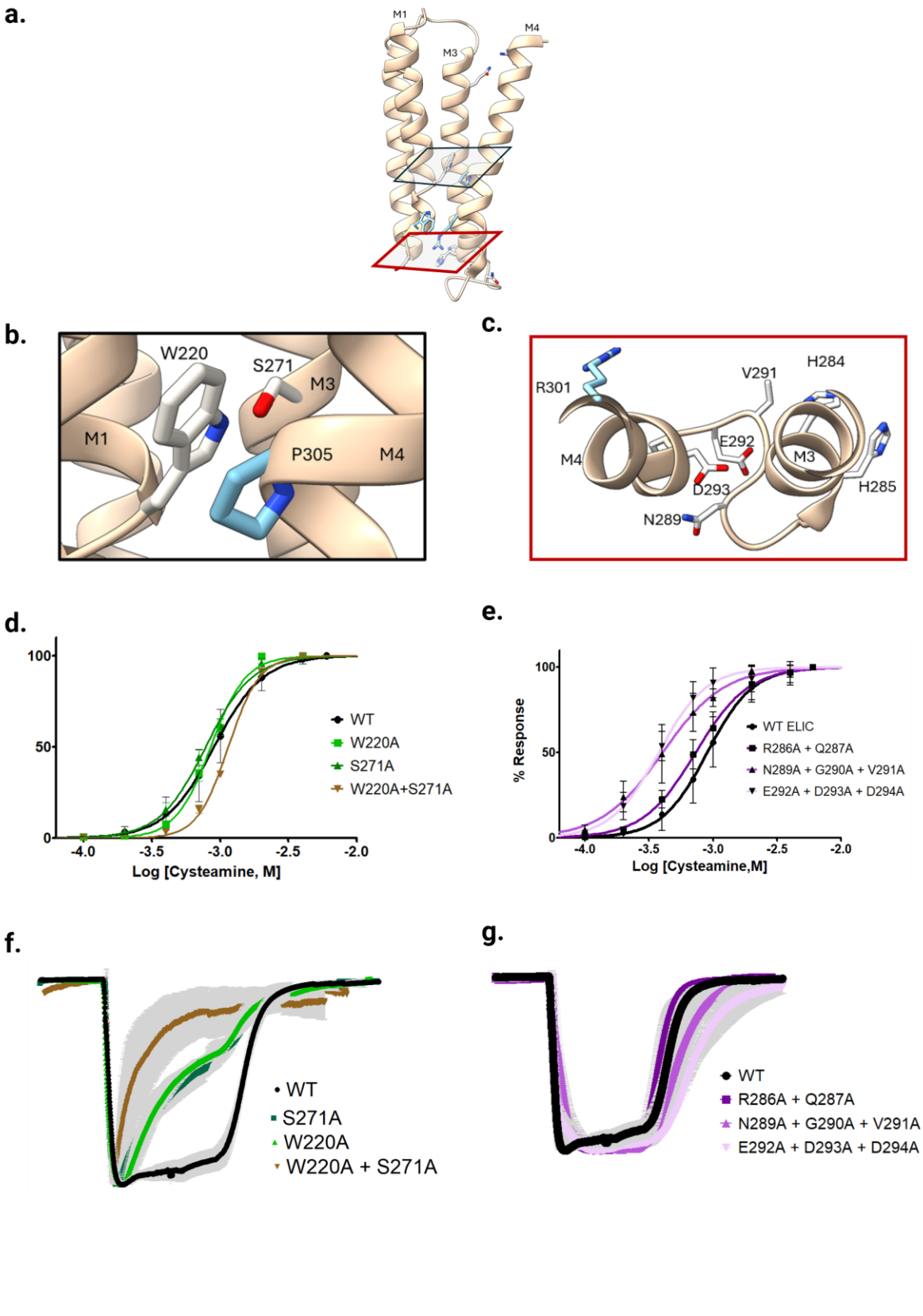
a.
M1
M3
M4
b.
W220
S271
M3
M1
P305
M4
c.
R301
V291
H284
E292
M4
M3
D293
H285
N289
d.
100
50
0
-4.0
-3.5
-3.0
-2.5
-2.0
Log [Cysteamine, M]
WT
W220A
S271A
W220A+S271A
e.
% Response
100
50
0
-4.0
-3.5
-3.0
-2.5
-2.0
Log [Cysteamine,M]
WT ELIC
R286A + Q287A
N289A + G290A + V291A
E292A + D293A + D294A
f.
WT
S271A
W220A
W220A + S271A
g.
WT
R286A + Q287A
N289A + G290A + V291A
E292A + D293A + D294A

Table 4-2 Effects of mutations at the M1-M3 interface and the M3-M4 linker on ELIC function.

Mutant	EC_{50} (Cysteamine, mM)	Hill slope	n	τ (s)*	%Des*	n
WT	0.96 ± 0.23	2.58 ± 0.79	58	> 100	16 ± 11	7
M1-M3 interface adjacent to the Pro305 kink						
W220A	0.91 ± 0.26 [d]	2.96 ± 0.20	8	24 ± 7	64 ± 2 [a]	3
S271A	0.82 ± 0.05 [d]	2.39 ± 0.31	7	23 ± 4	56 ± 4 [a]	3
W220A + S271A	1.18 ± 0.01 [b]	3.47 ± 0.28	8	12 ± 5	86 ± 9 [a]	4
M3-M4 linker mutations						
R286A + Q287A	0.81 ± 0.24	2.04 ± 0.28	6	> 100	N/A	2
N289A + G290A + V291A	0.42 ± 0.16 [a]	2.16 ± 0.39	6	> 100	N/A	3
E292A + D293A + D294A	0.46 ± 0.19 [a]	2.43 ± 0.68	7	> 100	N/A	2
M1-linker putative salt bridge						
E226A	0.46 ± 0.16 [a]	1.91 ± 0.55	6	> 100	N/A	4
H284A	NC	-	5	-	-	-
E226A + H284A	NC	-	5	-	-	-
E226A + H284A + H285A	NC	-	5	-	-	-

[a] $p < 0.001$ relative to wild type via one-way ANOVA followed by Dunnett's post hoc test. [b] $p < 0.01$ relative to wild type via one-way ANOVA followed by Dunnett's post hoc test. [d] Data from Therien & Baenziger 2017 *Data from 1-minute application of 10 mM cysteamine (~10-fold EC_{50}). $\tau > 100$ s indicates that the decay was too slow to be reliably estimated within the recording window using the criteria established in Chapter 2. Values are reported as mean ± standard deviation. N/A: no detectable current decay over the 1-min agonist application. NC: no measurable currents.

4.3 Discussion

In this chapter, I tested how interactions at the M4-M1/M3 interface contribute to the modulation of ELIC desensitization. The data supports two main findings. First, the strength of interactions at the M4-M1/M3 interface influence the rate of ELIC desensitization, providing direct functional evidence for the role of this interface in modulating desensitization. Second, this interface contains several distinct features that contribute to ELIC slow desensitization, including the Trp224-Arg301 cation-π interaction at the W-R-P motif and the Pro305 kink. Mutations at the M1-M3 interface adjacent to the Pro305 kink also accelerated desensitization, while mutations to the side chains of the M3-M4 linker did not.

Prior to this work, the link between M4 structure or dynamics and ELIC desensitization was supported by indirect evidence. The Δ8 ELIC crystal structure lacks density for the M4 helix, which has been interpreted as evidence for increased M4 mobility, but this could also reflect mobility introduced by detergent-solubilization of the protein rather than an M4 characteristic (Hénault et al., 2019). The P305A mutation accelerates desensitization and is expected to favour an unkinked M4 conformation, but its phenotype could reflect altered M4 conformation rather than altered M4 dynamics. The cation-π and 3 Aro mutagenesis experiments presented here provide more direct evidence to role of the M4 interactions with its neighboring helices M1 and M3. Disrupting this interaction with single Ala mutations accelerated desensitization, restoring it in inverted geometry through the W224R + R301W swap restored the slow-desensitizing phenotype, and replacing the cation-π with a salt bridge through W224D also maintained slow desensitization. These results show that the strength of the M4-M1 interaction contributes to the rate of desensitization, independent of the electrostatic interaction type. The 3Aro experiment further supports this conclusion. Strengthening interactions at the C-terminus of M4 through aromatic substitutions, which were previously characterized in the ELIC (Carswell, Hénault, et al., 2015), restored slow desensitization in the

W224A and R301A backgrounds. Together, these experiments support a model in which stabilizing interactions at the M4-M1/M3 interface favours slow ELIC desensitization rates.

The M4-M1/M3 interface have different kinds of features that contribute to slow desensitization. The Trp224-Arg301 cation-π pair acts as a coupled interaction. The single and double mutants produced similar phenotypes, with the τ of the W224A + R301A double mutant is indistinguishable from R301A alone. This is consistent with the two residues acting through one shared interaction at the M4-M1 interface. The W220-S271 interaction at the M1-M3, however, interface behaves differently. The single W220A and S271A mutants gave similar phenotypes, consistent with both residues participating in a shared interaction. The double mutant accelerated desensitization, however, faster than both single mutants, indicating that the contribution of W220 and S271 is not limited to a single shared interaction. This could reflect individual interactions for each residue beyond the shared interaction, or the loss of broader packing interactions in this region when both side chains are removed. The data here do not distinguish between these possibilities. The Pro305 kink represents a structurally distinct feature, with strengthening of other M4-M1/M3 interactions through the 3Aro substitutions unable to fully compensate for the kink removal. Slow ELIC desensitization is therefore supported by different interactions or features at the M4-M1/M3 interface; a coupled cation-π interaction at the W-R-P motif, interactions at the M1-M3 interface near the Pro-kink, and the Pro305 kink itself.

The Trp224-Arg301 cation-π interaction lies at the inner-leaflet W-R-P pocket where lipid binding has been observed (Hénault et al., 2019; P. Kumar et al., 2021; Tong et al., 2019). The M4 dynamics model proposes that lipid binding at this pocket stabilizes a kinked conformation of M4 and slows desensitization, while disruption of this binding accelerates it (Hénault et al., 2019). The data in this chapter is consistent with this model and identify M4-M1/M3 interactions whose modulation could underlie the lipid-dependent regulation of

desensitization. Lipid acyl chains in the pocket could provide a hydrophobic environment that strengthens the Trp224-Arg301 cation-π interaction or stabilize the broader M4-M1/M3 interface and constrain M4 in its kinked conformation through steric packing in the pocket. These possibilities are not mutually exclusive, and the present data do not distinguish between them.

A second lipid binding site has been identified at the outer-leaflet of the M4-M1/M3 interface, where PG binding stabilizes an open-state in ELIC (Petroff et al., 2022). The 3Aro substitutions lie in the same region of the TMD. The slowing of desensitization observed with the 3Aro substitutions is consistent with stronger interactions in this region stabilizing the open state, paralleling the effect of outer-leaflet PG binding reported by Petroff et al. (2022). The slow phenotype of 3Aro alone could therefore reflect strengthened TMD interactions, altered outer-leaflet lipid interactions, or both.

The slowing of desensitization rates in TEVC reflects the net macroscopic equilibrium between activation and desensitization. The macroscopic current decay rate reflects several underlying transitions at the channel level, as it does not distinguish between a transition from the closed to the open state, a transition from open to the desensitized state, or faster recovery from desensitization. Single-channel recordings would be needed to resolve individual channel openings and provide direct estimates of open probability.

In conclusion, this chapter identifies the M4-M1/M3 interface as a modulator of ELIC desensitization and maps three distinct interactions/features of the interface that contribute to slow desensitization. Direct tests of how lipid binding at the W-R-P pocket and the outer-leaflet site modulate these specific interactions remain an open avenue for future work.

5 Chapter 5 – Conclusion

5.1 Summary of findings

The goal of this thesis was to gain a deeper understanding of how the W-R-P motif and the M4-M1/M3 interface shape pLGIC desensitization. I asked two questions. First, does the conserved W-R-P pocket play a conserved role in modulating desensitization across pLGICs? Second, how do interactions at the W-R-P pocket and along the M4-M1/M3 interface modulate ELIC desensitization? I addressed both questions using TEVC electrophysiology in *Xenopus laevis* oocytes across ELIC, GlyR, and GLIC.

In Chapter 3, I show that the W-R-P pocket plays different roles in modulating desensitization across the three pLGICs, despite the conservation of the motif. In ELIC, mutations across the W-R-P motif and the lining residues of the W-R-P pocket accelerated desensitization, as did Pro-kink shifts and M4 C-terminal deletions. In GlyR, several pocket mutations also accelerated desensitization, but most other M4 perturbations abolished agonist-induced currents. In GLIC, most mutations to the W-R-P motif and the pocket had no measurable effect on desensitization. These results show that conservation of the W-R-P motif does not imply conservation of mechanism. Instead, the functional effect of perturbing this pocket depends on the broader architecture of the M4-M1/M3 interface, particularly the density of aromatic interactions at this interface.

In Chapter 4, I focused on ELIC and showed that the strength of interactions at the M4-M1/M3 interface modulates the rate of ELIC desensitization. Disrupting the Trp224-Arg301 cation-π interaction accelerated desensitization, while restoring or strengthening interactions at this interface, through cation-π substitutions or aromatic additions at the C-terminus of M4, preserved slow desensitization. These results identify three features that support slow

desensitization in ELIC, the Trp224-Arg301 cation-π interaction at the W-R-P motif, an interaction between W220 on M1 and S271 on M3 at the M1-M3 interface adjacent to the Pro305 kink, and the Pro305 kink itself. Together, these data provide direct functional evidence that the M4-M1/M3 interface regulates the rate of ELIC desensitization

These findings advance the understanding of pLGIC desensitization in two main ways. First, they establish direct evidence for a functional link between M4-M1/M3 interactions and the rate of desensitization in ELIC. This adds to the growing picture of M4 as a key regulator of pLGIC function and supports the idea that lipid binding at the W-R-P pocket modulates desensitization through its effects on M4 structure or dynamics. Second, the cross-receptor comparison shows that the same conserved motif can contribute differently to desensitization depending on the broader architecture of the M4-M1/M3 interface.

The work is also relevant to human health. Anion-selective pLGICs, including $GABA_A$Rs and GlyRs, mediate inhibitory neurotransmission in the CNS and are major targets for drugs used in epilepsy, anxiety, and pain management. The W-R-P pocket overlaps with binding sites for neurosteroids, cannabinoids, and other lipidic modulators that shape the function of these receptors in the brain. Understanding how this pocket and the surrounding M4-M1/M3 interface influence desensitization may therefore help guide future studies of lipid-dependent modulation and drug action in inhibitory neurotransmitter receptors.

5.2 Future directions

The data presented in this thesis support a working model in which M4 dynamics or conformation, lipid binding at the W-R-P pocket, and M4-M1/M3 interactions collectively shape ELIC desensitization. The next step is to test this model in systems that can directly measure structure, lipid dependence, and single-channel behavior.

5.2.1 Cryo-EM structures of fast desensitizing ELIC mutants

The current model relies on indirect evidence for M4 structure and/or dynamics. The Δ8 ELIC crystal structure lacks density for the M4 helix (Hénault et al., 2019), and M4 appears in both kinked and unkinked conformations across deposited ELIC structures (Gonzalez-Gutierrez et al., 2012; Zimmermann & Dutzler, 2011). These observations suggest that M4 can adopt different conformations, but they do not show directly how the fast-desensitizing mutants behave in a lipid bilayer.

An important next step is to solve cryo-EM structures of WT ELIC and three fast desensitizing constructs in lipid nanodiscs or liposomes that better recapitulate the lipid environment (Dalal et al., 2024, 2025): Δ8, ΔM4, and P305A. Each construct probes a different aspect of the model. Δ8 tests whether removing the M4 C-terminal produces a more dynamic or differently positioned M4 in a lipid bilayer, beyond what was observed in the original Δ8 crystal structure. P305A tests whether eliminating the kink alters M4 conformation while leaving the lipid binding pocket intact. ΔM4 removes the lipid binding site entirely and tests how the rest of the TMD rearranges in the absence of M4. WT ELIC, solved under the same conditions, would serve as a control for direct comparison.

These structures would help distinguish between two possibilities. If M4 is disordered or shows weaker density in P305A and Δ8, this would support a contribution of M4 dynamics to the fast-desensitizing phenotype. If M4 instead adopts a different but defined position, this would refine the model and point to altered M4 position relative to M1 and M3, rather than dynamics alone, as the key feature. Comparing the region near the proposed desensitization gate across WT and mutant structures would also help determine whether the mutations act through M4, the desensitization gate, or both.

5.2.2 Functional reconstitution of ELIC in single channel planar lipid bilayer recordings

A second direction is to characterize ELIC at the single channel level in defined lipid environments. The lab has the Nanion Orbit 16 planar lipid bilayer system, which uses MECA chips containing 16 microcavities to allow parallel single channel recordings of purified pLGICs reconstituted into bilayers of defined lipid composition.

This goal has three sequential aims. The first is to characterize the functional activity of WT ELIC in the planar lipid bilayer system. I ran some preliminary experiments have shown that asolectin bilayers alone give a flat baseline current, while bilayers reconstituted with ELIC and activated with 10 mM GABA produce clear single channel openings, validating the system for ELIC recordings. Further characterization of WT ELIC in standard lipid compositions will establish baseline values for single channel open probability (p_{open}) and mean cluster duration that can be used to compare against mutant constructs.

The second aim is to compare the single channel activity of fast-desensitizing ELIC mutants to WT in the same lipid environment. Starting with P305A and ΔM4, and extending to W224A, R301A, single channel recordings would test whether the fast-desensitizing phenotype observed in TEVC is reflected in altered p_{open} or open dwell times at the single channel level. P305A is predicted to show a lower p_{open}, consistent with loss of the kinked M4 conformation that the lipid-bound state stabilizes. ΔM4, which removes the lipid binding site entirely, is predicted to show the lowest p_{open}, with no responsiveness to lipid composition.

The third aim is to test how different lipids influence ELIC single channel activity. Reconstituting WT ELIC and the same set of mutants into bilayers of varying composition (pure PC, 9:1 PC:PG, 3:1 PC:PG, and 1:1 PC:PG) would test whether mol% PG modulates p_{open} and whether this modulation is preserved or lost in W-R-P pocket mutants. WT ELIC is

predicted to show a p_{open} that increases with mol% PG, with the highest values at 3:1 and 1:1 PC:PG. If a pocket mutation reduces this PG dependence, this would, indirectly, support a role for that residue in coupling lipid binding to channel function.

5.2.3 Disulfide cross-linked mutants to lock M4 in kinked or unkinked conformations

A third direction is to design ELIC constructs that lock M4 in either a kinked or an unkinked conformation through engineered disulfide bonds and then test desensitization under oxidizing and reducing conditions in TEVC. Preliminary AlphaFold (Jumper et al., 2021) modelling has been used to identify candidate Cys pairs at positions where the predicted Cα distance is compatible with disulfide formation in only one of the two M4 conformations. AlphaFold was run on both WT ELIC and the P305A background, and although most runs returned a kinked M4 even for P305A, a subset of runs produced unkinked M4 models. These unkinked models were used to identify Cys pairs that target the unkinked conformation.

Once validated engineered Cys constructs are in hand, agonist-induced currents could be recorded in TEVC under oxidizing conditions (using H_2O_2) and under reducing conditions (using DTT). If a construct designed to lock M4 in the kinked conformation shows slow desensitization under oxidizing conditions and faster desensitization upon reduction, this would be direct functional evidence that the kinked M4 conformation supports slow desensitization. Conversely, if a construct designed to lock M4 in the unkinked conformation shows fast desensitization under oxidizing conditions and slower desensitization upon reduction, this would link the unkinked geometry to the fast-desensitizing phenotype. This experiment would directly test a central assumption of the M4-dynamics model.

5.2.4 Molecular dynamics simulations and lipid docking at the W-R-P pocket

A fourth direction is to use molecular dynamics simulations and lipid docking to estimate the binding affinity of PE and PG at the W-R-P pocket of WT ELIC and the W-R-P

pocket mutants. Calculating the ΔG of lipid binding for each mutant would test whether the changes in desensitization measured in TEVC correlate with changes in predicted lipid affinity. If mutants that accelerate desensitization also show reduced lipid affinity, this would support the model that altered desensitization is driven by altered lipid occupancy at the pocket. If some mutants accelerate desensitization without changing predicted lipid affinity, this will indicate that those residues contribute to desensitization through M4 packing or M4 conformation rather than through lipid binding directly. The same simulations could be repeated with the pocket residues mutated to alanine, individually or together, to ask which residues contribute most to lipid affinity at the site.

Extending this analysis to GLIC would be informative. In Chapter 3, I showed that mutations to the GLIC W-R-P pocket had no measurable effect on desensitization. Two interpretations are possible. The first is that lipids still bind at the GLIC pocket, but the dense aromatic network at the GLIC M4-M1/M3 interface constrains M4 and limits any functional consequence, consistent with the 3Aro experiment in ELIC (Chapter 4). The second is that lipid binding at the GLIC pocket is intrinsically weaker or different, so the pocket has less effect on M4 to begin with. Comparing the predicted ΔG of lipid binding at the WT and Ala mutant pockets in GLIC and ELIC would help isolate whether the divergent phenotype reflects a lipid binding issue, an M4 architecture issue, or both. Together with the cross-linking experiments above, these simulations would give a coherent molecular picture of what is happening at the W-R-P pocket and how it shapes ELIC desensitization.

5.3 Limitations

The conclusions in this thesis are mainly bounded by two limitations of the experimental design: the use of TEVC electrophysiology and the use of *Xenopus laevis* oocytes as the expression system. The first limitation is that the temporal resolution of TEVC set ups

is variable to each set up. Several factors play a role, including the TEVC set up and the solutions flow rate. Because solution exchange occurs on a seconds-scale time course, the assay is best suited to macroscopic changes in current. Therefore, the τ values reported in this thesis should be interpreted as apparent or macroscopic rates of the desensitization process, rather than microscopic rate constants for individual conformational transitions (Cachelin & Colquhoun, 1989; Auerbach & Akk, 1998). Fast desensitization components can be detected using TEVC set ups that minimize the deadtime between the solution and the oocytes to minimize the solution exchange time as a factor. As a result, the analysis captures whether a construct population shifts toward a macroscopic desensitizing phenotype, but it cannot define the full kinetic pathway connecting activation, opening, and desensitization.

The second limitation is that all functional measurements were performed in *Xenopus laevis* oocytes, where the lipid environment is fixed and not experimentally controlled. The oocyte plasma membrane is composed mainly of PC, sphingomyelin, PI, and cholesterol, with low PG and negligible cardiolipin (Hill et al., 2005). This lipid composition differs from the *E. coli* inner membrane, where ELIC evolved and where PE is dominant and PG is enriched (Sohlenkamp & Geiger, 2016). It also differs from mammalian synaptic membranes, where cholesterol is abundant and synaptic-vesicle lipids include PE and PS enriched in polyunsaturated sn-2 chains (Takamori et al., 2006).

As the membrane composition is fixed, the mutant phenotypes measured here report how each mutation affects channel function within one fixed lipid background. This is important for interpreting the W-R-P pocket because mutations in this region could accelerate desensitization by altering lipid binding, changing the position or dynamics of M4, or both. The data are most consistent with a model in which the pocket influences desensitization through M4 structure or dynamics, but TEVC recordings in oocytes cannot directly separate protein-intrinsic effects from lipid-dependent effects. Reconstitution of purified channels into

liposomes of defined lipid composition would be the most direct way to test whether specific lipids rescue or reproduce the phenotypes observed in oocytes.

In conclusion, TEVC in *Xenopus laevis* oocytes allowed me to compare desensitization phenotypes across a large set of mutations and receptors under the same recording conditions. Although this approach does not resolve fast kinetic steps or control membrane lipid composition, the consistency of the mutant phenotypes provides strong functional evidence that the W-R-P pocket influences desensitization. Therefore, within the limits of the assay and expression system, this work provides a coherent functional framework for how a conserved lipid-binding pocket can produce receptor-specific effects on desensitization. The next step is to test this framework in systems that provide faster kinetic resolution and direct control over the lipid environment.

5.4 Concluding remarks

This thesis advances our understanding of how the W-R-P motif and the M4-M1/M3 interface shape pLGIC desensitization. I have shown that the W-R-P pocket plays different roles in modulating desensitization across ELIC, GlyR, and GLIC, despite the conservation of the W-R-P motif and the binding of lipids and other modulators at the homologous site in all three receptors. In ELIC, the Trp224-Arg301 cation-π interaction, the Pro305 kink, and the broader aromatic packing at the M4-M1/M3 interface are key determinants of slow desensitization, likely through their effects on M4 structure or dynamics. The future experiments outlined here would directly test this model and ultimately elucidate how lipid binding and M4 conformation shape ELIC desensitization.

6 References

Akk, G., Bracamontes, J. R., Covey, D. F., Evers, A., Dao, T., & Steinbach, J. H. (2004). Neuroactive steroids have multiple actions to potentiate GABAA receptors. *Journal of Physiology*, *558*(1), 59–74. https://doi.org/10.1113/JPHYSIOL.2004.066571;PAGE:STRING:ARTICLE/CHAPTER

Akk, G., Bracamontes, J., & Steinbach, J. H. (2001). Pregnenolone sulfate block of GABAA receptors: mechanism and involvement of a residue in the M2 region of the α subunit. *The Journal of Physiology*, *532*(3), 673–684. https://doi.org/10.1111/J.1469-7793.2001.0673E.X

Akk, G., Bracamontes, J., & Steinbach, J. H. (2004). Activation of GABAA receptors containing the α4 subunit by GABA and pentobarbital. *Journal of Physiology*, *556*(2), 387–399. https://doi.org/10.1113/JPHYSIOL.2003.058230;PAGEGROUP:STRING:PUBLICATION

Akk, G., Covey, D. F., Evers, A. S., Steinbach, J. H., Zorumski, C. F., & Mennerick, S. (2009). The influence of the membrane on neurosteroid actions at GABAA receptors. *Psychoneuroendocrinology*, *34*(SUPPL. 1), S59–S66. https://doi.org/10.1016/J.PSYNEUEN.2009.05.020

Akk, G., Li, P., Bracamontes, J., Reichert, D. E., Covey, D. F., & Steinbach, J. H. (2008). Mutations of the GABA-A Receptor α1 Subunit M1 Domain Reveal Unexpected Complexity for Modulation by Neuroactive Steroids. *Molecular Pharmacology*, *74*(3), 614–627. https://doi.org/10.1124/MOL.108.048520

Akk, G., Li, P., Bracamontes, J., & Steinbach, J. H. (2009). Activation and Modulation of Concatemeric GABA-A Receptors Expressed in Human Embryonic Kidney Cells. *Molecular Pharmacology*, *75*(6), 1400–1411. https://doi.org/10.1124/MOL.108.054510

Akk, G., Shu, H. J., Wang, C., Steinbach, J. H., Zorumski, C. F., Covey, D. F., & Mennerick, S. (2005). Neurosteroid Access to the GABAA Receptor. *Journal of Neuroscience*, *25*(50), 11605–11613. https://doi.org/10.1523/JNEUROSCI.4173-05.2005

Albuquerque, E. X., Pereira, E. F. R., Alkondon, M., & Rogers, S. W. (2009). Mammalian Nicotinic Acetylcholine Receptors: From Structure to Function. *Https://Doi.Org/10.1152/Physrev.00015.2008*, *89*(1), 73–120. https://doi.org/10.1152/PHYSREV.00015.2008

Ananchenko, A., Hussein, T. O. K., Mody, D., Thompson, M. J., & Baenziger, J. E. (2022). Recent Insight into Lipid Binding and Lipid Modulation of Pentameric Ligand-Gated Ion Channels. In *Biomolecules* (Vol. 12, Number 6). MDPI. https://doi.org/10.3390/biom12060814

Arregui, A., Logan, W. J., Bennett, J. P., & Snyder, S. H. (1972). Specific glycine--accumulating synaptosomes in the spinal cord of rats. *Proceedings of the National Academy of Sciences of the United States of America*, *69*(11), 3485–3489. https://doi.org/10.1073/PNAS.69.11.3485;WGROUP:STRING:PUBLICATION

Auerbach, A. L., & Akk, G. (1998). Desensitization of Mouse Nicotinic Acetylcholine Receptor Channels A Two-Gate Mechanism. *J. Gen. Physiol*, *112*, 181–197. http://www.jgp.org

Baenziger, J. E., Domville, J. A., & Therien, J. P. D. (2017). The Role of Cholesterol in the Activation of Nicotinic Acetylcholine Receptors. In *Current Topics in Membranes* (Vol. 80, pp. 95–137). Academic Press Inc. https://doi.org/10.1016/bs.ctm.2017.05.002

Baenziger, J. E., Hénault, C. M., Therien, J. P. D., & Sun, J. (2015). Nicotinic acetylcholine receptor–lipid interactions: Mechanistic insight and biological function. *Biochimica et Biophysica Acta (BBA) - Biomembranes*, *1848*(9), 1806–1817. https://doi.org/10.1016/J.BBAMEM.2015.03.010

Baenziger, J. E., Morris, M. L., Darsaut, T. E., & Ryan, S. E. (2000). Effect of membrane lipid composition on the conformational equilibria of the nicotinic acetylcholine receptor. *Journal of Biological Chemistry*, *275*(2), 777–784. https://doi.org/10.1074/jbc.275.2.777

Basak, S., Schmandt, N., Gicheru, Y., & Chakrapani, S. (2017). Crystal structure and dynamics of a lipid-induced potential desensitized-state of a pentameric ligand-gated channel. *ELife*, *6*. https://doi.org/10.7554/eLife.23886

Beato, M., Groot-Kormelink, P. J., Colquhoun, D., & Sivilotti, L. G. (2004). The Activation Mechanism of α1 Homomeric Glycine Receptors. *Journal of Neuroscience*, *24*(4), 895–906. https://doi.org/10.1523/jneurosci.4420-03.2004

Becker, L., Von Wegerer, J., Schenkel, J., Zeilhofer, H. U., Swandulla, D., & Weiher, H. (2002). Disease-Specific Human Glycine Receptor α1 Subunit Causes Hyperekplexia Phenotype and Impaired Glycine- and GABAA-Receptor Transmission in Transgenic Mice. *Journal of Neuroscience*, *22*(7), 2505–2512. https://doi.org/10.1523/JNEUROSCI.22-07-02505.2002

Belelli, D., & Lambert, J. J. (2005). Neurosteroids: Endogenous regulators of the GABAA receptor. *Nature Reviews Neuroscience*, *6*(7), 565–575. https://doi.org/10.1038/NRN1703;KWRD

Benarroch, E. (2021). What is the role of Potassium channels in Ataxia? *Neurology*, *97*(20), 938–941. https://doi.org/10.1212/WNL.0000000000012870;WGROUP:STRING:PUBLICATION

Bennett, P. J., & Simmonds, M. A. (1996). The influence of membrane cholesterol on the GABAA receptor. *British Journal of Pharmacology*, *117*(1), 87–92. https://doi.org/10.1111/J.1476-5381.1996.TB15158.X;WEBSITE:WEBSITE:BPSPUBS;WGROUP:STRING:PUBLICATION

Bergh, C., Rovšnik, U., Howard, R., & Lindahl, E. (2024). Discovery of lipid binding sites in a ligand-gated ion channel by integrating simulations and cryo-EM. *ELife*, *13*. https://doi.org/10.7554/eLife.86016

Bertozzi, C., Zimmermann, I., Engeler, S., Hilf, R. J. C., & Dutzler, R. (2016). Signal Transduction at the Domain Interface of Prokaryotic Pentameric Ligand-Gated Ion Channels. *PLoS Biology*, *14*(3), e1002393. https://doi.org/10.1371/JOURNAL.PBIO.1002393

Bharambe, N., Li, Z., Seiferth, D., Balakrishna, A. M., Biggin, P. C., & Basak, S. (2024). Cryo-EM structures of prokaryotic ligand-gated ion channel GLIC provide insights into gating in a lipid environment. *Nature Communications*, *15*(1), 1–16. https://doi.org/10.1038/s41467-024-47370-w

Bičiková, M. (2001). Neuroactive steroids. *Psychiatrie*, *5*(SUPPL. 2), 10–11. https://doi.org/10.1096/FASEBJ.6.6.1347506;PAGEGROUP:STRING:PUBLICATION

Bocquet, N., Nury, H., Baaden, M., Le Poupon, C., Changeux, J. P., Delarue, M., & Corringer, P. J. (2009). X-ray structure of a pentameric ligand-gated ion channel in an apparently open conformation. *Nature*, *457*(7225), 111–114. https://doi.org/10.1038/nature07462

Bocquet, N., Nury, H., Baaden, M., Poupon, C. Le, Changeux, J. P., Delarue, M., & Corringer, P.-J. (2009). X-ray structure of a pentameric ligand-gated ion channel in an apparently open conformation. *Nature*, *457*(7225), 111–114. https://doi.org/10.1038/nature07462

Bode, A., & Lynch, J. W. (2014). *The impact of human hyperekplexia mutations on glycine receptor structure and function*. http://www.molecularbrain.com/content/7/1/2

Bowery, N. G., & Smart, T. G. (2006). GABA and glycine as neurotransmitters: A brief history. *British Journal of Pharmacology*, *147*(SUPPL. 1), S109–S119. https://doi.org/10.1038/SJ.BJP.0706443;SUBPAGE:STRING:FULL

Bradley, P. (1987). 5-HT3 receptors in the brain? *Nature*, *330*(6150), 696. https://doi.org/10.1038/330696A0;KWRD

Brams, M., Govaerts, C., Kambara, K., Price, K., Spurny, R., Gharpure, A., Pardon, E., Evans, G. L., Bertrand, D., Lummis, S. C. R., Hibbs, R. E., Steyaert, J., & Ulens, C. (2020). Modulation of the erwinia ligand-gated ion channel (ELIC) and the 5-HT3 receptor via a common vestibule site. *ELife*, *9*. https://doi.org/10.7554/eLife.51511

Breitinger, H. G., Lanig, H., Vohwinkel, C., Grewer, C., Breitinger, U., Clark, T., & Becker, C. M. (2004). Molecular Dynamics Simulation Links Conformation of a Pore-Flanking Region to Hyperekplexia-Related Dysfunction of the Inhibitory Glycine Receptor. *Chemistry & Biology*, *11*(10), 1339–1350. https://doi.org/10.1016/J.CHEMBIOL.2004.07.008

Brejc, K. Ï., Dijk, W. J. Van, Klaassen[2], R. V, Schuurmans[2], M., Oost[23], J. Van Der, Smit[2], A. B., & Sixma, T. K. (2001). Crystal structure of an ACh-binding protein reveals the ligand-binding domain of nicotinic receptors. *Nature 2001 411:6835*, *411*(6835), 269–276. https://doi.org/10.1038/35077011

Briley, M. S., & Changeux, J. P. (1977). Isolation and Purification of the Nicotinic Acetylcholine Receptor and Its Functional Reconstitution into a Membrane Environment. *International Review of Neurobiology*, *20*(C), 31–63. https://doi.org/10.1016/S0074-7742(08)60650-9

Brisson, A., & Unwin, P. N. T. (1985). Quaternary structure of the acetylcholine receptor. *Nature 1985 315:6019*, *315*(6019), 474–477. https://doi.org/10.1038/315474a0

Bristow, D. R., & Martin, I. L. (1987). Solubilisation of the γ-Aminobutyric Acid/Benzodiazepine Receptor from Rat Cerebellum: Optimal Preservation of the Modulatory Responses by Natural Brain Lipids. *Journal of Neurochemistry*, *49*(5), 1386–1393. https://doi.org/10.1111/J.1471-4159.1987.TB01004.X;CTYPE:STRING:JOURNAL

Brophy, P., & Shen, K. (2009). Neuronal and glial cell biology. *Current Opinion in Neurobiology*, *19*(5), 459. https://doi.org/10.1016/J.CONB.2009.10.013

Cachelin, A. B., & Colquhoun, D. (1989). DESENSITIZATION OF THE ACETYLCHOLINE RECEPTOR OF FROG END-PLATES MEASURED IN A VASELINE-GAP VOLTAGE CLAMP A. B. CA CHELIN AND D. COLQ UlHOUX INTRODUCTION. In *Journal of Physiology* (Vol. 415).

Calinsky, R., & Levy, Y. (2024). Aromatic Residues in Proteins: Re-Evaluating the Geometry and Energetics of π–π, Cation−π, and CH−π Interactions. *The Journal of Physical Chemistry B*, *128*(36), 8687–8700. https://doi.org/10.1021/ACS.JPCB.4C04774

Carswell, C. L., Hénault, C. M., Murlidaran, S., Therien, J. P. D., Juranka, P. F., Surujballi, J. A., Brannigan, G., & Baenziger, J. E. (2015). Role of the Fourth Transmembrane α Helix in the Allosteric Modulation of Pentameric Ligand-Gated Ion Channels. *Structure*, *23*(9), 1655–1664. https://doi.org/10.1016/j.str.2015.06.020

Carswell, C. L., Sun, J., & Baenziger, J. E. (2015). Intramembrane aromatic interactions influence the lipid sensitivities of pentameric ligand-gated ion channels. *Journal of Biological Chemistry*, *290*(4), 2496–2507. https://doi.org/10.1074/jbc.M114.624395

Catterall, W. A. (1996). Introduction: Ion channels in plasma membrane signal transduction. *Journal of Bioenergetics and Biomembranes*, *28*(3), 217–218. https://doi.org/10.1007/BF02110696

Catterall, W. A., Raman, I. M., Robinson, H. P. C., Sejnowski, T. J., & Paulsen, O. (2012). The hodgkin-huxley heritage: From channels to circuits. *Journal of Neuroscience*, *32*(41), 14064–14073. https://doi.org/10.1523/jneurosci.3403-12.2012

Celie, P. H. N., van Rossum-Fikkert, S. E., van Dijk, W. J., Brejc, K., Smit, A. B., & Sixma, T. K. (2004). Nicotine and Carbamylcholine Binding to Nicotinic Acetylcholine Receptors as Studied in AChBP Crystal Structures. *Neuron*, *41*(6), 907–914. https://doi.org/10.1016/S0896-6273(04)00115-1

Changeux, J. P., Kasai, M., & Lee, C. Y. (1970). Use of a snake venom toxin to characterize the cholinergic receptor protein. *Proceedings of the National Academy of Sciences of the United States of America*, *67*(3), 1241–1247. https://doi.org/10.1073/PNAS.67.3.1241

Chen, Q., Wells, M. M., Arjunan, P., Tillman, T. S., Cohen, A. E., Xu, Y., & Tang, P. (2018). Structural basis of neurosteroid anesthetic action on GABAA receptors. *Nature Communications 2018 9:1*, *9*(1), 1–10. https://doi.org/10.1038/s41467-018-06361-4

Chen, X., Webb, T. I., & Lynch, J. W. (2009). The M4 transmembrane segment contributes to agonist efficacy differences between α 1 and α 3 glycine receptors. *Molecular Membrane Biology*, *26*(5–7), 321–332. https://doi.org/10.1080/09687680903120319

Cheng, W. W. L., & Arcario, M. J. (2026). Structure–Function Studies of Pentameric Ligand-Gated Ion Channels: Combining Experimental and Computational Approaches. In *Advances in Experimental Medicine and Biology* (Vol. 1497, pp. 287–306). Springer. https://doi.org/10.1007/978-3-032-07523-9_11

Chung, S. K., Vanbellinghen, J. F., Mullins, J. G. L., Robinson, A., Hantke, J., Hammond, C. L., Gilbert, D. F., Freilinger, M., Ryan, M., Kruer, M. C., Masri, A., Gurses, C., Ferrie, C., Harvey, K., Shiang, R., Christodoulou, J., Andermann, F., Andermann, E., Thomas, R. H., … Rees, M. I. (2010). Pathophysiological

Mechanisms of Dominant and Recessive GLRA1 Mutations in Hyperekplexia. *Journal of Neuroscience*, *30*(28), 9612–9620. https://doi.org/10.1523/JNEUROSCI.1763-10.2010

Claudio, T., Ballivet, M., Patrick, J., & Heinemann, S. (1983). Nucleotide and deduced amino acid sequences of Torpedo californica acetylcholine receptor γ subunit. *Proceedings of the National Academy of Sciences of the United States of America*, *80*(4 I), 1111–1115. https://doi.org/10.1073/PNAS.80.4.1111;WGROUP:STRING:PUBLICATION

Cordes, F. S., Bright, J. N., & Sansom, M. S. P. (2002). Proline-induced Distortions of Transmembrane Helices. *Journal of Molecular Biology*, *323*(5), 951–960. https://doi.org/10.1016/S0022-2836(02)01006-9

Cory-Wright, J., Alqazzaz, M., Wroe, F., Jeffreys, J., Zhou, L., & Lummis, S. C. R. (2018). Aromatic Residues in the Fourth Transmembrane-Spanning Helix M4 Are Important for GABAρ Receptor Function. *ACS Chemical Neuroscience*, *9*(2), 284–290. https://doi.org/10.1021/acschemneuro.7b00315

Criado, M., Eibl, H., & Barrantes, F. J. (1982). Effects of Lipids on Acetylcholine Receptor. Essential Need of Cholesterol for Maintenance of Agonist-Induced State Transitions in Lipid Vesicles. *Biochemistry*, *21*(15), 3622–3629. https://doi.org/10.1021/bi00258a015

Criado, M., Eibl, H., & Barrantes, F. J. (1984). Functional properties of the acetylcholine receptor incorporated in model lipid membranes. Differential effects of chain length and head group of phospholipids on receptor affinity states and receptor-mediated ion translocation. *Journal of Biological Chemistry*, *259*(14), 9188–9198. https://doi.org/10.1016/S0021-9258(17)47283-8

Curtis, D. R., & Ryall, R. W. (1964). Nicotinic and Muscarinic Receptors of Renshaw Cells. *Nature 1964 203:4945*, *203*(4945), 652–653. https://doi.org/10.1038/203652a0

daCosta, C. J. B., & Baenziger, J. E. (2009). A lipid-dependent uncoupled conformation of the acetylcholine receptor. *The Journal of Biological Chemistry*, *284*(26), 17819–17825. https://doi.org/10.1074/JBC.M900030200

daCosta, C. J. B., Dey, L., Therien, J. P. D., & Baenziger, J. E. (2013). A distinct mechanism for activating uncoupled nicotinic acetylcholine receptors. *Nature Chemical Biology*, *9*(11), 701–707. https://doi.org/10.1038/nchembio.1338

daCosta, C. J. B., Medaglia, S. A., Lavigne, N., Wang, S., Carswell, C. L., & Baenzinger, J. E. (2009). Anionic lipids allosterically modulate multiple nicotinic acetylcholine receptor conformational equilibria. *Journal of Biological Chemistry*, *284*(49), 33841–33849. https://doi.org/10.1074/jbc.M109.048280

daCosta, C. J. B., Ogrel, A. A., McCardy, E. A., Blanton, M. P., & Baenziger, J. E. (2002). Lipid-protein interactions at the nicotinic acetylcholine receptor. A functional coupling between nicotinic receptors and phosphatidic acid-containing lipid bilayers. *Journal of Biological Chemistry*, *277*(1), 201–208. https://doi.org/10.1074/jbc.M108341200

Dalal, V., Arcario, M. J., Petroff, J. T., Tan, B. K., Dietzen, N. M., Rau, M. J., Fitzpatrick, J. A. J., Brannigan, G., & Cheng, W. W. L. (2024). Lipid nanodisc scaffold and size alter the structure of a pentameric ligand-gated ion channel. *Nature Communications*, *15*(1). https://doi.org/10.1038/s41467-023-44366-w

Dalal, V., Tan, B. K., Xu, H., & Cheng, W. W. L. (2025). Cryo-EM structures of a pentameric ligand-gated ion channel in liposomes. *ELife*, *14*. https://doi.org/10.7554/elife.106728

Dale, H. H. (1936). SOME RECENT EXTENSIONS OF CHEMICAL TRANSMISSION. *Cold Spring Harbor Symposia on Quantitative Biology*, *4*(0), 143–149. https://doi.org/10.1101/SQB.1936.004.01.015

Dämgen, M. A., & Biggin, P. C. (2021). State-dependent protein-lipid interactions of a pentameric ligand-gated ion channel in a neuronal membrane. *PLOS Computational Biology*, *17*(2), e1007856. https://doi.org/10.1371/JOURNAL.PCBI.1007856

Damle, V. N., & Karlin, A. (1978). Affinity labeling of one of two α-neurotoxin binding sites in acetylcholine receptor from Torpedo californica. *Biochemistry*, *17*(11), 2039–2045. https://doi.org/10.1021/bi00604a002

Davies, J. S., Chung, S. K., Thomas, R. H., Robinson, A., Hammond, C. L., Mullins, J. G. L., Carta, E., Pearce, B. R., Harvey, K., Harvey, R. J., & Rees, M. I. (2010). The glycinergic system in human startle disease: A genetic screening approach. *Frontiers in Molecular Neuroscience*, *3*(MAR), 1116. https://doi.org/10.3389/FNMOL.2010.00008/XML

Dennis, M., Giraudat, J., Kotzyba-Hibert, F., Goeldner, M., Hirth, C., Chang, J. Y., Lazure, C., Chretien, M., & Changeux, J. P. (1988). Amino acids of the Torpedo marmorata acetylcholine receptor .alpha. subunit labeled by a photoaffinity ligand for the acetylcholine binding site. *Biochemistry*, *27*(7), 2346–2357. https://doi.org/10.1021/bi00407a016

Devillers Thiery, A., Giraudat, J., Bentaboulet, M., & Changeux, J. P. (1983). Complete mRNA coding sequence of the acetylcholine binding α-subunit of Torpedo marmorata acetylcholine receptor: A model for the transmembrane organization of the polypeptide chain. *Proceedings of the National Academy of Sciences of the United States of America*, *80*(7 I), 2067–2071. https://doi.org/10.1073/PNAS.80.7.2067;WEBSITE:WEBSITE:PNAS-SITE;WGROUP:STRING:PUBLICATION

Dietzen, N. M., Arcario, M. J., Chen, L. J., Petroff, J. T., Moreland, K. T., Krishnan, K., Brannigan, G., Covey, D. F., & Cheng, W. W. L. (2022). Polyunsaturated fatty acids inhibit a pentameric ligand-gated ion channel through one of two binding sites. *ELife*, *11*, 1–25. https://doi.org/10.7554/elife.74306

Dietzen, N., Petroff, J. T., Covey, D. F., & Cheng, W. W. L. (2021). Fatty Acids Inhibit a Pentameric Ligand-Gated Ion Channel through One of Two Binding Sites. *Biophysical Journal*, *120*(3), 56a. https://doi.org/10.1016/j.bpj.2020.11.575

Dudel, J., & Kuffler, S. W. (1961a). Mechanism of facilitation at the crayfish neuromuscular junction. *The Journal of Physiology*, *155*(3), 530. https://doi.org/10.1113/JPHYSIOL.1961.SP006645

Dudel, J., & Kuffler, S. W. (1961b). Presynaptic inhibition at the crayfish neuromuscular junction. *The Journal of Physiology*, *155*(3), 543. https://doi.org/10.1113/JPHYSIOL.1961.SP006646

Dudel, J., & Kuffler, S. W. (1961c). The quantal nature of transmission and spontaneous miniature potentials at the crayfish neuromuscular junction. *The Journal of Physiology*, *155*(3), 514. https://doi.org/10.1113/JPHYSIOL.1961.SP006644

Edwards, C., & Kuffler, S. W. (1959). THE BLOCKING EFFECT OF y-AMINOBUTYRIC ACID (GABA) AND THE ACTION OF RELATED COMPOUNDS ON SINGLE NERVE CELLS. *Journal of Neurochemistry*, *4*(1), 19–30. https://doi.org/10.1111/J.1471-4159.1959.TB13170.X;CTYPE:STRING:JOURNAL

Eisenman, L. N., He, Y., Fields, C., Zorumski, C. F., & Mennerick, S. (2003). Activation-dependent properties of pregnenolone sulfate inhibition of GABAA receptor-mediated current. *Journal of Physiology*, *550*(3), 679–691. https://doi.org/10.1113/JPHYSIOL.2003.043810;JOURNAL:JOURNAL:14697793;WGROUP:STRING:PUBLICATION

Epstein, M., & Racker, E. (1978). Reconstitution of carbamylcholine-dependent sodium ion flux and desensitization of the acetylcholine receptor from Torpedo californica. *Journal of Biological Chemistry*, *253*(19), 6660–6662. https://doi.org/10.1016/S0021-9258(17)37967-X

Ferraro, N. A., & Cascio, M. (2018). Cross-Linking-Mass Spectrometry Studies of Cholesterol Interactions with Human α1 Glycine Receptor. *Analytical Chemistry*, *90*(4), 2508–2516. https://doi.org/10.1021/acs.analchem.7b03639

Fong, T. M., & McNamee, M. G. (1986). Correlation between acetylcholine receptor function and structural properties of membranes. *Biochemistry*, *25*(4), 830–840. https://doi.org/10.1021/BI00352A015

Fourati, Z., Howard, R. J., Heusser, S. A., Hu, H., Ruza, R. R., Sauguet, L., Lindahl, E., & Delarue, M. (2018). Structural Basis for a Bimodal Allosteric Mechanism of General Anesthetic Modulation in Pentameric Ligand-Gated Ion Channels. *Cell Reports*, *23*(4), 993–1004. https://doi.org/10.1016/J.CELREP.2018.03.108

Fourati, Z., Ruza, R. R., Laverty, D., Drège, E., Delarue-Cochin, S., Joseph, D., Koehl, P., Smart, T., & Delarue, M. (2017). Barbiturates bind in the GLIC ion channel pore and cause inhibition by stabilizing a closed state. *Journal of Biological Chemistry*, *292*(5), 1550–1558. http://www.jbc.org/article/S0021925820366898/fulltext

Fourati, Z., Sauguet, L., & Delarue, M. (2015). Genuine open form of the pentameric ligand-gated ion channel GLIC. *Acta Crystallographica Section D: Biological Crystallography*, *71*, 454–460. https://doi.org/10.1107/S1399004714026698

Franke, C., Parnas, H., Hovav, G., & Dudel, J. (1993). A molecular scheme for the reaction between acetylcholine and nicotinic channels. *Biophysical Journal*, *64*(2), 339–356. https://doi.org/10.1016/S0006-3495(93)81374-2

Gallivan, J. P., & Dougherty, D. A. (1999). Cation-π interactions in structural biology. *Proceedings of the National Academy of Sciences*, *96*(17), 9459–9464. https://doi.org/10.1073/pnas.96.17.9459

Galzi, J. L., Revah, F., Black, D., Goeldner, M., Hirth, C., & Changeux, J. P. (1990). Identification of a novel amino acid alpha-tyrosine 93 within the cholinergic ligands-binding sites of the acetylcholine receptor by photoaffinity labeling. Additional evidence for a three-loop model of the cholinergic ligands-binding sites. *Journal of Biological Chemistry*, *265*(18), 10430–10437. https://doi.org/10.1016/S0021-9258(18)86964-2

Gibbs, E., Klemm, E., Seiferth, D., Kumar, A., Ilca, S. L., Biggin, P. C., & Chakrapani, S. (2023). Conformational transitions and allosteric modulation in a heteromeric glycine receptor. *Nature Communications 2023 14:1*, *14*(1), 1–15. https://doi.org/10.1038/s41467-023-37106-7

Gielen, M., Barilone, N., & Corringer, P. J. (2020). The desensitization pathway of GABAA receptors, one subunit at a time. *Nature Communications*, *11*(1), 1–14. https://doi.org/10.1038/s41467-020-19218-6

Gielen, M., & Corringer, P.-J. (2018a). The dual-gate model for pentameric ligand-gated ion channels activation and desensitization. In *The Journal of Physiology* (Vol. 596, Number 10, pp. 1873–1902). Blackwell Publishing Ltd. https://doi.org/10.1113/jp275100

Gielen, M., & Corringer, P.-J. (2018b). The dual-gate model for pentameric ligand-gated ion channels activation and desensitization. *The Journal of Physiology*, *596*(10), 1873–1902. https://doi.org/10.1113/JP275100

Gielen, M., Thomas, P., & Smart, T. G. (2015a). The desensitization gate of inhibitory Cys-loop receptors. *Nature Communications*, *6*. https://doi.org/10.1038/ncomms7829

Gielen, M., Thomas, P., & Smart, T. G. (2015b). The desensitization gate of inhibitory Cys-loop receptors. *Nature Communications*, *6*. https://doi.org/10.1038/ncomms7829

Gonzalez-Gutierrez, G., Cuello, L. G., Nair, S. K., & Grosman, C. (2013). Gating of the proton-gated ion channel from Gloeobacter violaceus at pH 4 as revealed by X-ray crystallography. *Proceedings of the National Academy of Sciences of the United States of America*, *110*(46), 18716–18721. https://doi.org/10.1073/PNAS.1313156110

Gonzalez-Gutierrez, G., Lukk, T., Agarwal, V., Papke, D., Nair, S. K., & Grosman, C. (2012). Mutations that stabilize the open state of the Erwinia chrisanthemi ligand-gated ion channel fail to change the conformation of the pore domain in crystals.

Proceedings of the National Academy of Sciences of the United States of America, *109*(16), 6331–6336. https://doi.org/10.1073/pnas.1119268109

Grenningloh, G., Rienitz, A., Schmitt, B., Methfessel, C., Zensen, M., Beyreuther, K., Gundelfinger, E. D., & Betz, H. (1988). The strychnine-binding subunit of the glycine receptor shows homology with nicotinic acetylcholine receptors. *Nature*, *328*(6127), 215–220. https://doi.org/10.1038/328215A0;KWRD

Haeger, S., Kuzmin, D., Detro-Dassen, S., Lang, N., Kilb, M., Tsetlin, V., Betz, H., Laube, B., & Schmalzing, G. (2009). An intramembrane aromatic network determines pentameric assembly of Cys-loop receptors. *Nature Structural & Molecular Biology 2009 17:1*, *17*(1), 90–98. https://doi.org/10.1038/nsmb.1721

Hamouda, A. K., Sanghvi, M., Sauls, D., Machu, T. K., & Blanton, M. P. (2006). Assessing the lipid requirements of the Torpedo californica nicotinic acetylcholine receptor. *Biochemistry*, *45*(13), 4327–4337. https://doi.org/10.1021/bi052281z

Hansen, S. B., Sulzenbacher, G., Huxford, T., Marchot, P., Taylor, P., & Bourne, Y. (2005). Structures of Aplysia AChBP complexes with nicotinic agonists and antagonists reveal distinctive binding interfaces and conformations. *The EMBO Journal*, *24*(20), 3635. https://doi.org/10.1038/SJ.EMBOJ.7600828

Hayoundjian, H., Paul, S. M., & Skolnick, P. (1986). The permeability of γ-aminobutyric acid-gated chloride channels is described by the binding of a 'cage' convulsant, t-butylbicyclophosphoro[35S]thionate. *Proceedings of the National Academy of Sciences of the United States of America*, *83*(23), 9241–9244. https://doi.org/10.1073/PNAS.83.23.9241;PAGE:STRING:ARTICLE/CHAPTER

HEIDMANN, T., SOBEL, A., POPOT, J. -L, & Changeux, J. P. (1980). Reconstitution of a Functional Acetylcholine Receptor. *European Journal of Biochemistry*, *110*(1), 35–55. https://doi.org/10.1111/J.1432-1033.1980.TB04839.X

Hénault, C. M., Govaerts, C., Spurny, R., Brams, M., Estrada-Mondragón, A., Lynch, J., Bertrand, D., Pardon, E., Evans, G. L., Woods, K., Elberson, B. W., Cuello, L. G., Brannigan, G., Nury, H., Steyaert, J., Baenziger, J. E., & Ulens, C. (2019). A lipid site shapes the agonist response of a pentameric ligand-gated ion channel. *Nature Chemical Biology*, *15*(12), 1156–1164. https://doi.org/10.1038/s41589-019-0369-4

Hénault, C. M., Juranka, P. F., & Baenziger, J. E. (2015). The M4 Transmembrane α-Helix Contributes Differently to Both the Maturation and Function of Two Prokaryotic Pentameric Ligand-gated Ion Channels *. *Journal of Biological Chemistry*, *290*(41), 25118–25128. https://doi.org/10.1074/JBC.M115.676833

Hilf, R. J. C., Bertozzi, C., Zimmermann, I., Reiter, A., Trauner, D., & Dutzler, R. (2010). Structural basis of open channel block in a prokaryotic pentameric ligand-gated ion channel. *Nature Structural and Molecular Biology*, *17*(11), 1330–1336. https://doi.org/10.1038/NSMB.1933

Hilf, R. J. C., & Dutzler, R. (2008). X-ray structure of a prokaryotic pentameric ligand-gated ion channel. *Nature*, *452*(7185), 375–379. https://doi.org/10.1038/nature06717

Hilf, R. J. C., Dutzler, R., RJ, H., & R, D. (2009). Structure of a potentially open state of a proton-activated pentameric ligand-gated ion channel. *Nature*, *457*(7225), 115–118. https://doi.org/10.1038/nature07461

Hille, B., Armstrong, C. M., & MacKinnon, R. (1999). Ion channels: From idea to reality. *Nature Medicine*, *5*(10), 1105–1109. https://doi.org/10.1038/13415

Hodgkin, A. L. (1948). The local electric changes associated with repetitive action in a non-medullated axon. *The Journal of Physiology*, *107*(2), 165–181. https://doi.org/10.1113/jphysiol.1948.sp004260

HODGKIN, A. L., & HUXLEY, A. F. (1952). Currents carried by sodium and potassium ions through the membrane of the giant axon of Loligo. *The Journal of Physiology*, *116*(4), 449–472. https://doi.org/10.1113/jphysiol.1952.sp004717

HODGKIN, A. L., & KATZ, B. (1949). The effect of sodium ions on the electrical activity of giant axon of the squid. *The Journal of Physiology*, *108*(1), 37–77. https://doi.org/10.1113/jphysiol.1949.sp004310

Hu, H., Ataka, K., Menny, A., Fourati, Z., Sauguet, L., Corringer, P.-J., Koehl, P., Heberle, J., & Delarue, M. (2018). Electrostatics, proton sensor, and networks governing the gating transition in GLIC, a proton-gated pentameric ion channel. *Proceedings of the National Academy of Sciences of the United States of America*, *115*(52), E12172–E12181. https://doi.org/10.1073/pnas.1813378116

Hu, H., Howard, R. J., Bastolla, U., Lindahl, E., & Delarue, M. (2020). Structural basis for allosteric transitions of a multidomain pentameric ligand-gated ion channel. *Proceedings of the National Academy of Sciences*, *117*(24), 13437–13446. https://doi.org/10.1073/PNAS.1922701117

Hu, H., Nemecz, Á., Renterghem, C. Van, Fourati, Z., Sauguet, L., Corringer, P.-J., Delarue, M., & Renterghem, C. Van. (2018). Crystal structures of a pentameric ion channel gated by alkaline pH show a widely open pore and identify a cavity for modulation. *Proceedings of the National Academy of Sciences*, *115*(17), E3959–E3968. https://doi.org/10.1073/PNAS.1717700115

Ivica, J., Lape, R., Jazbec, V., Yu, J., Zhu, H., Gouaux, E., Gold, M. G., & Sivilotti, L. G. (2021). The intracellular domain of homomeric glycine receptors modulates agonist efficacy. *Journal of Biological Chemistry*, *296*, 100387. https://doi.org/10.1074/JBC.RA119.012358/ATTACHMENT/38ED8678-E00C-462F-A002-5C8AC994826E/MMC1.PDF

Jones, O. T., Eubanks, J. H., Earnest, J. P., & McNamee, M. G. (1988). A Minimum Number of Lipids Are Required To Support the Functional Properties of the Nicotinic Acetylcholine Receptor1. *Biochemistry*, *27*, 3733–3742. https://pubs.acs.org/sharingguidelines

Jones, O. T., & Mcnamee, M. G. (1988). Annular and nonannular binding sites for cholesterol associated with the nicotinic acetylcholine receptor. *Biochemistry*, *27*(7), 2364–2374. https://doi.org/10.1021/BI00407A018

Jones, M. V, & Westbrook, G. L. (1995). Desensitized states prolong GABAA channel responses to brief agonist pulses. *Neuron*, *15*(1), 181–191. https://doi.org/10.1016/0896-6273(95)90075-6

Jones, M. V., & Westbrook, G. L. (1996). The impact of receptor desensitization on fast synaptic transmission. *Trends in Neurosciences*, *19*(3), 96–101. https://doi.org/10.1016/S0166-2236(96)80037-3

Jumper, J., Evans, R., Pritzel, A., Green, T., Figurnov, M., Ronneberger, O., Tunyasuvunakool, K., Bates, R., Žídek, A., Potapenko, A., Bridgland, A., Meyer, C., Kohl, S. A. A., Ballard, A. J., Cowie, A., Romera-Paredes, B., Nikolov, S., Jain, R., Adler, J., … Hassabis, D. (2021). Highly accurate protein structure prediction with AlphaFold. *Nature 2021 596:7873*, *596*(7873), 583–589. https://doi.org/10.1038/s41586-021-03819-2

Karlin, A., & Cowburn, D. (1973). The affinity labeling of partially purified acetylcholine receptor from electric tissue of Electrophorus. *Proceedings of the National Academy of Sciences of the United States of America*, *70*(12 (I)), 3636–3640. https://doi.org/10.1073/PNAS.70.12.3636;PAGE:STRING:ARTICLE/CHAPTER

Kilpatrick, G. J., Jones, B. J., & Tyers, M. B. (1987). Identification and distribution of 5-HT3 receptors in rat brain using radioligand binding. *Nature*, *330*(6150), 746–748. https://doi.org/10.1038/330746A0;KWRD

Kim, J. J., Gharpure, A., Teng, J., Zhuang, Y., Howard, R. J., Zhu, S., Noviello, C. M., Walsh, R. M., Lindahl, E., & Hibbs, R. E. (2020). Shared structural mechanisms of general anaesthetics and benzodiazepines. *Nature*, *585*(7824), 303–308. https://doi.org/10.1038/s41586-020-2654-5

Kinde, M. N., Chen, Q., Lawless, M. J., Mowrey, D. D., Xu, J., Saxena, S., Xu, Y., & Tang, P. (2015). Conformational Changes Underlying Desensitization of the Pentameric Ligand-Gated Ion Channel ELIC. *Structure (London, England : 1993)*, *23*(6), 995–1004. https://doi.org/10.1016/J.STR.2015.03.017

Kuffler, S. W., & Edwards, C. (1958). MECHANISM OF GAMMA AMINOBUTYRIC ACID (GABA) ACTION AND ITS RELATION TO SYNAPTIC INHIBITION. *Journal of Neurophysiology*, *21*(6), 589–610. https://doi.org/10.1152/jn.1958.21.6.589

Kuffler, S. W., & Eyzaguirre, C. (1955). SYNAPTIC INHIBITION IN AN ISOLATED NERVE CELL. *The Journal of General Physiology*, *39*(1), 155–184. https://doi.org/10.1085/jgp.39.1.155

Kuffler, S. W., & Yoshikami, D. (1975a). The distribution of acetylcholine sensitivity at the post-synaptic membrane of vertebrate skeletal twitch muscles: iontophoretic mapping in the micron range. *The Journal of Physiology*, *244*(3), 703–730. https://doi.org/10.1113/JPHYSIOL.1975.SP010821;JOURNAL:JOURNAL:14697793;WGROUP:STRING:PUBLICATION

Kuffler, S. W., & Yoshikami, D. (1975b). The number of transmitter molecules in a quantum: an estimate from iontophoretic application of acetylcholine at the neuromuscular synapse. *The Journal of Physiology*, *251*(2), 465–482. https://doi.org/10.1113/JPHYSIOL.1975.SP011103;CTYPE:STRING:JOURNAL

Kumar, A., Basak, S., Rao, S., Gicheru, Y., Mayer, M. L., Sansom, M. S. P., & Chakrapani, S. (2020a). Mechanisms of activation and desensitization of full-length glycine receptor in lipid nanodiscs. *Nature Communications*, *11*(1), 1–14. https://doi.org/10.1038/s41467-020-17364-5

Kumar, A., Basak, S., Rao, S., Gicheru, Y., Mayer, M. L., Sansom, M. S. P., & Chakrapani, S. (2020b). Mechanisms of activation and desensitization of full-length glycine receptor in lipid nanodiscs. *Nature Communications*, *11*(1), 1–14. https://doi.org/10.1038/s41467-020-17364-5

Kumar, A., Kindig, K., Rao, S., Zaki, A.-M., Basak, S., Sansom, M. S. P., Biggin, P. C., & Chakrapani, S. (2022a). Structural basis for cannabinoid-induced potentiation of alpha1-glycine receptors in lipid nanodiscs. *Nature Communications 2022 13:1*, *13*(1), 1–14. https://doi.org/10.1038/s41467-022-32594-5

Kumar, A., Kindig, K., Rao, S., Zaki, A.-M., Basak, S., Sansom, M. S. P., Biggin, P. C., & Chakrapani, S. (2022b). Structural basis for cannabinoid-induced potentiation of

alpha1-glycine receptors in lipid nanodiscs. *Nature Communications 2022 13:1*, *13*(1), 1–14. https://doi.org/10.1038/s41467-022-32594-5

Kumar, P., Cymesa, G. D., & Grosman, C. (2021). Structure and function at the lipid-protein interface of a pentameric ligand-gated ion channel. *Proceedings of the National Academy of Sciences of the United States of America*, *118*(23). https://doi.org/10.1073/pnas.2100164118

Kumar, P., Wang, Y., Zhang, Z., Zhao, Z., Cymesa, G. D., Tajkhorshid, E., & Grosman, C. (2020). Cryo-EM structures of a lipid-sensitive pentameric ligand-gated ion channel embedded in a phosphatidylcholine-only bilayer. *Proceedings of the National Academy of Sciences of the United States of America*, *117*(3), 1788–1798. https://www.pnas.org/content/117/3/1788

Labriola, J. M., Pandhare, A., Jansen, M., Blanton, M. P., Corringer, P.-J., & Baenziger, J. E. (2013). Structural sensitivity of a prokaryotic pentameric ligand-gated ion channel to its membrane environment. *Journal of Biological Chemistry*, *288*(16), 11294–11303. https://doi.org/10.1074/jbc.M113.458133

Langlhofer, G., Janzen, D., Meiselbach, H., & Villmann, C. (2015). Length of the TM3-4 loop of the glycine receptor modulates receptor desensitization. *Neuroscience Letters*, *600*, 176–181. https://doi.org/10.1016/j.neulet.2015.06.017

Langlhofer, G., & Villmann, C. (2016). The intracellular loop of the glycine receptor: It's not all about the size. *Frontiers in Molecular Neuroscience*, *9*(JUNE), 1–14. https://doi.org/10.3389/fnmol.2016.00041

Laverty, D., Desai, R., Uchański, T., Masiulis, S., Stec, W. J., Malinauskas, T., Zivanov, J., Pardon, E., Steyaert, J., Miller, K. W., & Aricescu, A. R. (2019). Cryo-EM

structure of the human α1β3γ2 GABAA receptor in a lipid bilayer. *Nature*, *565*(7740), 516–520. https://doi.org/10.1038/s41586-018-0833-4

Laverty, D., Thomas, P., Field, M., Andersen, O. J., Gold, M. G., Biggin, P. C., Gielen, M., & Smart, T. G. (2017a). Crystal structures of a GABA A -receptor chimera reveal new endogenous neurosteroid-binding sites. *Nature Structural and Molecular Biology*, *24*(11), 977–985. https://doi.org/10.1038/nsmb.3477

Laverty, D., Thomas, P., Field, M., Andersen, O. J., Gold, M. G., Biggin, P. C., Gielen, M., & Smart, T. G. (2017b). Crystal structures of a GABA A -receptor chimera reveal new endogenous neurosteroid-binding sites. *Nature Structural and Molecular Biology*, *24*(11), 977–985. https://doi.org/10.1038/nsmb.3477

Lee, A. G. (2021a). Interfacial binding sites for cholesterol on GABA A receptors and competition with neurosteroids. *Biophysical Journal*, *120*(13), 2710–2722. https://doi.org/10.1016/J.BPJ.2021.05.009

Lee, A. G. (2021b). Interfacial binding sites for cholesterol on GABAA receptors and competition with neurosteroids. *Biophysical Journal*, *120*(13), 2710–2722. https://doi.org/10.1016/j.bpj.2021.05.009

Lee, W. Y., Free, C. R., & Sine, S. M. (2009). Binding to Gating Transduction in Nicotinic Receptors: Cys-Loop Energetically Couples to Pre-M1 and M2–M3 Regions. *Journal of Neuroscience*, *29*(10), 3189–3199. https://doi.org/10.1523/JNEUROSCI.6185-08.2009

Lee, W. Y., & Sine, S. M. (2005). Principal pathway coupling agonist binding to channel gating in nicotinic receptors. *Nature*, *438*(7065), 243–247. https://doi.org/10.1038/nature04156

Lindstrom, J. M., Engel, A. G., Seybold, M. E., Lennon, V. A., & Lambert, E. H. (1976). Pathological mechanisms in experimental autoimmune myasthenia gravis. II. Passive transfer of experimental autoimmune myasthenia gravis in rats with anti-acetylcholine recepotr antibodies. *Journal of Experimental Medicine*, *144*(3), 739–753. https://doi.org/10.1084/JEM.144.3.739

Louis, S., Dalal, V., Arcario, M. J., Dietzen, N. M., Rau, M. J., Fitzpatrick, J. A. J., Brannigan, G., Cheng, W. W. L., & Biology, I. (2022). *Lipid nanodisc scaffold and size alters the structure of a pentameric ligand-gated ion channel*.

Lummis, S. C. R. (2012). 5-HT3 Receptors. *Journal of Biological Chemistry*, *287*(48), 40239–40245. https://doi.org/10.1074/JBC.R112.406496

Lycksell, M., Rovšnik, U., Bergh, C., Johansen, N. T., Martel, A., Porcar, L., Arleth, L., Howard, R. J., & Lindahl, E. (2021). Probing solution structure of the pentameric ligand-gated ion channel GLIC by small-angle neutron scattering. *Proceedings of the National Academy of Sciences of the United States of America*, *118*(37). https://doi.org/10.1101/2021.04.10.439285

Lynch, J. W. (2004). Molecular structure and function of the glycine receptor chloride channel. *Physiological Reviews*, *84*(4), 1051–1095. https://doi.org/10.1152/PHYSREV.00042.2003/ASSET/IMAGES/LARGE/Z9J004 0403220006.JPEG

Majewska, M. D., Harrison, N. L., Schwartz, R. D., Barker, J. L., & Paul, S. M. (1986). Steroid hormone metabolites are barbiturate-like modulators of the GABA receptor. *Science*, *232*(4753), 1004–1007. https://doi.org/10.1126/SCIENCE.2422758;PAGE:STRING:ARTICLE/CHAPTER

Majewska, M. D., Mienville, J. M., & Vicini, S. (1988). Neurosteroid pregnenolone sulfate antagonizes electrophysiological responses to GABA in neurons. *Neuroscience Letters*, *90*(3), 279–284. https://doi.org/10.1016/0304-3940(88)90202-9

Marabelli, A., Lape, R., & Sivilotti, L. (2015). Mechanism of activation of the prokaryotic channel ELIC by propylamine: A single-channel study. *Journal of General Physiology*, *145*(1), 23–45. https://doi.org/10.1085/jgp.201411234

McCarthy, M. P., & Moore, M. A. (1992). Effects of lipids and detergents on the conformation of the nicotinic acetylcholine receptor from Torpedo californica. *Journal of Biological Chemistry*, *267*(11), 7655–7663. https://doi.org/10.1016/S0021-9258(18)42565-3

McCormack, T. J., Melis, C., Colón, J., Gay, E. A., Mike, A., Karoly, R., Lamb, P. W., Molteni, C., & Yakel, J. L. (2010). Rapid desensitization of the rat α7 nAChR is facilitated by the presence of a proline residue in the outer β-sheet. *Journal of Physiology*, *588*(22), 4415–4429. https://doi.org/10.1113/JPHYSIOL.2010.195495;WGROUP:STRING:PUBLICATION

Menny, A., Lefebvre, S. N., Schmidpeter, P. A. M., Drège, E., Fourati, Z., Delarue, M., Edelstein, S. J., Nimigean, C. M., Joseph, D., & Corringer, P.-J. (2017). Identification of a pre-active conformation of a pentameric channel receptor. *ELife*, *6*. https://doi.org/10.7554/eLife.23955

Michaelson, D. M., Duguid, J. R., Miller, D. L., & Raftery, M. A. (1976). Reconstitution of a purified acetylcholine receptor. *Journal of Supramolecular and Cellular Biochemistry*, *4*(3), 419–426. https://doi.org/10.1002/jss.400040312

Michaelson, D. M., & Raftery, M. A. (1974a). *Purified Acetylcholine Receptor: Its Reconstitution to a Chemically Excitable Membrane* (acetylcholine binding/ion translocation)* (Vol. 71, Number 12). https://www.pnas.org

Michaelson, D. M., & Raftery, M. A. (1974b). *Purified Acetylcholine Receptor: Its Reconstitution to a Chemically Excitable Membrane* (acetylcholine binding/ion translocation)* (Vol. 71, Number 12). https://www.pnas.org

Middleton, R. E., & Cohen, J. B. (1991). Mapping of the Acetylcholine Binding Site of the Nicotinic Acetylcholine Receptor: [3H]Nicotine as an Agonist Photoaffinity Label1. *Biochemistry*, *30*, 6987–6997. https://pubs.acs.org/sharingguidelines

Mike, A., Castro, N. G., & Albuquerque, E. X. (2000). Choline and acetylcholine have similar kinetic properties of activation and desensitization on the a7 nicotinic receptors in rat hippocampal neurons. In *Brain Research* (Vol. 882). www.elsevier.com/locate/bres

Miller, P. S., Scott, S., Masiulis, S., Colibus, L. De, Pardon, E., Steyaert, J., & Aricescu, A. R. (2017). Structural basis for GABAA receptor potentiation by neurosteroids. *Nature Structural & Molecular Biology*, *24*(11), 986–992. https://doi.org/10.1038/NSMB.3484

Miller, P. S., Scott, S., Masiulis, S., De Colibus, L., Pardon, E., Steyaert, J., & Aricescu, A. R. (2017). Structural basis for GABAA receptor potentiation by neurosteroids. *Nature Structural & Molecular Biology*, *24*(11), 986–992. https://doi.org/10.1038/NSMB.3484

Miyazawa, A., Fujiyoshi, Y., & Unwin, N. (2003). Structure and gating mechanism of the acetylcholine receptor pore. *Nature 2003 423:6943*, *423*(6943), 949–955. https://doi.org/10.1038/nature01748

Mody, D., Hussein, T. O. K., & Baenziger, J. E. (2025). Lipid-dependent uncoupling of agonist binding and channel gating in the nicotinic acetylcholine receptor. In *Biophysical Reviews*. Springer Science and Business Media Deutschland GmbH. https://doi.org/10.1007/s12551-025-01397-5

Moraga-Cid, G., Sauguet, L., Huon, C., Malherbe, L., Girard-Blanc, C., Petres, S., Murail, S., Taly, A., Baaden, M., Delarue, M., & Corringer, P.-J. (2015). Allosteric and hyperekplexic mutant phenotypes investigated on an α1 glycine receptor transmembrane structure. *Proceedings of the National Academy of Sciences of the United States of America*, *112*(9), 2865–2870. https://doi.org/10.1073/PNAS.1417864112/SUPPL_FILE/PNAS.201417864SI.PDF

Moroni, M., Biro, I., Giugliano, M., Vijayan, R., Biggin, P. C., Beato, M., & Sivilotti, L. G. (2011). Chloride ions in the pore of glycine and GABA channels shape the time course and voltage dependence of agonist currents. *Journal of Neuroscience*, *31*(40), 14095–14106. https://doi.org/10.1523/JNEUROSCI.1985-11.2011

Mukhtasimova, N., Lee, W. Y., Wang, H. L., & Sine, S. M. (2009). Detection and trapping of intermediate states priming nicotinic receptor channel opening. *Nature*, *459*(7245), 451–454. https://doi.org/10.1038/nature07923

Nef, P., Mauron, A., Stalder, R., Alliod, C., & Ballivet, M. (1984). Structure linkage, and sequence of the two genes encoding the delta and gamma subunits of the nicotinic acetylcholine receptor. *Proceedings of the National Academy of Sciences*, *81*(24), 7975–7979. https://doi.org/10.1073/PNAS.81.24.7975

Nemecz, Á., Prevost, M., Menny, A., & Corringer, P.-J. (2016). Emerging Molecular Mechanisms of Signal Transduction in Pentameric Ligand-Gated Ion Channels. *Neuron*, *90*(3), 452–470. https://doi.org/10.1016/j.neuron.2016.03.032

Nury, H., Renterghem, C. Van, Weng, Y., Tran, A., Baaden, M., Dufresne, V., Changeux, J. P., Sonner, J. M., Delarue, M., & Corringer, P.-J. (2011). X-ray structures of general anaesthetics bound to a pentameric ligand-gated ion channel. *Nature*, *469*(7330), 428–431. https://doi.org/10.1038/nature09647

Nys, M., Wijckmans, E., Farinha, A., Yoluk, Ö., Andersson, M., Brams, M., Spurny, R., Peigneur, S., Tytgat, J., Lindahl, E., & Ulens, C. (2016). Allosteric binding site in a Cys-loop receptor ligand-binding domain unveiled in the crystal structure of ELIC in complex with chlorpromazine. *Proceedings of the National Academy of Sciences of the United States of America*, *113*(43), E6696–E6703. https://doi.org/10.1073/pnas.1603101113

Ohno, K., Hutchinson, D. O., Milone, M., Brengman, J. M., Bouzat, C., Sine, S. M., & Engel, A. G. (1995). Congenital myasthenic syndrome caused by prolonged acetylcholine receptor channel openings due to a mutation in the M2 domain of the ε subunit. *Proceedings of the National Academy of Sciences of the United States of America*, *92*(3), 758–762. https://doi.org/10.1073/PNAS.92.3.758;WEBSITE:WEBSITE:PNAS-SITE;WGROUP:STRING:PUBLICATION

Olsen, R. W., & Sieghart, W. (2008). International Union of Pharmacology. LXX. Subtypes of γ-Aminobutyric AcidA Receptors: Classification on the Basis of Subunit Composition, Pharmacology, and Function. Update. *Pharmacological Reviews*, *60*(3), 243–260. https://doi.org/10.1124/PR.108.00505

Pan, J., Chen, Q., Willenbring, D., Mowrey, D., Kong, X.-P. P., Cohen, A. E., Divito, C. B. B., Xu, Y., Tang, P., J, P., Q, C., D, W., D, M., XP, K., A, C., CB, D., Y, X., & P, T. (2012). Structure of the Pentameric Ligand-Gated Ion Channel GLIC Bound with Anesthetic Ketamine. *Structure*, *20*(9), 1463–1469. https://doi.org/10.1016/J.STR.2012.08.009

Pan, J., Chen, Q., Willenbring, D., Yoshida, K., Tillman, T., Kashlan, O. B., Cohen, A. E., Kong, X.-P. P., Xu, Y., & Tang, P. (2012). Structure of the pentameric ligand-gated ion channel ELIC cocrystallized with its competitive antagonist acetylcholine. *Nature Communications*, *3*(1), 1–8. https://doi.org/10.1038/ncomms1703

Papke, D., & Grosman, C. (2014). The role of intracellular linkers in gating and desensitization of human pentameric ligand-gated ion channels. *Journal of Neuroscience*, *34*(21), 7238–7252. https://doi.org/10.1523/JNEUROSCI.5105-13.2014

Petroff, J. T., Dietzen, N. M., Santiago-McRae, E., Deng, B., Washington, M. S., Chen, L. J., Moreland, K. T., Deng, Z., Rau, M., Fitzpatrick, J. A. J., Yuan, P., Joseph, T. T., Hénin, J., Brannigan, G., & Cheng, W. W. L. (2022). Open-channel structure of a pentameric ligand-gated ion channel reveals a mechanism of leaflet-specific phospholipid modulation. *Nature Communications*, *13*(1), 7017. https://doi.org/10.1038/s41467-022-34813-5

Pinheiro, P., & Mulle, C. (2006). Kainate receptors. In *Cell and Tissue Research* (Vol. 326, Number 2, pp. 457–482). https://doi.org/10.1007/s00441-006-0265-6

Prevost, M., Sauguet, L., Nury, H., Renterghem, C. Van, Huon, C., Poitevin, F., Baaden, M., Delarue, M., & Corringer, P.-J. (2012). A locally closed conformation of a

bacterial pentameric proton-gated ion channel. *Nature Structural and Molecular Biology*, *19*(6), 642–649. https://doi.org/10.1038/NSMB.2307

Quick, M. W., & Lester, R. A. J. (2002). Desensitization of Neuronal Nicotinic Receptors. *J Neurobiol*, *53*, 457–478. https://doi.org/10.1002/neu.10109

Rajakulendran, S., Schorge, S., Kullmann, D. M., & Hanna, M. G. (2007). Episodic ataxia type 1: A neuronal potassium channelopathy. *Neurotherapeutics 2007 4:2*, *4*(2), 258–266. https://doi.org/10.1016/J.NURT.2007.01.010

Rankin, S. E., Addona, G. H., Kloczewiak, M. A., Bugge, B., & Miller, K. W. (1997). The cholesterol dependence of activation and fast desensitization of the nicotinic acetylcholine receptor. *Biophysical Journal*, *73*(5), 2446–2455. https://doi.org/10.1016/s0006-3495(97)78273-0

Richardson, B. P., & Engel, G. (1986). The pharmacology and function of 5-HT3receptors. *Trends in Neurosciences*, *9*(C), 424–428. https://doi.org/10.1016/0166-2236(86)90137-2

Riquelme, G., Morato, E., López, E., Ruiz-Gómez, A., Ferragut, J. A., González Ros, J. M., & Mayor, F. (1990). Agonist binding to purified glycine receptor reconstituted into giant liposomes elicits two types of chloride currents. *FEBS Letters*, *276*(1–2), 54–58. https://doi.org/10.1016/0014-5793(90)80505-D

Rovšnik, U., Zhuang, Y., Forsberg, B. O., Carroni, M., Yvonnesdotter, L., Howard, R. J., & Lindahl, E. (2021). Dynamic closed states of a ligand-gated ion channel captured by cryo-EM and simulations. *Life Science Alliance*, *4*(8), 2021.01.04.425171. https://doi.org/10.26508/LSA.202101011

Sauguet, L., Howard, R. J., Malherbe, L., Lee, U. S., Corringer, P.-J., Harris, R. A., & Delarue, M. (2013). Structural basis for potentiation by alcohols and anaesthetics in a ligand-gated ion channel. *Nature Communications*, *4*. https://doi.org/10.1038/NCOMMS2682

Sauguet, L., Poitevin, F., Murail, S., Renterghem, C. Van, Moraga-Cid, G., Malherbe, L., Thompson, A. W., Koehl, P., Corringer, P.-J., Baaden, M., & Delarue, M. (2013). Structural basis for ion permeation mechanism in pentameric ligand-gated ion channels. *EMBO Journal*, *32*(5), 728–741. https://doi.org/10.1038/EMBOJ.2013.17

Sauguet, L., Shahsavar, A., Poitevin, F., Huon, C., Menny, A., Nemecz, Á., Haouz, A., Changeux, J. P., Corringer, P.-J., & Delarue, M. (2014). Crystal structures of a pentameric ligand-gated ion channel provide a mechanism for activation. *Proceedings of the National Academy of Sciences of the United States of America*, *111*(3), 966–971. https://doi.org/10.1073/pnas.1314997111

Schmidt, J., & Raftery, M. A. (1973). Purification of acetylcholine receptors from Torpedo claifornica electroplax by affinity chromatography. *Biochemistry*, *12*(5), 852–856. https://doi.org/10.1021/bi00729a011

Schofield, P. R., Darlison, M. G., Fujita, N., Burt, D. R., Stephenson, F. A., Rodriguez, H., Rhee, L. M., Ramachandran, J., Reale, V., Glencorse, T. A., Seeburg, P. H., & Barnard, E. A. (1988). Sequence and functional expression of the GABAA receptor shows a ligand-gated receptor super-family. *Nature*, *328*(6127), 221–227. https://doi.org/10.1038/328221A0;KWRD

Schwiening, C. J. (2012). A brief historical perspective: Hodgkin and Huxley. In *Journal of Physiology* (Vol. 590, Number 11, pp. 2571–2575). https://doi.org/10.1113/jphysiol.2012.230458

Shen, W., Mennerick, S., Covey, D. F., & Zorumski, C. F. (2000a). Pregnenolone Sulfate Modulates Inhibitory Synaptic Transmission by Enhancing GABAA Receptor Desensitization. *Journal of Neuroscience*, *20*(10), 3571–3579. https://doi.org/10.1523/JNEUROSCI.20-10-03571.2000

Shen, W., Mennerick, S., Covey, D. F., & Zorumski, C. F. (2000b). Pregnenolone Sulfate Modulates Inhibitory Synaptic Transmission by Enhancing GABAA Receptor Desensitization. *Journal of Neuroscience*, *20*(10), 3571–3579. https://doi.org/10.1523/JNEUROSCI.20-10-03571.2000

Sine, S. M., Ohno, K., Bouzat, C., Auerbach, A., Milone, M., Pruitt, J. N., & Engel, A. G. (1995). Mutation of the acetylcholine receptor α subunit causes a slow-channel myasthenic syndrome by enhancing agonist binding affinity. *Neuron*, *15*(1), 229–239. https://doi.org/10.1016/0896-6273(95)90080-2

Smit, A. B., Syed, N. I., Schaap, D., Van Minnen, J., Klumperman, J., Kits, K. S., Lodder, H., Van Der Schors, R. C., Van Elk, R., Sorgedrager, B., Brejc, K., Sixma, T. K., & Geraerts, W. P. M. (2001). A glia-derived acetylcholine-binding protein that modulates synaptic transmission. *Nature 2001 411:6835*, *411*(6835), 261–268. https://doi.org/10.1038/35077000

Sooksawate, T., & Simmonds, M. A. (2001a). Effects of membrane cholesterol on the sensitivity of the GABAA receptor to GABA in acutely dissociated rat hippocampal neurones. *Neuropharmacology*, *40*(2), 178–184. https://doi.org/10.1016/S0028-3908(00)00159-3

Sooksawate, T., & Simmonds, M. A. (2001b). Influence of membrane cholesterol on modulation of the GABAA receptor by neuroactive steroids and other potentiators. *British Journal of Pharmacology*, *134*(6), 1303–1311. https://doi.org/10.1038/sj.bjp.0704360

Spurny, R., Billen, B., Howard, R. J., Brams, M., Debaveye, S., Price, K. L., Weston, D. A., Strelkov, S. V, Tytgat, J., Bertrand, S., Bertrand, D., Lummis, S. C. R., & Ulens, C. (2013). Multisite Binding of a General Anesthetic to the Prokaryotic Pentameric Erwinia chrysanthemi Ligand-gated Ion Channel (ELIC). *Journal of Biological Chemistry*, *288*(12), 8355–8364. https://doi.org/10.1074/JBC.M112.424507

Spurny, R., Debaveye, S., Farinha, A., Veys, K., Vos, A. M., Gossas, T., Atack, J., Bertrand, S., Bertrand, D., Danielson, U. H., Tresadern, G., & Ulens, C. (2015). Molecular blueprint of allosteric binding sites in a homologue of the agonist-binding domain of the α7 nicotinic acetylcholine receptor. *Proceedings of the National Academy of Sciences*, *112*(19), E2543–E2552. https://doi.org/10.1073/PNAS.1418289112

Spurny, R., Ramerstorfer, J., Price, K., Brams, M., Ernst, M., Nury, H., Verheij, M., Legrand, P., Bertrand, D., Bertrand, S., Dougherty, D. A., Esch, I. J. P. De, Corringer, P.-J., Sieghart, W., Lummis, S. C. R. R., Ulens, C., & de Esch, I. J. P. (2012). Pentameric ligand-gated ion channel ELIC is activated by GABA and modulated by benzodiazepines. *Proceedings of the National Academy of Sciences of the United States of America*, *109*(44), E3028–E3034. https://doi.org/10.1073/pnas.1208208109

Sridhar, A., Lummis, S. C. R., Pasini, D., Mehregan, A., Brams, M., Kambara, K., Bertrand, D., Lindahl, E., Howard, R. J., & Ulens, C. (2021). Regulation of a pentameric ligand-gated ion channel by a semiconserved cationic lipid-binding site. *Journal of Biological Chemistry*, *297*(2), 100899. https://doi.org/10.1016/j.jbc.2021.100899

Südhof, T. C. (2013). Neurotransmitter release: The last millisecond in the life of a synaptic vesicle. *Neuron*, *80*(3), 675–690. https://doi.org/10.1016/j.neuron.2013.10.022

Sun, C., Zhu, H., Clark, S., & Gouaux, E. (2023). Cryo-EM structures reveal native GABAA receptor assemblies and pharmacology. *Nature*, *622*(7981), 195–201. https://doi.org/10.1038/s41586-023-06556-w

Sunshine, C., & McNamee, M. G. (1992). Lipid modulation of nicotinic acetylcholine receptor function: the role of neutral and negatively charged lipids. *Biochimica et Biophysica Acta*, *1108*(2), 240–246. https://doi.org/10.1016/0005-2736(92)90031-G

Swanson, G. T. (2009). Targeting AMPA and kainate receptors in neurological disease: Therapies on the horizon? In *Neuropsychopharmacology* (Vol. 34, Number 1, pp. 249–250). https://doi.org/10.1038/npp.2008.158

Tan, B. K., Xu, H., Sandberg, J. W., Brannigan, G., & Cheng, W. W. L. (2025). *Structural mechanism of lipid modulation of pentameric ligand-gated ion channel activity*. https://doi.org/10.1101/2025.10.07.680764

Tasneem, A., Iyer, L. M., Jakobsson, E., & Aravind, L. (2005). Identification of the prokaryotic ligand-gated ion channels and their implications for the mechanisms

and origins of animal Cys-loop ion channels. *Genome Biology*, *6*(1). https://doi.org/10.1186/GB-2004-6-1-R4

Tecott, L. H., Maricq, A. V., & Julius, D. (1993). Nervous system distribution of the serotonin 5-HT3 receptor mRNA. *Proceedings of the National Academy of Sciences of the United States of America*, *90*(4), 1430–1434. https://doi.org/10.1073/PNAS.90.4.1430;WGROUP:STRING:PUBLICATION

Therien, J. P. D., & Baenziger, J. E. (2017). Pentameric ligand-gated ion channels exhibit distinct transmembrane domain archetypes for folding/expression and function. *Scientific Reports*, *7*(1). https://doi.org/10.1038/S41598-017-00573-2

Thompson, M. J., & Baenziger, J. E. (2020). Structural basis for the modulation of pentameric ligand-gated ion channel function by lipids. *Biochimica et Biophysica Acta - Biomembranes*, *1862*(9), 183304. https://doi.org/10.1016/j.bbamem.2020.183304

Thompson, M. J., Domville, J. A., Edrington, C. H., Venes, A., Giguère, P. M., & Baenziger, J. E. (2022). Distinct functional roles for the M4 α-helix from each homologous subunit in the heteropentameric ligand-gated ion channel nAChR. *Journal of Biological Chemistry*, *298*(7). https://doi.org/10.1016/j.jbc.2022.102104

Thompson, M. J., Tessier, C. J. G., Ananchenko, A., Emlaw, J. R., Dehez, F., Zarkadas, E., daCosta, C. J. B., Nury, H., & Baenziger, J. E. (n.d.). *Asynchronous subunit transitions precede acetylcholine receptor activation*.

Tong, A., Hsu, F. F., Schmidpeter, P. A., Nimigean, C. M., Sharp, L., Brannigan, G., & Cheng, W. W. L. (2019). Direct binding of phosphatidylglycerol at specific sites modulates desensitization of a Ligand-gated ion channel. *ELife*, *8*. https://doi.org/10.7554/eLife.50766

Toyoshima, C., & Unwin, N. (1988a). Contrast transfer for frozen-hydrated specimens: Determination from pairs of defocused images. *Ultramicroscopy*, *25*(4), 279–291. https://doi.org/10.1016/0304-3991(88)90003-4

Toyoshima, C., & Unwin, N. (1988b). *Ion channel of acetylcholine receptor reconstructed from images of postsynaptic membranes*.

Toyoshima, C., & Unwin, N. (1990). Three-dimensional structure of the acetylcholine receptor by cryoelectron microscopy and helical image reconstruction. *Journal of Cell Biology*, *111*(6), 2623–2635. https://doi.org/10.1083/JCB.111.6.2623

Unwin, N. (1993). Nicotinic Acetylcholine Receptor an 9 Å Resolution. *Journal of Molecular Biology*, *229*(4), 1101–1124. https://doi.org/10.1006/jmbi.1993.1107

Unwin, N. (2005). Refined structure of the nicotinic acetylcholine receptor at 4A resolution. *Journal of Molecular Biology*, *346*(4), 967–989. https://doi.org/10.1016/J.JMB.2004.12.031

Unwin, N., Toyoshima, C., & Kubalek, E. (1988). Arrangement of the acetylcholine receptor subunits in the resting and desensitized states, determined by cryoelectron microscopy of crystallized Torpedo postsynaptic membranes. *Journal of Cell Biology*, *107*(3), 1123–1138. https://doi.org/10.1083/JCB.107.3.1123

Velisetty, P., & Chakrapani, S. (2012). Desensitization mechanism in prokaryotic ligand-gated ion channel. *Journal of Biological Chemistry*, *287*(22), 18467–18477. https://doi.org/10.1074/jbc.M112.348045

Velisetty, P., Chalamalasetti, S. V., & Chakrapani, S. (2012). Conformational transitions underlying pore opening and desensitization in membrane-embedded Gloeobacter

violaceus ligand-gated ion channel (GLIC). *The Journal of Biological Chemistry*, *287*(44), 36864–36872. https://doi.org/10.1074/JBC.M112.401067

Voglis, G., & Tavernarakis, N. (2006). The role of synaptic ion channels in synaptic plasticity. In *EMBO Reports* (Vol. 7, Number 11, pp. 1104–1110). https://doi.org/10.1038/sj.embor.7400830

Whiting, P. J., & Lindstrom, J. M. (1988). Characterization of bovine and human neuronal nicotinic acetylcholine receptors using monoclonal antibodies. *Journal of Neuroscience*, *8*(9), 3395–3404. https://doi.org/10.1523/JNEUROSCI.08-09-03395.1988

Williams, D. K., Wang, J., & Papke, R. L. (2011). Investigation of the Molecular Mechanism of the α7 Nicotinic Acetylcholine Receptor Positive Allosteric Modulator PNU-120596 Provides Evidence for Two Distinct Desensitized States. *Molecular Pharmacology*, *80*(6), 1013–1032. https://doi.org/10.1124/MOL.111.074302

Yao, L., Liu, C., Wang, N., Du, F., Fan, S., Guo, Y., Zhang, L., Pan, Y., & Xiong, W. (2020). Cholesterol regulates cannabinoid analgesia through glycine receptors. *Neuropharmacology*, *177*(June), 108242. https://doi.org/10.1016/j.neuropharm.2020.108242

Yao, L., Wells, M., Wu, X., Xu, Y., Zhang, L., & Xiong, W. (2020). Membrane cholesterol dependence of cannabinoid modulation of glycine receptor. *FASEB Journal*, *34*(8), 10920–10930. https://doi.org/10.1096/fj.201903093R

Young, A. B., & Snyder, S. H. (1973). Strychnine Binding Associated with Glycine Receptors of the Central Nervous System. *Proceedings of the National Academy of Sciences*, *70*(10), 2832–2836. https://doi.org/10.1073/PNAS.70.10.2832

Young, A. B., & Snyder, S. H. (1974). The glycine synaptic receptor: evidence that strychnine binding is associated with the ionic conductance mechanism. *Proceedings of the National Academy of Sciences of the United States of America*, *71*(10), 4002–4005. https://doi.org/10.1073/PNAS.71.10.4002;ISSUE:ISSUE:DOI

Young, M. T. (2010). P2X receptors: dawn of the post-structure era. In *Trends in Biochemical Sciences* (Vol. 35, Number 2, pp. 83–90). https://doi.org/10.1016/j.tibs.2009.09.006

Yu, J., Zhu, H., Lape, R., Greiner, T., Du, J., Lü, W., Sivilotti, L., & Gouaux, E. (2021a). Mechanism of gating and partial agonist action in the glycine receptor. *Cell*, *184*(4), 957-968.e21. https://doi.org/10.1016/J.CELL.2021.01.026

Yu, J., Zhu, H., Lape, R., Greiner, T., Du, J., Lü, W., Sivilotti, L., & Gouaux, E. (2021b). Mechanism of gating and partial agonist action in the glycine receptor. *Cell*, *184*(4), 957-968.e21. https://doi.org/10.1016/J.CELL.2021.01.026

Yuan, Z., Pavel, M. A., & Hansen, S. B. (2025). GABA and astrocytic cholesterol determine the lipid environment of GABAAR in cultured cortical neurons. *Communications Biology*, *8*(1). https://doi.org/10.1038/s42003-025-08026-7

Zhuang, Y., Noviello, C. M., Hibbs, R. E., Howard, R. J., & Lindahl, E. (2022). Differential interactions of resting, activated, and desensitized states of the α7 nicotinic acetylcholine receptor with lipidic modulators. *Proceedings of the National Academy of Sciences of the United States of America*, *119*(43), e2208081119. https://doi.org/10.1073/PNAS.2208081119;PAGE:STRING:ARTICLE/CHAPTER

Zimmermann, I., & Dutzler, R. (2011). Ligand activation of the Prokaryotic Pentameric ligand-gated ion channel ELIC. *PLoS Biology*, *9*(6), e1001101. https://doi.org/10.1371/journal.pbio.1001101

Zimmermann, I., Marabelli, A., Bertozzi, C., Sivilotti, L. G., & Dutzler, R. (2012). Inhibition of the Prokaryotic Pentameric Ligand-Gated Ion Channel ELIC by Divalent Cations. *PLoS Biology*, *10*(11), e1001429. https://doi.org/10.1371/journal.pbio.1001429

Zukin, S. R., Young, A. B., & Snyder, S. H. (1974). Gamma-aminobutyric acid binding to receptor sites in the rat central nervous system. *Proceedings of the National Academy of Sciences of the United States of America*, *71*(12), 4802–4807. https://doi.org/10.1073/PNAS.71.12.4802;PAGEGROUP:STRING:PUBLICATION

7 Appendix

Chapter 3 GlyR Aromatic Mutants

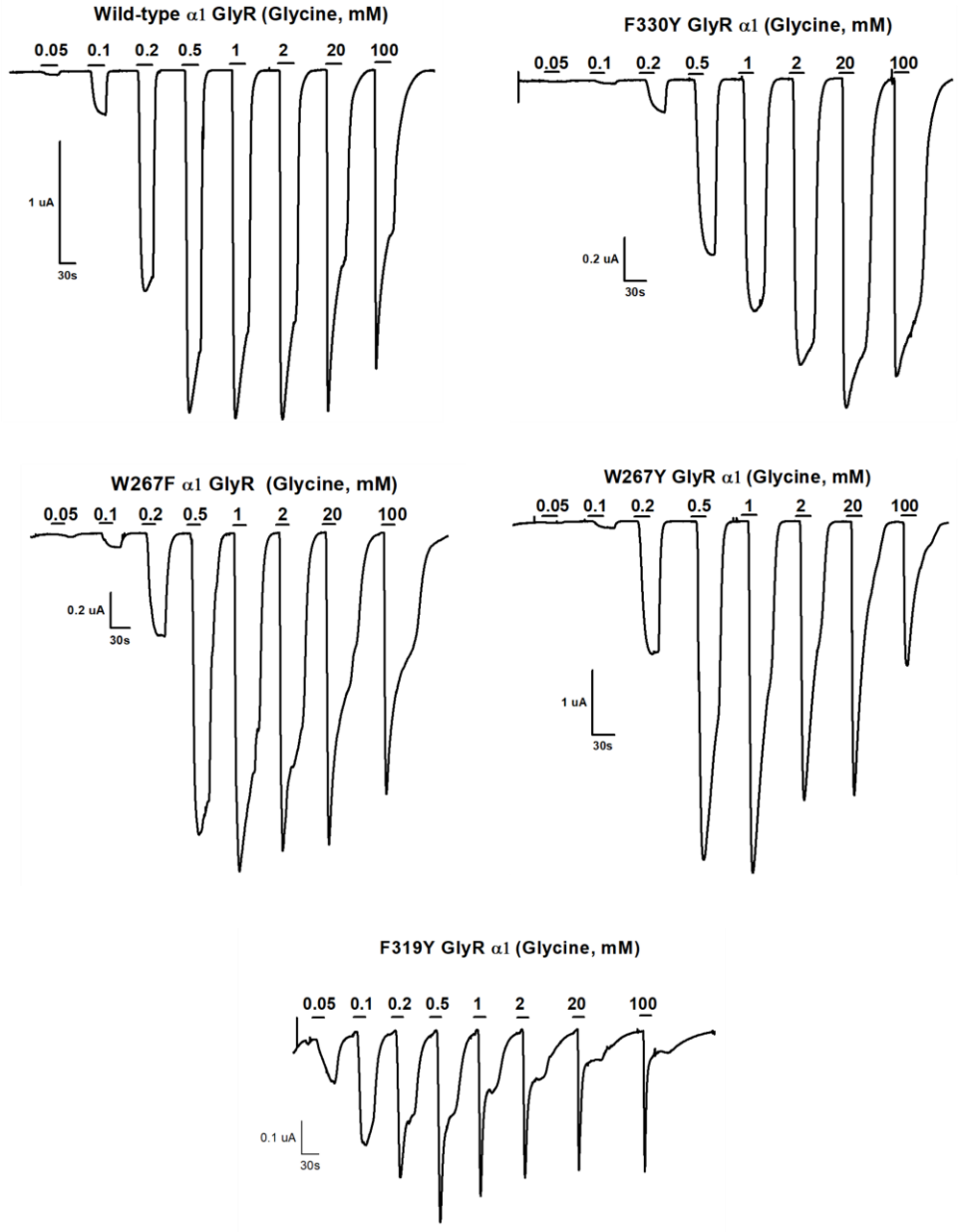

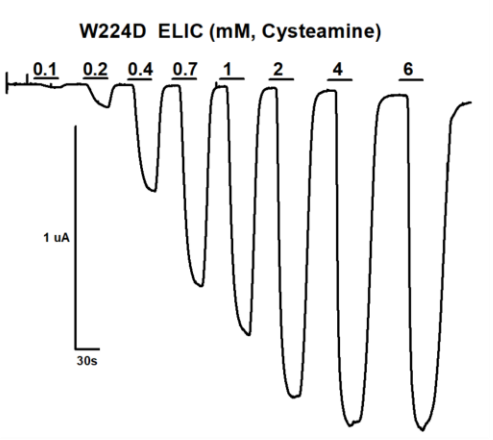
W224D ELIC (mM, Cysteamine)
0.1
0.2
0.4
0.7
1
2
4
6
1 uA
30s

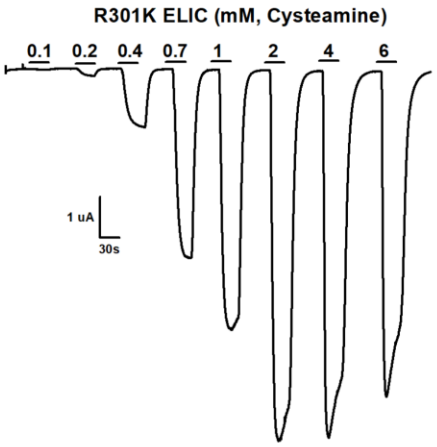
R301K ELIC (mM, Cysteamine)
0.1
0.2
0.4
0.7
1
2
4
6
1 uA
30s

8 Toka Hussein – CV

- International graduate student in biochemistry at the University of Ottawa.
- Experience in chemistry teaching and curriculum development.
- Excellent communication and problem-solving skills earned through 11 years of research experience.
- Fluent in English (Academic IELTS band 8.0 (2019); General CELP-IP 12 (2023)).

EDUCATION

Doctor of Philosophy in Biochemistry — **September 2021 - Present**
Department of Biochemistry, Microbiology, and Immunology (BMI), Faculty of Medicine, University of Ottawa, Ottawa, Canada

Master of Science in Biochemistry — **September 2019 – August 2021**
Department of Biochemistry, Microbiology, and Immunology (BMI), Faculty of Medicine, University of Ottawa, Ottawa, Canada
- GPA: 9.6/10

Bachelor of Science in Biomedical Sciences — **September 2013 - June 2018**
University of Science and Technology, Zewail City of Science and Technology, Egypt
- Drug Design and Development Concentration
- 5 years program, GPA 3.4/4.0

Summer Student - Bioinformatics Lab Intern - Computational drug design internship — **July 2017 - August 2017**
School of Life Sciences and Biotechnology, Dr. Haifeng Chen's lab, Shanghai Jiao Tong University, China

Summer School, Advances in Drug Discovery — **September 2016**
University of Chemistry and Technology, Prague, Czech Republic.

ACADEMIC AWARDS

- Biophysical Society of Canada 2023 Travel Award — **May 2023**
- Admission scholarship (University of Ottawa) — **September 2021- present**
- International student scholarship (University of Ottawa) — **September 2021- present**
- Roger Guindon scholarship fund (University of Ottawa) — **September 2021**
- CREATE-APRENTICE Trainee scholarship program - NSERC — **September 2020 - August 2022**
- International graduate bursary (University of Ottawa) — **September 2018 – August 2021**
- Full admission scholarship (University of Science and Technology) — **September 2013 - June 2018**
- Best team award at SOLE Biotechnology competition participant. — **August 2015**
- Best poster in Microbiology research day (University of Science and Technology) — **January 2015**
- Best poster award at Annual Undergraduate Scientific Conference — **June 2014**

RESEARCH EXPERIENCE

Biochemistry PhD Candidate — **September 2021 - Present**
Dr. John E. Baenziger lab, Department of Biochemistry, Microbiology, and Immunology (BMI), Faculty of Medicine, University of Ottawa, Ottawa, Canada
- Thesis title: Lipid-dependent modulation of desensitization in pentametric ligand-gated ion channels.

- Whole-cell electrophysiology studies on pentameric ligand-gated ion channels using Two-electrode voltage clamp (TEVC) technique.
- Training and mentoring undergraduate students:
    - Danielle Bonini – DEGREE shadowing program
    - Jack Cowan – TMM program rotation student

Masters' student **September 2019 – August 2021**

Dr. Jyh-Yeuan Lee lab, Department of Biochemistry, Microbiology, and Immunology (BMI), Faculty of Medicine, University of Ottawa, Ottawa, Canada

- Expressed and purified the membrane protein ABCG5/G8 in milligram quantities. Purified protein was then used for structural studies by colleagues.
- Developed nanodisc reconstitution protocol for ABCG5/G8 in membrane scaffold protein (MSP) nanodiscs.
- Training and mentoring undergraduate students:
    - Yudhvir Bhatti – Volunteer 2020-2021
    - Ahnaf Tahmid – Volunteer 2020-2021
    - Molly de Barros – Honors student 2019-2020
    - Rhea Gupta – UROP 2019-2020

Research Assistant **December 2018 - June 2019**

Dr. Fareed Aboulela's lab, Center for X-Ray Determination of the Structure of Matter, Zewail City of Science and Technology, Giza, Egypt

- Produced *in-vitro* RNA SAM Riboswitches in preparation for structural studies using small angle x-ray scattering (SAXS).
- Conducted biophysical characterization experiments using dynamic light scattering (DLS) and differential scanning calorimetry (DSC).
- Expressed and purified cell-soluble proteins with affinity chromatography and size exclusion chromatography using ÄKTA-FPLC system.

Undergraduate Research Assistant **January 2017 - June 2018**

Dr. Fareed Aboulela's lab, Center for X-Ray Determination of the Structure of Matter, Zewail City of Science and Technology, Giza, Egypt

- Conducted literature reviews and developed research protocols.
- Gained proficient experience in molecular biology techniques including PCR, RNA *in-vitro* transcriptions, electroelution and dialysis.

Research Intern **August 2015 - August 2016**

Dr. Reem Arafa's lab, Drug Design and Development Group, Zewail City of Science and Technology, Egypt

- Achieved proficient experience at ligand docking and 2D QSAR using Molecular Operating Environment (MOE) program.

Research Intern **June 2014 - September 2015**

Dr. Ayman El Shibiny's lab, Phage Therapy Research Group, Zewail City of Science and Technology, Egypt

- Earned proficient experience at microbiology lab techniques and bacteriophage isolation from environmental samples.

TEACHING EXPERIENCE

Chemistry/Biochemistry tutor **September 2022 – February 2025**

Go2Grad tutors

- Guide students in chemistry concepts, boosting grades and confidence through tailored lessons.

- Develop engaging lesson plans, enhancing student understanding and retention in chemistry.
- Utilize diverse teaching methods to address varied learning styles, achieving improved outcomes.
- Monitor student progress, providing feedback to foster academic growth and motivation.
- Collaborate with parents to support student success, ensuring a comprehensive learning approach.

Immunology Teaching Assistant / Demonstrator / Lab monitor **September 2023 – December 2023**
University of Ottawa, Faculty of Medicine

- Exam invigilation
- Marked midterm exams

uOGlobal course Teaching Assistant / Demonstrator / Lab monitor **October 2022 - April 2023**

University of Ottawa, International Office

- Facilitated group discussions and in class activities.
- Marked submitted assignments and provided constructive feedback to the students.

Biochemistry Lab Teaching Assistant / Demonstrator / Lab monitor **January 2020 - April 2020**

University of Ottawa, Faculty of Science

- Demonstrated experiments to students in the lab and provided guidance throughout the experiments.
- Marked laboratory reports and provided constructive feedback to the students.

Teaching Effectiveness Unit Intern **October 2017 - February 2018**

Center of Learning Technologies - Zewail City of Science and Technology, Egypt

- Conducted literature reviews on pedagogy and curriculum design.
- Developed new approaches in training professors at Zewail City.
- Organized 2 teaching effectiveness workshops for professors.
- Facilitated mid-term courses' evaluation and regular meetings with student representatives to enhance the teaching quality.

Analytical and Physical Chemistry Teaching Assistant **February 2017 - June 2017**

University of Science and Technology at Zewail City of Science and Technology, Egypt

- Reinforce lessons presented by professors by reviewing material with students.
- Responsible for conducting office hours and technical enhancement for students.

PROFESSIONAL EXPERIENCE

Paid Social PhD Strategist **January 2026 - present**
Supreme Optimization, remote

Chemistry Content Developer **August - November 2018**
Nagwa LTD., Nasr City, Cairo, Egypt

- Developed chemistry curriculum plans to create and deliver high-quality content.
- Analyzed learning objectives and design questions to meet them.
- Ensured content alignment with different curriculum frameworks.
- Conducted technical interviews with applicants applying to the team.

PEER-REVIEWED PUBLICATIONS

- Mody, D., **Hussein, T. O. K.,** & Baenziger, J. E. (2025). Lipid-dependent uncoupling of agonist binding and channel gating in the nicotinic acetylcholine receptor. Biophysical Reviews, 1-17.
- Ananchenko, A., **Hussein, T. O. K.**, Mody, D., Thompson, M. J., & Baenziger, J. E. (2022). Recent Insight into Lipid Binding and Lipid Modulation of Pentameric Ligand-Gated Ion Channels. Biomolecules, 12(6), 814.
- Baenziger, J. E., Ananchenko, A., **Hussein, T. O. K.,** & Mody, D. (2021). IUPAB 2021 Symposium 13: ion channels and membrane transporters. *Biophysical Reviews, 1-3*.
- Khunweeraphong, N., Mitchell-White, J., Szöllősi, D., **Hussein, T.O.K.,** Kuchler, K., Kerr, I.D., Stockner, T. and Lee, J.Y., 2020. Picky ABCG5/G8 and promiscuous ABCG2-a tale of fatty diets and drug toxicity. *FEBS Letters*, *594*(23), p.4035.
- Zein, A.A., Kaur, R., **Hussein, T.O.K**., Graf, G.A. and Lee, J.Y., (2019). ABCG5/G8: a structural view to pathophysiology of the hepatobiliary cholesterol secretion. *Biochemical society transactions*, *47*(5), pp.1259-1268.

ORAL PRESENTATIONS

Invited speaker at She Talks Science Summit **October 2022**

Bioscience GP Ltd., Egypt

- Presentation title: "How can structural biology revolutionize drug design?"

Protein Engineering Canada (PEC), Montreal, Canada **June 2022**

- International conference
- "Lipid-dependent modulation of desensitization in pentameric ligand-gated ion channels"

Work in Progress Seminars **November 2020**

Department of Biochemistry, Microbiology, and Immunology (BMI), Faculty of Medicine, University of Ottawa

- Local seminar
- "Structural analysis of the cholesterol transporter ABCG5/G8"

SOLE Biotechnology Competition Participant, Zewail City's Presentation Team **August 2015**

- **National competition**
- **Presentation title: "Biofuels"**

Drug Design and Development Day: From Bench to Market **February 2015**

Zewail City of Science and Technology, Egypt

- **Local Research Day**
- **Presentation title: "Antimalarial drugs"**

Biotechnology Month Conference **September 2014**

Cairo University, Egypt

- **National conference**
- **Presentation title: "Phage Therapy"**

POSTER PRESENTATIONS

Canadian Society for Chemistry (CEC) **June 2025**
Ottawa, Canada
- International conference
- **Toka O.K. Hussein**, John E. Baenziger. Decoding the effects of lipid-protein interactions on the mechanisms of desensitization of a pentameric ligand-gated ion channel

9th Annual meeting of the Biophysical Society of Canada **May 2024**
University of Montreal, Quebec, Canada
- National conference
- **Toka O.K. Hussein**, John E. Baenziger. Lipid-dependent modulation of desensitization in pentameric ligand-gated ion channels.

Canadian Society for Molecular Biosciences (CSMB) meeting **June 2023**
University of Ottawa, Ontario, Canada
- National conference
- **Toka O. K. Hussein**, Thao Nguyen-Tran, Anu Surendra, Irina Alecu, Mary Ellen Harper, Eric Smith, Miroslava Cuperlovic-Culf, Steffany A.L. Bennett. Investigating lipidomic biomarkers in cerebral small vessel disease (cSVD) patients using machine learning methods.

8th Annual meeting of the Biophysical Society of Canada **May 2023**
University of Calgary, Alberta, Canada
- National conference
- **Toka O.K. Hussein**, John E. Baenziger. Lipid-dependent modulation of desensitization in pentameric ligand-gated ion channels.

CREATE-APRENTICE retreat **May 2021**
Natural Science and Engineering Research Council of Canada (NSERC)
- **Toka O.K. Hussein**, Jean-François Couture, Jyh-Yeuan Lee. Reconstitution of the sterol transporter ABCG5/G5 in membrane scaffold protein (MSP) nanodiscs

Faculty of Medicine Research Day **September 2020**
University of Ottawa, Ontario, Canada
- Local conference
- **Toka O.K. Hussein**, Jyh-Yeuan Lee. "Structural analysis of the cholesterol transporter ABCG5/G8"

3rd Prague Summer School, Advances in Drug Discovery **September 2016**
University of Chemistry and Technology, Prague, Czech Republic
- International summer school
- Abdelraouf R., Habashy M., **Hussein T. O. K.**, Elghazawy N., Arafa R. Novel Pharmacophore Model for the Design of Anti-HIV Integrase LEDGF/p53 site Targeted Drugs and its Applications,

Microbiology Research Day **January 2015**
Zewail City of Science and Technology, Egypt
- Local research day
- Title: "A Closer look onto *Pseudomonas aeruginosa*"

Annual Undergraduate Scientific Conference **June 2014**
Zewail City of Science and Technology, Egypt
- Local conference
- Title: "Phage Therapy"

LAB TECHNIQUES

- **Animal care**
  - *Xenopus laevis* dissection and oocytes extraction
- **Electrophysiology**
  - Two-electrode voltage clamp (TEVC)
- **Molecular biology**
  - Cloning and PCR
  - *In-vitro* RNA transcription
- **Protein biochemistry**
  - Recombinant protein expression and purification.
  - Nanodisc reconstitution in membrane mimetic systems
  - Dynamic light scattering (DLS)
  - Differential scanning calorimetry (DSC)
- **Cryo-electron microscopy (Cryo-EM)**
  - Grids handling, preparation and negative staining
  - Vitrification using Vitrobot (FEI)
  - Transmission electron microscopy (TEM) imaging.
- **Computational drug design**
  - Ligand docking using MOE, Maestro and Autodock.
  - 2D and 3D QSAR using MOE and SYBYL-X

VOLUNTEER EXPERIENCE AND EXTRACURRICULAR ACTIVITIES

- Secretary for the Altavista campus Health and Safety committee, University of Ottawa — January 2024 – December 2025
- Graduate Student's Association des étudiant.es diplômé.es (GSAÉD) representative for the BMI Graduate Student Association (BMIGSA) University of Ottawa — May 2023 – April 2024
- Undergraduate tutor: General chemistry and Organic chemistry
- Member at large at Biophysical Society of Canada (BSC) Trainee Executive — September 2022 - February 204
- Board of Trustees member at Zewail City Alumni Association (ZCAA) — May 2022 – May 2023
- International students' representative at the BMIGSA — December 2021 – December 2022
- Biophysical Society of Canada (BSC) Trainee Symposium 2022 organizer — September 2021 – April 2023
  - Reached out and invited 4 speakers from different fields.
  - Moderated the career panel session.
  - Secured $750 as funds for the trainee symposium and stationary sponsor (through CUPE2626 and RBC on Campus) — May 2022
- Founding Team and Activities Head at Zewail City Alumni Association (ZCCA) — August 2020- June 2021
- Judge at IgNITE Case Competition 2020/2021 — December 2020 – January 2021
- BMI Department Work-in-Progress (WIP) Seminar's coordinator — October 2020 - April 2020
- VP Wellness at the BMI Graduate Student Association (BMIGSA) — September 2020 - March 2021
- Let's Talk Science Volunteer — September 2019 - September 2020
- Member of University Affairs and Equity Committees at GSAÉD, University of Ottawa — October 2019 - August 2020
- Organizer at Several scientific Conferences and Workshops:
  - Workshop: Key Concepts in Cheminformatics for Sound Drug Design, Zewail City — 31st January – 1st February 2018
  - Zewail City Conference and Exhibition on Biomedical Sciences, Zewail City
  - Annual Undergraduate Scientific Conference, Zewail City
- Vice President of Enactus Zewail City — 21-22 April 2017
  - Won HH Sheikha Fatima Bint Mubarak Award for the Arab Youth in Creator Project category for our project 'Mooztilizer' — 17-18 June 2014
- Member of Zewail City Youth Advisory Council — October 2015 – October 2016; December 2014 – December 2015

- Co-founder of Enactus Zewail City and Head of Events and Coordination committee — October 2014 – October 2015
    - Our team was qualified to the Final in the National Competition in its first year of participation, 3 thematic competitions were won. Our team won the 4th place.
- Head of the Academic Committee at Zewail City's Student Union — November 2013 – November 2014